The Black Hole Spin Controversy

KOLEHMAINEN, MARI,JOHANNA

The Black Hole Spin Controversy

Mari J. Kolehmainen

A thesis presented for the degree of
Doctor of Philosophy

Department of Physics
University of Durham
United Kingdom

September 2012

Abstract

Astrophysical black holes are the simplest possible objects. They are completely described by only two parameters in general relativity, their mass and the specific angular momentum, spin. The spin is a fundamental characteristic of a black hole, but unlike mass it leaves a mark on space-time only very close to the event horizon, and is therefore more difficult to measure. The observational relevance of the spin comes from the fact that it sets the size scale of the last stable orbit around the accreting black hole, dragging the accretion disc farther in the faster it spins.

Black hole spin is a very controversial topic in both stellar and supermassive black holes. There are two methods to determine spin in binary systems, using either the direct disc continuum or the reflected emission. These can give significantly different values, and understanding the source of this discrepancy is important especially for interpreting AGN spin, where only the reflection method can be used.

We have strived to understand and carefully model the time-averaged energy spectra from several Galactic black hole binaries, in order to ultimately measure the black hole spin. Achieving this has required in-depth understanding of the *instruments* as well as the data analysis methods. The spin leaves only minor traces in the data, and these can be affected by calibration uncertainties, uncertainties in the models and systematic uncertainties. This knowledge is absolutely essential for a detailed analysis of all relativistically smeared atomic features seen in the time-averaged energy spectra of compact objects.

Contents

List of Figures

List of Tables

Declaration

The work described in this thesis was undertaken between 2009–2012 when the author was a postgraduate research student under the supervision of Prof. Chris Done in the Department of Physics at the University of Durham. This work has not been submitted for any other degree at the University of Durham or any other University.

Portions of this thesis have appeared in the following papers:

- Kolehmainen, M., & Done, C. 2010, MNRAS, 406, 2206
- Kolehmainen, M., Done, C., & Díaz Trigo, M., 2011, MNRAS, 416, 311
- Kolehmainen, M., Done, C., & Díaz Trigo, M., 2012, MNRAS, in preparation

Acknowledgements

First things first: a massive thank you to my amazing supervisor Prof. Chris Done. If I was not quite sure what I was getting myself into when I came to do a PhD at Durham, I could not have imagined a better 3.5 years. The many conferences, visitors, physics chats and all the countless bottles of wine in between made for a truly fantastic PhD experience. I cannot thank you enough, Chris, for the incredible start to my career you gave me!

What made my time in Durham so special was the amazing X-ray group.
My 'original office' boys and dearest friends, Matt and Adam, love you loads! Life will be weird without you two always around.
A special shout-out also to Tim, Nessie, Cameron, Nikki, Andy, Floyd, Jay and Emma. Who knew working long hours could be so much fun!
My home boys, Tom and Max, thanks for the countless good times (and tequila)!

Uskomatonta että se on nyt valmis! Suurin kiitos kaikesta kuuluu omalle perheelleni. Äiti, iskä ja Jari, ilman teitä maailma olisi iso ja pelottava. Elämä Englannissa on ollut mahtavaa, mutta yksi viikon kohokohdista on aina sunnuntain skypeily. Tätä kiitollisuutta on vaikea kuvailla arvoisillaan sanoilla, suunnattoman suuri kiitos kaikesta tuesta ja kannustuksesta! Olette kaikki mielessäni joka ikinen päivä.

Erityiskiitos myös mummolle, jonka anteliaalla tuella oli suuri ja ennen kaikkea suora vaikutus tämän väitöskirjan valmistumiseen.

Astrofysiikan tohtori, kuka olisi uskonut?

Chapter 1

Introduction to Black Hole Spin

During the past fifty years or so, black holes have become basic elements in our conception of the world; understanding them is a very important part of understanding the Universe. By definition we cannot observe them directly, but they can be easily studied when they interact with other objects, accreting matter and producing copious high energy luminosity from the immense gravitational potential energy released by the in-falling material. Black holes represent extreme gravity - a phenomenon which is not possible to reproduce anywhere on Earth. Thus they give us the chance to explore conditions that are not attainable anywhere else, conditions that are very important in understanding the complex physical Universe we live in. In that aspect, black holes are ideal laboratories for studying fundamental physics.

1.1 Black hole binaries

The evolution of a star depends on its initial mass. After the star exhausts the supply of hydrogen in its core, there is no fusion heating source to counteract the force of gravity. This leads to core collapse, and the end-point of the star's evolution depends on its initial mass. Low-mass stars will end up as white dwarfs, whereas more massive stars experience more catastrophic endings, exploding as supernovae and leaving behind a neutron star or a black hole. If a binary star system survives the supernova, it ends up as a binary with a compact primary component (black hole or a neutron star) and a non-degenerate secondary companion star.

After the compact binary component has been established, a black hole in the

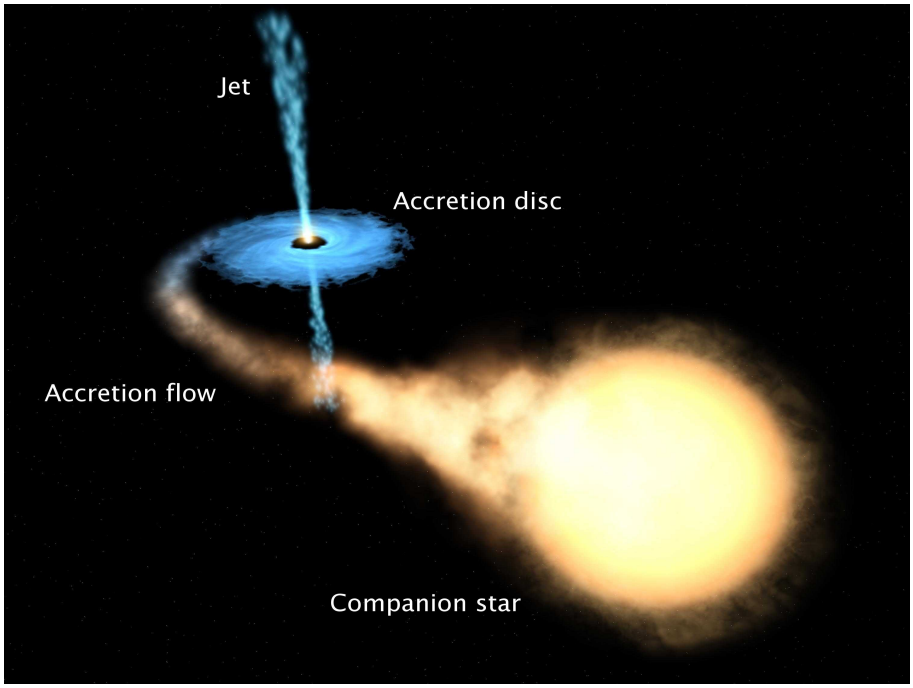

Figure 1.1: An illustration of a black hole binary system. Modified from an artist's impression, courtesy of ESA, NASA and Felix Mirabel (the French Atomic Energy Commission & the Institute for Astronomy and Space Physics/Conicet of Argentina).

case of black hole binaries, it starts to accrete matter from the orbiting companion star through the saddle point that joins their equipotentials. This saddle point is called the inner Lagrangian point, and the three dimensional critical surface of the gravitational potential around each component is known as the Roche lobe. Once the secondary star fills its Roche lobe, through e.g. stellar evolution, and reaches the inner Lagrangian point between the two potentials, matter will start flowing through towards the primary component. Since this system is rotating around its centre of mass, the accreting material has angular momentum that needs to be conserved. Thus matter cannot fall directly into the black hole, but instead forms a thin accretion disc around it (Figure 1.1).

Once the falling material has reached the disc it settles down into Keplerian

orbits with the same angular momentum it had when it passed through the inner Lagrangian point. However, dissipative processes, such as particle collisions, shocks and viscous dissipation, slowly drain energy from the orbiting material and the angular momentum is transported outwards through the disc. Near the black hole the disc terminates because there are no stable particle orbits possible in the extreme gravitational field. The innermost stable circular orbit (ISCO) is the last marginally stable particle orbit, beyond which the event horizon of the black hole becomes a dominant feature. In the standard accretion disc interpretation the disc innermost radius $R_{in} = R_{ISCO}$.

1.1.1 Accretion onto black holes

Accretion onto a compact object is the ultimate source of energy in the Universe. In a standard, steady and spherically symmetrical accretion scenario, a gas element of mass m enters the outer accretion disc and starts moving towards the black hole in circular orbits. For a black hole of mass M and radius R, the gravitational potential energy released by this gas element falling into the black hole is $\Delta E = GMm/R$, where the ratio M/R describes the compactness of the accreting object, as well as the efficiency of the energy release. The total energy released by this accretion is $L = \eta \dot{M} c^2$, where η is the efficiency of accretion and $\dot{M}$ is the mass accretion rate. η depends on the black hole spin, hence the greater the spin the higher the efficiency.

The maximum possible luminosity for an accretion-powered object is reached when the radiation pressure force is balanced by the gravitational force. This limiting luminosity is called the Eddington luminosity L_{Edd},

$$L_{\rm Edd} = \frac{4\pi G M m_p c}{\sigma_T} = 1.26 \times 10^{38} (M/M_\odot) ergs^{-1} \tag{1.1}$$

At greater luminosities the radiation pressure would exceed the gravitational force and accretion would stop in sources where accretion is the only source of luminosity.

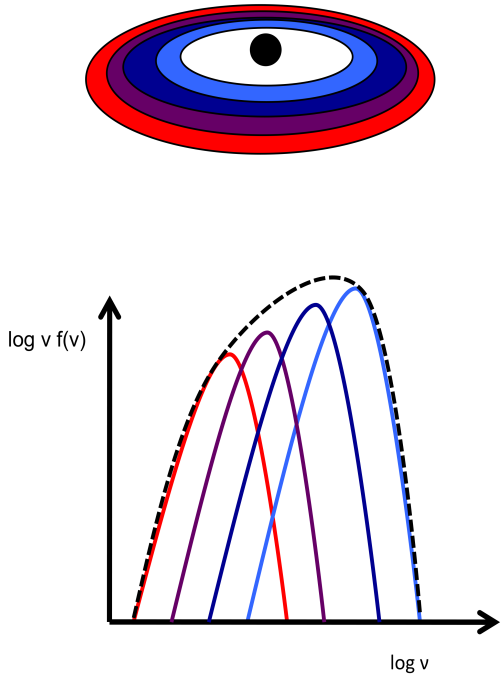

Figure 1.2: A multicolour disc blackbody, produced by blackbody emission over multiple disc annuli. The hottest blackbody component comes from the annulus closest to the black hole.

However, since this only holds for steady and spherically symmetric accretion flows, it may not always hold for accretion discs.

The classical Shakura-Sunyaev accretion disc model assumes a cool, optically thick but geometrically thin disc, balanced to a steady state by gravitational heating and radiative cooling. As the material moves inwards in the disc at rate $\dot{M}$ through an annulus with a width dR, potential energy is released at rate $dE/dt = dL_{pot} = (GM\dot{M}/R^2)\times dR$. Assuming that this thermalises to a blackbody, then

$$dL = dA\sigma_{SB}T^4 \tag{1.2}$$

where dA is the area of the emitting annulus including both sides of the disc, $dA = 2 \times 2\pi RdR$, and σ_{SB} is the Stefan-Boltzmann constant. If half of the released

potential energy is radiated following the virial theorem, then the luminosity from an annulus dR can be approximated as

$$dL_{rad} = \frac{GM\dot{M}}{2R^2}dR = 4\pi R \times dR\sigma_{SB}T^4. \quad (1.3)$$

This forms a multi-temperature (multi-colour) disc spectrum with a sum of black-body components, described by a temperature distribution $T(R) \propto R^{-3/4}$, where the temperature and luminosity increase towards the black hole (Figure 1.2).

1.2 Black hole spin

Astrophysical black holes are the simplest possible objects. They are completely described by only two parameters in general relativity, their mass and the specific angular momentum, spin. Born as a result of gravitational collapse, all black holes are in general born with a non-zero spin from the residual angular momentum of the singularity (Gammie et al. 2004).

The spin is defined as $a \equiv J/cM$, where J is the angular momentum, c is the speed of light and M the mass of the black hole. It is best expressed as a dimensionless parameter to describe the magnitude of the spin, so that $a_* \equiv Jc/GM^2$. This spin parameter is zero for a non-spinning Schwarzschild black hole, where the ISCO is at $6R_g$, (with $R_g = GM/c^2$), following the Schwarzschild metric in general relativity. For spinning black holes, however, $a_* > 0$ and the surrounding space-time is described by the Kerr metric. A maximally spinning, extreme Kerr black hole has $a_* = 1$ and the innermost stable orbit is down at $1R_g$. This also sets the radius of the event horizon, as $R_H = R_g + \sqrt{R_g^2 - a^2} = R_g(1 + \sqrt{1 - a_*^2})$. In order for the black hole to exist, a_*^2 in the last term must be ≤ 1 (Kato et al. 1998). However, the radiation emitted by the disc and swallowed by the black hole produces a counteracting torque that sets a steady state limit of $\sim$0.998 for all accreting black holes, with $R_{in} \sim$

$1.24R_g$ (Thorne 1974). In theory, black holes can spin up through mass accretion. In stellar mass black hole binaries, however, the companion star is usually too small for the mass transfer to produce any significant changes to the spin even if all the mass of the secondary was to be accreted by the black hole.

In stellar-mass black hole binary systems the black hole spin and the accretion disc angular momentum are usually parallel, but retrograde spins with $-1 \leq a_* < 0$ are possible for super-massive black holes in active galactic nuclei (Fanidakis et al. 2011). In this thesis I will only discuss phenomena associated with prograde spins.

1.2.1 Astrophysical relevance

One of the clearest manifestations of black hole spin is its strong coupling with the accretion disc. The spin sets the position of the last stable circular orbit around an accreting black hole, pulling the accretion disc farther in the faster it spins (Figure 1.3). This causes the inner regions in the disc to be subjected to stronger relativistic effects and makes the disc more luminous by increasing the efficiency of the black hole.

The spin might also offer an insight to other astrophysical phenomena. Its correlation with jet power is currently a controversial issue, mainly due to uncertainties in converting observed radio fluxes to jet power (see e.g. Fender, Gallo & Russell (2010) vs. Narayan & McClintock (2012)). This possible correlation does not mean that the spin has to be the origin of the jet, but solving the spin–jet connection could play a crucial part in finally solving the jet launch mechanism.

The spin also plays an important role in galaxy mergers. When two galaxies with differently/oppositely spinning active galactic nuclei (AGN) come within close proximity of each other, the encounter can result in one of the central black holes being kicked out of the system instead of merging into an even more supermassive black hole (King et al. 2008).

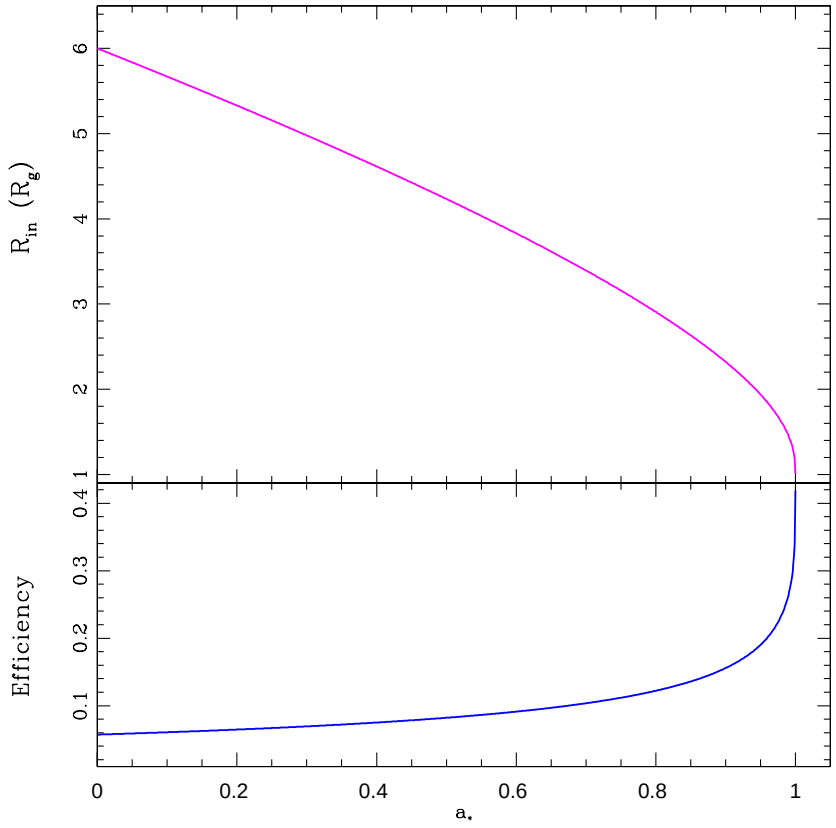

Figure 1.3: The disc inner radius R_{in} and the radiation efficiency of the black hole, plotted against the (prograde) spin parameter a_*.

Efficiency

Another astrophysical relevance of the spin is the increased radiation efficiency of the black hole. The specific energy of a particle rotating in the innermost circular stable orbit R_{in} can be expressed as $E_{ISCO} = c^2\sqrt{1-(2R_g/3R_{in})}$, where $R_g = GM/c^2$ is the gravitational radius. Assuming that all photons emitted by the disc escape the black hole to infinity, the total amount of gravitational energy that can be released between R_{ISCO} and infinity is the same as the specific binding energy of the last stable orbit, $c^2 - E_{ISCO}$. The binding energy of the last stable orbit increases with spin, thus increasing the efficiency of converting the rest-mass energy into radiation such that

$$\eta = 1 - \frac{E_{ISCO}}{c^2} = \begin{cases} 1 - \sqrt{8/9} = 0.057 & \text{for } a_* = 0 \\ 1 - \sqrt{1/3} = 0.420 & \text{for } a_* = 1 \end{cases} \tag{1.4}$$

The capture of photons decreases this efficiency by only a small amount for both Schwarzschild and extreme Kerr black holes. However, for a spin of 0.998 the actual maximum possible efficiency of a black hole is close to 30 %, thus significantly lower than for the theoretical $a_* = 1$ (Thorne 1974). Figure 1.3 shows the trend in efficiency as a function of spin.

1.2.2 Measuring the black hole spin

Black hole spin is currently a controversial topic in astrophysics, as it leaves a mark on space-time only very close to the event horizon, which makes it very difficult to measure. In the past few decades astrophysical research has led to reliable measurements of black hole masses through dynamical studies, but until recently reliable spin measurements have remained out of reach.

There are currently two observational methods to determine the black hole spin; either by fitting the intrinsic continuum spectra from the accretion disc, or by

analysing the secondary reflection features. The first method is based on the peak temperature T_{max} and luminosity L_{disc} of the accretion disc. These both increase with the mass accretion rate $\dot{M}$ while the disc inner emission region (and hence the disc inner radius, Figure 4.8) stays constant. The disc continuum fitting method is widely considered to be a relatively robust way to determine the black hole spin, but large uncertainty comes from the fact that the derived spin values depend heavily on the binary parameters being accurately known (see Section 1.3).

The second method uses the profile of the Fe K_α line, produced by fluorescence in the X-ray illuminated accretion disc. The faster the black hole spins, the further down the accretion disc can extend and the stronger the relativistic effects which broaden the line. The width of the line is set by the line emissivity, together with the strength of the gravitational field and inclination of the disc. All these essential parameters (inclination, disc inner radius and emissivity) can be constrained directly from spectral fitting, which in theory makes this method more widely usable. However, unlike the disc in the disc-dominated spectra, the line is only a small feature on the total spectrum, which means it can be very difficult to constrain. The line profile is also highly dependent on the ionisation of the material and the way the reflected and underlying continua are modelled (see Chapters 3 & 4).

1.3 Spin from accretion disc spectra

Since the location of the innermost stable orbit around the black hole depends on the black hole spin, studying the accretion disc provides a direct link to determining the spin. The area of the emitting region in the inner disc can be estimated from the observed peak temperature T_{max} and luminosity of the disc L_{disc}, both of which peak close to the innermost stable orbit R_{ISCO}. Data from bright black holes show a clear $L - T^4$ relation at high mass accretion rates (Kubota et al. 2001, Gierliński & Done 2004), which, based on Equation 1.2, implies that the innermost emitting area of the

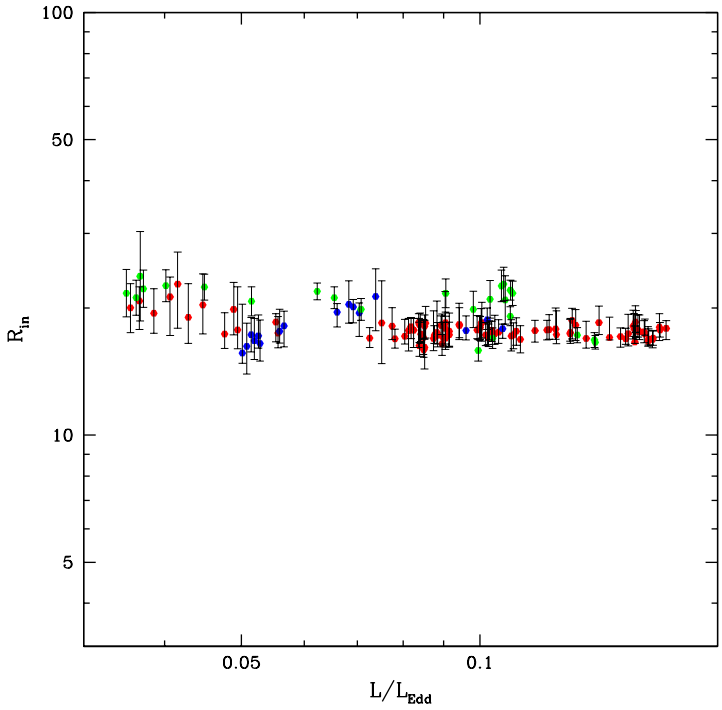

Figure 1.4: The apparent disc inner radius R_{in} measured from the disc dominated spectra of the Galactic black hole binary GX 339-4. The inner radius stays relatively constant over a range of luminosities for nearly a decade. The different colours refer to different outbursts during 2002–2010.

disc stays constant. This means the radius R of the emitting area stays constant over a range of luminosities, as seen in Figure 1.4. Thus equation 1.3 can be used to derive R_{in} from the observed T_{max} and L_{disc} by using $\sigma_{SB}T_{max}^4 = \sigma_{SB}T^4(R_{in}) = L_{disc}/(4\pi R_{in}^2)$, so that

$$R_{in} = \frac{L_{disc}}{4\pi\sigma_{SB}T_{max}^4} \tag{1.5}$$

Finally, converting this observed inner radius into gravitational radii $r = R_{in}/R_g$ gives a way to observationally measure the black hole spin. However, this method

is highly dependent on the binary system parameters. Converting the observed X-ray flux to luminosity requires knowledge of the distance to the source, and the measured inner radius relates to the system parameters as $R_{in}^2 \propto D^2/(M^2 cos(i))$. Thus converting the disc inner radius to spin is difficult even in the best constrained binary systems. A good example of this is the black hole binary LMC X-3. Its distance in the Large Magellanic Cloud is measured at 52 kpc (di Benedetto 1997), and the black hole mass has been constrained between $7 - 9 M_{\odot}$ (Cowley et al. 1983, Soria et al. 2001), with a disc inclination between 50–67° (Cowley et al. 1983). Even with these relatively small ranges in system parameters, however, the spin can only be constrained between $a_* = 0 - 0.7$ (Kubota et al. 2010).

The total luminosity has to be dominated by the disc emission, as the $L - T^4$ relation breaks when the disc component gets weaker and the tail stronger. Therefore the most reliable way is to use the disc dominated soft state spectra where non-thermal emission is just a small fraction of the total luminosity (Section 1.3.2 below).

Using this constant size scale of the emitting region to estimate the radius is somewhat more complex than this, but sophisticated theoretical models now exist. They are discussed in more detail below and in the later chapters, but in summary they include both the fully relativistic expression for the energy release as a function of radius, full vertical radiative transfer through the self-consistently determined ionisation structure of the disc and special and general relativistic effects from propagation of this emission to the observer.

1.3.1 Corrections to the simple disc solution

Even though the Shakura-Sunyaev disc model is widely used as an approximation, real accretion discs are more complex, and thus several corrections are needed to help the disc approximation. For one, it does not include a fully relativistic stress-free inner boundary condition. The widely used simple disc model DISKBB has no bound-

ary condition implemented, which means that the disc temperature peaks at the last stable orbit. Including a boundary condition means that the temperature actually peaks at larger radii and is therefore somewhat lower (Pringle 1981; Gierliński et al 1999). Secondly, the emission from each radius is only a true blackbody if the disc is effectively optically thick to absorption at all frequencies. However, the continuum (free-free) absorption drops as a function of frequency, which means that the higher energy photons in each radius are unlikely to thermalise. This forms a modified blackbody, where a colour temperature correction $f_{\rm col}$ is needed to compensate for the incomplete thermalisation. Hence, effective temperature is a factor of f_{col} higher than for a true blackbody, being best-fitted roughly in the range of $1.7 \leq f_{\rm col} \leq 2.0$ (Shimura & Takahara 1995).

In addition, the intrinsic spectrum is emitted from material which is rapidly rotating in a strongly curved spacetime, so it is smeared by the combination of special and general relativistic effects similar to the iron line emission (Section 1.4.1). This broadens the spectrum from each radius, giving a noticeably different shape to the sharp Wien drop at the highest energies (e.g. Cunningham 1975; Zhang et al. 1997).

Finally, even after all these corrections to the disc spectrum, the basic assumption that the local spectrum at each radius has a modified blackbody shape is only an approximation to the full radiative transfer scenario. Photo-electric (bound-free) absorption from partially ionised metals becomes significant especially at high frequencies, where the free-free absorption drops. This effect is highlighted by the radiative transfer through the vertical structure of the disc, and while these spectral features are smeared by the special and general relativistic effects, they still result in a broader spectrum than predicted by the simpler models (Davis et al. 2005).

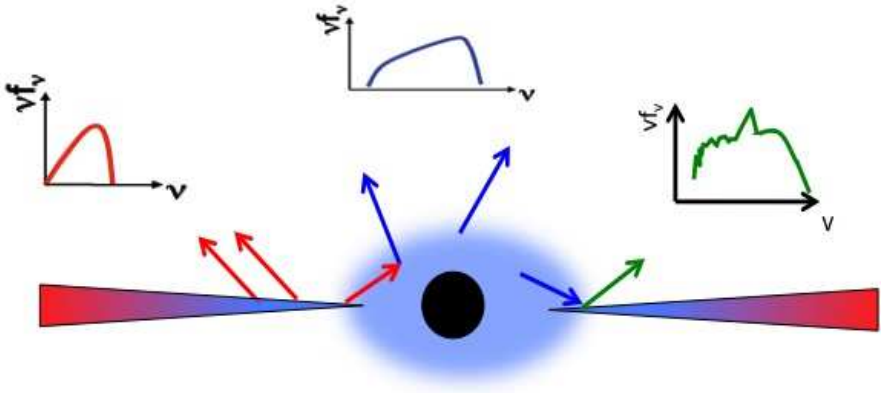

Figure 1.5: Primary and secondary components in the time-averaged energy spectrum. Emission from the accretion disc is illustrated in red, with a blackbody shaped spectrum component. A portion of these seed photons is Comptonised by the hot plasma in the black hole corona, showing a power law shaped component (in blue). Secondary reflection features (in green) sit on top of these primary components, with a strong iron emission line as the signature characteristic.

1.3.2 Time-averaged energy spectra and spectral states

Time-averaged energy spectra obtained from black hole binaries show two primary components, illustrated in red and blue in Figure 1.5. At low energies, the defining feature is a quasi-thermal blackbody-like component coming from an optically thick, geometrically thin accretion disc as described in Section 1.1.1. Above a few keV the continuum takes the shape of a power law tail, produced by either thermal (low/hard state) or non-thermal (high/soft state) Comptonisation by the high energy plasma in the black hole corona.

Even though astrophysical black holes can be described by only mass and spin, there is a third, important factor that sets the *observational* characteristics of an accreting black hole; the mass accretion rate $\dot{M}$. The emission from the accretion flow is strongly dependent on $\dot{M}$, and thus changes in this flow provide a frame to

the observed spectral states. $\dot{M}$ through the accretion disc, triggered by the disc instability, varies on timescales from minutes to years, giving also an origin to the observed long-term X-ray light curve and long term variability.

Spectral states are often classified by the contributions of the disc and the power law components in relation to the total emission, as shown in Figures 1.6 and 1.7. At high mass accretion rates the disc component dominates, and the time-averaged energy spectrum is best described as a multicolour disc blackbody, with the inner radius most likely reaching the innermost stable orbit in the line of sight. A portion of the disc photons act as the seed photons for the Compton component, forming a non-thermal tail extending to harder energies, but carrying only a small fraction of the total bolometric luminosity. The photon index is $\Gamma > 2$ when the disc is strong and tail weak. This is known as the classical high/soft spectral state (HSS) or the thermal dominated state (TDS), as the temperature peaks in the soft energy band below 2 keV at high luminosities (Figure 1.6, in green). The tail has more fast variability than the disc (Churazov et al. 2001), with the disc having almost no variability. Cases where the hard tail is extremely weak are described as ultrasoft state (Figure 1.6).

The hard X-ray tail gets gradually stronger as the mass accretion rate either increases, going into the very high state, or decreases in the hard intermediate state, before moving towards a soft-to-hard state transition. The photon index decreases ($\Gamma < 2$) as the disc gets weaker and the spectrum harder, dominated by a hard thermal Comptonised component. The spectrum peaks at high energies, above $\sim$100 keV, at luminosities $L \leq 0.02 L_{Edd}$, producing a characteristic Maxwellian roll over in the spectrum (Figure 1.6, blue). These low mass accretion rate spectra are known as the canonical low/hard state (LHS).

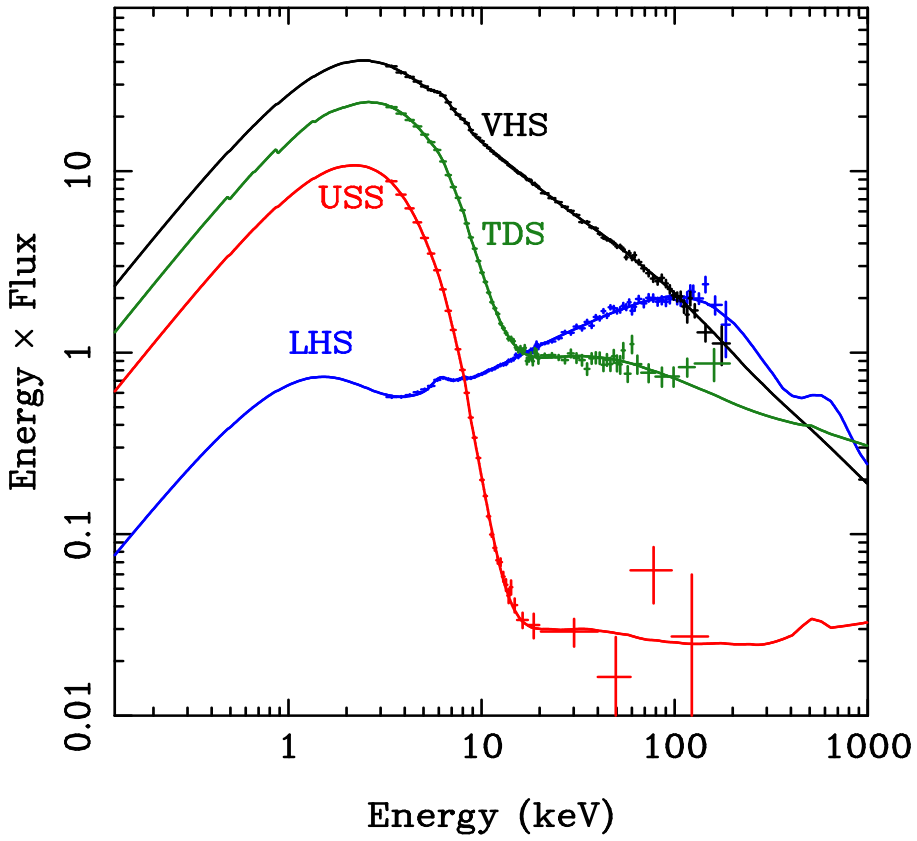

Figure 1.6: The different spectral states seen in black hole binaries, in the special case of GRO J1655-40 during its 2005 outburst (Done, Gierliński & Kubota 2007). The states seen here are the very high state (VHS), the thermal dominant state (TDS; also the high/soft state), the ultra-soft state (USS) and the low/hard state (LHS).

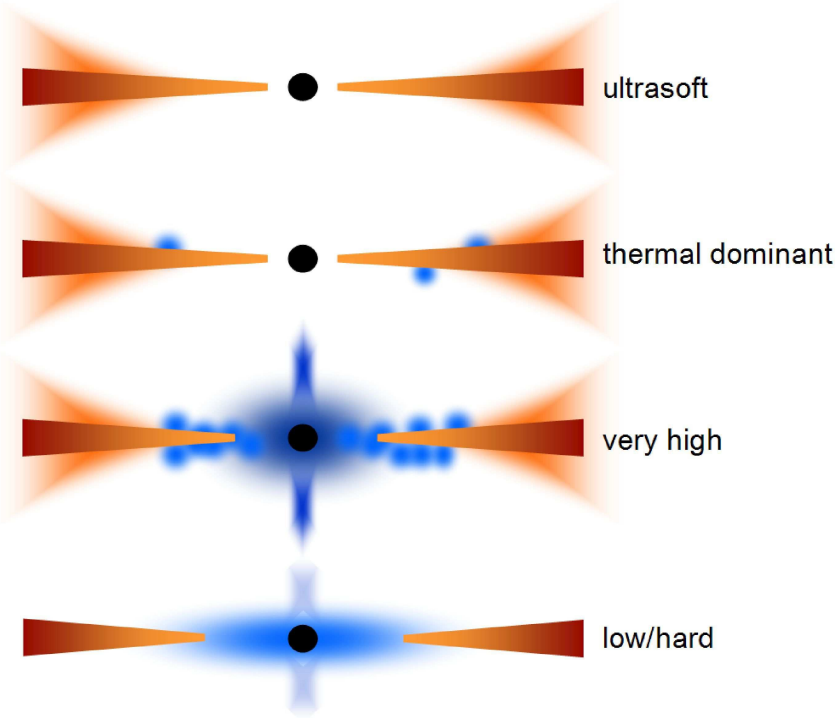

Figure 1.7: A schematic of the truncated disc model and spectral evolution explained through changes in the accretion flow, with contributions from the disc, hot inner flow, disc wind and jets (Done, Gierliński & Kubota 2007).

The truncated disc model

The low/hard and high/soft state spectra show clear distinctions in their emission spectra, which can be interpreted as due to changes in the accretion geometry. In the standard truncated disc model, the inner disc is replaced by a hot, optically thin but geometrically thick accretion flow, as pictured in Figure 1.7.

There is only little overlap with the truncated disc and the hot flow in the low/hard state, so only few seed photons illuminate the flow. Compton cooling is therefore weaker and the electrons in the flow are hot. This forms a hard, ther-

mal Comptonised spectrum, with $N(E) = N_0 E^{-\Gamma}$ and $1.4 < \Gamma < 2$. It also gives rise to the observed X-ray variability, when fluctuations from further out propagate inwards.

The observed softening of the spectra at higher luminosities can then be explained by the accretion disc slowly pushing inwards underneath the hot flow, increasing the number of seed photons. The spectrum enters the hard intermediate state, and eventually the soft and/or soft intermediate states when the disc extends further inwards. When the disc reaches the last stable orbit there is no room for the hot flow and the disc is back to a standard Shakura-Sunyaev disc (Figure 1.7).

1.4 Spin from reflection

On top of the primary spectral components seen in time-averaged continuum spectra, the intrinsic continuum is often modified by secondary processes caused by hard X-rays from the corona illuminating the cool disc. These processes are described in detail in the review by Fabian et al. (2000). What happens when a high energy photon scatters back into the disc can be described with a simplified case of hard X-rays illuminating a semi-infinite slab of cold gas. A photon entering the slab, made up of a neutral population of metals and mostly ionised hydrogen and helium, may either undergo electron scattering or photo-electric absorption, resulting in either reflection or absorption features. Absorption furthermore produces either fluorescent line emission or Auger de-excitation. In the end the photon is either destroyed by Auger de-excitation, scattered out of the slab or reprocessed into a fluorescence line and brought back into the line of sight. These processes together make up a reflection spectrum on top of an incident power law continuum, shown in Figure 1.8.

The reflected fraction increases with energy as the photo-electric cross-section decreases. Since photo-electric absorption dominates at low energies, soft X-rays are mostly absorbed into the disc, whereas higher energy photons are more likely to scat-

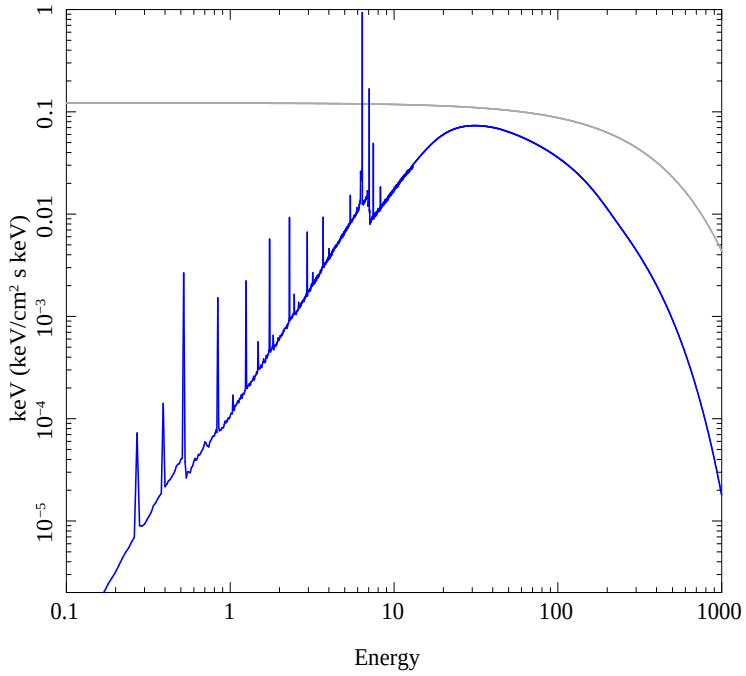

Figure 1.8: Reflection spectrum of neutral material with solar abundances (blue), with the electron scattering cross-section in grey. At low energies most of the incident photons are absorbed rather than reflected, due to the large absorption cross-section. A Compton hump is visible at ∼20–50 keV, after which Compton down-scattering becomes dominant and high energy photons are not reflected elastically. The strongest atomic feature at 6.4 keV is the Fe $K\alpha$ emission line (Done 2011).

ter out of the disc. Above ∼10 keV Compton down-scattering becomes important, making reflection non-elastic. Photons still reflect at higher energies, but lose energy in the process and emerge at lower energies than they are incident, thus resulting in a characteristic high energy break at 20–50 keV (Figure 1.8).

Characteristic reflection features in continuum spectra are mainly manifested as fluorescent $K\alpha$ emission lines from the most abundant elements, most prominent being the iron $K\alpha$ line at 6.4 keV in neutral material (Figure 1.8). The $K\alpha$ line is produced when one of the electrons in the K-shell (n=1) gets ejected following photo-electric absorption of a high energy X-ray photon. This excited state then decays when an L-shell (n=2) electron drops into the K-shell emitting the energy by either an emission line photon or an Auger electron. Iron, being the last astronomically abundant element, has the strongest impact on the observed emission as it is emitted where the fraction of reflected to incident emission is large and has the highest fluorescence probability.

The basic reflection principle described above describes the characteristics of neutral reflecting material. However, the dependence on photo-electric absorption at low energies also makes reflection highly sensitive to the ionisation state of the reflecting material. This is parameterised by

$$\xi = \frac{L}{nr^2} \tag{1.6}$$

where L is the ionising luminosity, n is the proton density and r is the distance to the central source. The charge imbalance in an ion means all the electrons are more tightly bound, so a higher ionisation state increases the energy of both the photo-electric threshold and the $K\alpha$ fluorescence line. The optical depth τ is a key parameter in atomic absorption, and hence determines how much of the fluorescence line escapes. This strongly depends on the cross-section $\sigma(E)$ such that $\tau = \sigma(E)N_H$, where N_H is the hydrogen column density. A higher ionisation state reduces the

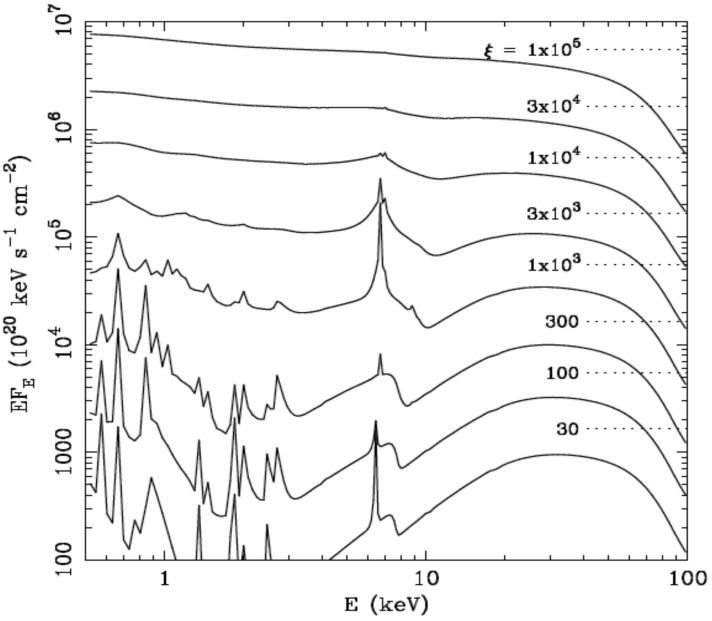

Figure 1.9: Reflection spectra from ionised material at different ionisation states, with the intrinsically narrow fluorescence line and absorption edge features broadened with increasing ionisation state (Fabian et al. 2000).

overall cross-section, so increases the fraction $e^{-\tau_{T(E)}}$ of the fluorescence line which can escape. In ionised material both Compton up-scattering and down-scattering are important, so the intrinsically narrow fluorescence line and absorption edge features are broadened (see Figure 1.9).

The strength of the line is generally given in terms of its equivalent width in relation to the intrinsic emission. This depends, yet again, on the ionisation state of the reflecting material, and hence measuring it from observations using sophisticated self-consistent reflection models can prove complicated in highly ionised accretion discs. Thus the strength of these reflection features is instead often given in terms of the solid angle subtended by the reflector, $\Omega/2\pi$.

1.4.1 Relativistically broadened line profile

Neutral emission lines emitted by the X-ray illuminated accretion disc are intrinsically narrow. However, due to the proximity of the black hole, the inner regions of the disc move faster than the outer regions and are therefore subjected to stronger relativistic effects. This causes the line profiles from the inner disc to appear further broadened and shifted by Doppler shifts, relativistic beaming and gravitational redshifting.

Figure 1.10 shows a schematic on how these effects alter an observed line profile. In a non-relativistic case (top panel, Figure 1.10), each disc annulus produces a standard, symmetric line profile. This corresponds to emission from both the receding (red-shifted) side of the disc and the approaching (blue-shifted) side. The broadest parts of the line are produced in the fast-moving inner regions of the disc. This double-peaked line profile starts to reshape as the orbital velocities get mildly relativistic close to the black hole, and special relativistic beaming increases the blue peak of the profile. Both transverse Doppler shifting and gravitational redshifting move the contribution from each disc annulus to lower energies (second and third panels). Finally, summing these effects from each annulus produces a broad, distorted line profile (bottom panel).

1.4.2 Black hole spin from the Fe line profile

Theoretically, both the blue and the red wing of the line profile tell us important information about the disc. The blue-shifted part of the line is almost entirely a function of the disc inclination, and as such provides a way to determine the inclination directly from the line profile. The red-shifted part of the line, on the other hand, is a function of the inner radius of the line emitting annulus. Assuming this is also the accretion disc inner radius, the red wing gives a direct way to measure R_{in} and hence the black hole spin.

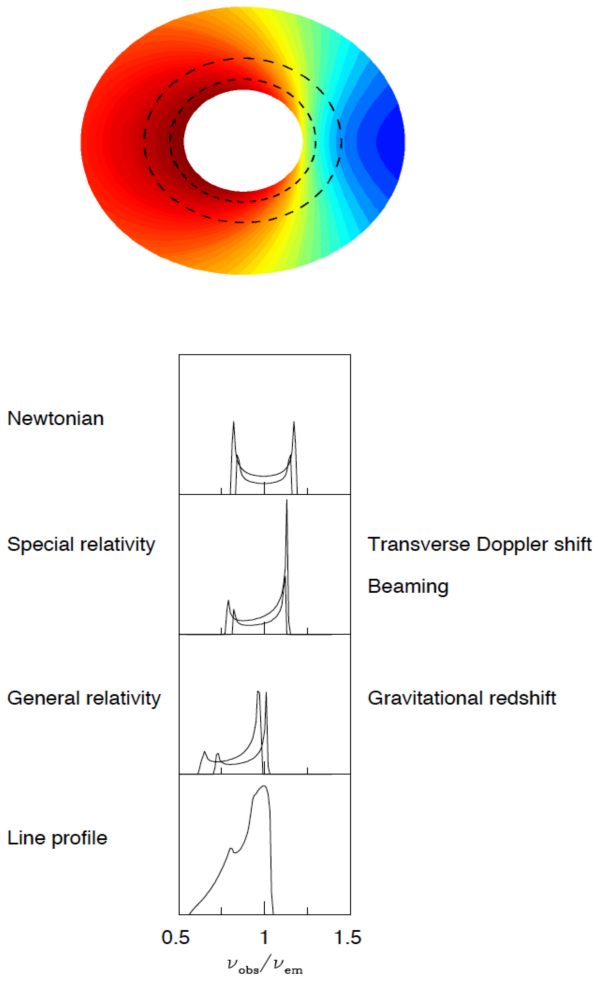

Figure 1.10: A schematic of how a relativistically broadened line profile is formed. The top panel shows a Newtonian double-peaked line profile from a non-relativistic accretion disc. Adding transverse Doppler shifting and beaming makes the blue wing of the line more profound and extends the red wing in the second panel. The third panel demonstrates how gravitational redshifting affects the line profile, and the bottom panel shows the resulting broad, skewed line profile (Fabian et al. 2000).

Observationally, measuring the disc inner radius and disc inclination directly from the line profile using spectral modelling of the time-averaged energy spectrum is not as simple as this. The observed line profile is often only a few percent feature on top of the underlying continuum, and as such, highly dependent on the way the continuum is modelled. Furthermore, the limitations in sensitivity and resolution of current X-ray satellites mean it is difficult, if not impossible, to reliably constrain both the red and the blue wing of the line at the same time. These issues will be further discussed in Chapters 3 and 4.

1.5 Overview of the black hole spin controversy

Since there are two possible ways to measure the spin in black hole binaries, it is obviously very important to compare the results from both methods to strengthen our confidence in one or both them. However, the current level of agreement is not very encouraging. The first problem is that these two techniques apply in very different conditions. The disc fitting method can only be used confidently when the disc emission is dominant, i.e. more than 80% of the total emission, whereas the iron line method requires a strong hard X-ray tail. Another problem is that even when this comparison can be done on the same source, the derived values often disagree, with the iron line method generally resulting in a higher spin value than the one derived from disc continuum fitting (Miller et al. 2004; Kolehmainen, Done & Diaz Trigo 2011). The third problem is that black hole binaries are often so bright that they have to be observed using non-standard observing modes, which are often plagued by significant instrumental uncertainties in calibration.

This thesis takes a close look at all these issues, and aims to resolve the currently existing controversy over the spin measurements. Chapter 2 introduces the disagreement over the spin in the particular case of the Galactic black hole binary GX 339−4. We use the disc continuum fitting method to derive a new, strict upper limit for the

spin in GX 339−4 and compare it with the existing iron line profile results.

Chapter 3 goes deeper into trying to resolve the discrepancy in derived spin values from the two methods at high mass accretion rate spectra, and we find that the iron line method is very much dependent on the way the intrinsic continuum is modelled. Changing the continuum model changes the shape of the iron line profile and thus the derived spin value. Our preferred continuum gives a line profile that is too narrow to constrain the black hole spin from the analysed GX 339−4 observations, indicating that the spin need not be extreme. This solves the disagreement in this particular source, but shows problems with disc models at the 5–10% level, made significant by the quality of the data.

Using this knowledge we expand our investigation to the low mass accretion rate spectra and re-analyse all archival low/hard state *XMM-Newton* timing mode observations in Chapter 4. It is clear from our analysis that using sophisticated ionised reflection models, together with continuum models motivated by timing properties of the same data, produces narrow line profiles in most of our sample spectra. Thus we find that not all low/hard state spectra have relativistically broadened line profiles, unlike widely claimed in literature.

Finally, having obtained the most sensitive X-ray data available on the disc emission at different luminosities, we test our understanding of the disc vertical structure in Chapter 5. We take advantage of the low absorption column of the black hole binary LMC X-3 to carefully test the best current theoretical disc models against the best current X-ray data. These data are the optimal set of disc dominated spectra to which to apply the most robust method in determining the black hole spin.

Chapter 2

Paper 1: Limits on spin determination from disc spectral fitting in GX 339−4

2.1 Introduction

An astrophysical black hole (BH) can be entirely described by two parameters in general relativity, its mass M and a dimensionless spin, a_*, which is 0 for a non-rotating Schwarzschild BH and 0.998 for a maximal Kerr BH. Unlike mass, spin only leaves an imprint on the spacetime very close to the event horizon, so it is much more difficult to measure. Nonetheless, it is important to constrain because it is a fundamental parameter determining the structure of the spacetime around the BH. It sets the size–scale of the last stable orbit around the BH, from $6 - 1.23R_g$ for $a_* = 0$ and 0.998, respectively, where $R_g = GM/c^2$. This determines the efficiency of conversion of mass to radiation for accreting objects, and may also determine the structure and power of relativistic jets. For BHs formed from stellar collapse then the resulting spin gives insight into the (poorly understood) supernova event (Gammie, Shapiro & McKinney 2004) and its gravitational wave signature.

Currently there are only two methods which can be used to determine spin from accreting BHs (see Reynolds & Fabian 2008; McClintock & Remillard 2006). The first uses the luminosity and temperature of the optically thick, geometrically thin

accretion disc to measure the emitting area of the inner disc, and hence its radius. This assumes that the dissipation follows that of the relativistic stress-free inner boundary condition (Novikov & Thorne 1973), an assumption which is now strongly supported by recent fully relativistic MHD simulations of thin discs with self-consistent magnetic turbulence as the origin of stress (Shafee et al. 2008).

To use this method requires that we can observe the spectrum at energies close to the peak temperature, which limits this method to stellar mass BH binaries (hereafter BHBs), as AGN discs typically peak in the unobservable far UV. Additionally, the source distance, and disc inclination (assumed to be the same as that of the binary) must be constrained, as these are necessary to transform the observed disc flux into luminosity. Similarly, the BH mass is required to convert the resulting size scale into gravitational radii. Thus this technique can only be used on a small subset of systems for which this information is available. Further restrictions are that the systems should be *dominated* by the disc emission. The method can still be applied to data with an increasing fraction of emission in the power law tail, but with increasingly large uncertainties in reconstructing the temperature and luminosity of the disc emission (Kubota et al. 2001; Kubota & Done 2004; Done & Kubota 2006; Steiner et al. 2009). A final restriction is that the source should not be too bright as the disc structure may change at luminosities approaching and exceeding the Eddington limit $L_{\rm Edd}$. The disc can puff up to become geometrically thick, advection and winds may become important, and the spectrum may also be increasingly distorted by low temperature Comptonization which can be difficult to distinguish from disc emission (e.g. GRS 1915+105: where Middleton et al. 2006 derive $a_* \sim 0.7$ compared to $a_* = 0.98$ from McClintock et al. 2006 due to differences in Comptonisation assumptions).

Within these limitations, the models including the full physics (stress-free inner boundary condition, relativistic smearing, and modelling the non-blackbody intrinsic emission from each radial annulus) are remarkably robust to changes in the disc

vertical structure from different *ad hoc* stress prescriptions (Done & Davis 2008), and all the potential uncertainties act in the same direction which is for these models to overestimate the black hole spin (Gierliński & Done 2004; Done & Davis 2008).

The second method to measure spin uses the shape of the iron line produced by fluorescence in the X-ray illuminated accretion disc. The width of the line is set by the line emissivity, together with the strength of the gravitational field, as this determines the velocity of the disc (hence the Doppler shift, beaming and time dilation) as well as gravitational redshift. All these parameters (inclination, inner disc radius in terms of gravitational radii and emissivity) can be constrained directly from spectral fitting, so this technique can be used much more widely than disc spectral fitting. Its only restrictions are that the disc is flat and in Keplerian rotation (which again becomes increasingly uncertain at luminosities approaching/exceeding Eddington) and that there are sufficient hard X-rays illuminating the disc to produce the iron line. Thus it can be used for both (sub-Eddington) AGNs and BHBs and requires no additional information about the distance and/or inclination of the system (Fabian et al. 1989; Fabian et al. 2000).

However, unlike the disc in the disc dominated spectra, the line is only a small feature on the total spectrum, which means it can be difficult to measure. The line sits on top of a reflected continuum, and the shape of both line and reflected continuum depend on ionisation of the material (Ross, Fabian & Young 2001), and the radial and vertical profile of this ionisation (Nayakshin, Kazanzas & Kallman 2001; Done & Nayakshin 2007). Other key issues are the underlying continuum shape (which can be distorted by complex absorption: L. Miller et al. 2007; 2008) and disentangling the intrinsic shape of the blue wing of the line from any absorption lines from ionised iron Kα (Done & Gierliński 2006; Done & Kubota 2006; Young et al. 2005).

Since we have two methods to measure spin it is obviously important to compare them. We would have increased confidence in both methods if they gave the same

answer for the same object. However, the very different restrictions on the two techniques mean there is a very small set of objects where both can be used. Disc dominated spectra generally have too few photons at the high energies required to produce a strong iron fluorescence line. Similarly, disc spectral fitting cannot be used on spectra with a strong tail (carrying more than 25 per cent of the bolometric luminosity) as the uncertainties in reconstructing the intrinsic disc emission become too large (Kubota & Done 2004). Thus the two methods cannot be reliably compared using the same dataset (but see Miller et al. 2009 for an attempt at this), but they can be used on the same object for a BHB with well constrained system parameters which shows spectral transitions.

To date only three objects have good spin estimates from both methods, where 'good' is defined as derived from fits with the best currently available models i.e. BHSPEC for disc spectral fitting (Davis et al. 2005) and CDID for ionised reflection (Ross & Fabian 2005). The results are not encouraging. The spin estimates match well only for XTE J1550-564, are somewhat discrepant for 4U 1543-475, and are quite significantly different for GRO J1655-40 (see Section 2.6.3).

It is clearly important to expand the sample of objects for which this comparison can be made. GX 339−4 is one of the best studied BHBs in terms of iron line profile from three separate data sets, spanning a range of spectral states (Miller et al. 2004; 2006; 2008; Reis et al. 2008). Two of these datasets have issues with pileup, which distorts the line (Done & Diaz-Trigo 2010; Yamada et al. 2010), but results from the third dataset alone indicate a very high spin, with $r_{in} \sim 1.8$ or 2 depending on the detailed emissivity profile, requiring $a_* = 0.96$ or 0.935 (Reis et al. 2008) and an inclination of $\sim 20°$.

Here we apply the disc spectral fitting method and find that, despite the poorly known system parameters, such high spin is unlikely to match the observed temperature and luminosity of the disc dominated spectra from this source.

2.2 System parameters

Measuring spin from disc spectral fitting requires that the system parameters (mass, distance and inclination) are reasonably constrained. Without relativistic effects, the disc luminosity relates to the inclination via $L \propto 2\pi D^2 F/\cos i \propto A T_{\rm disc}^4$, where D is distance, F is the observed flux and $A = 2\pi r_{in}^2 R_g^2$ sets the size scale for the emission from the inner disc. Thus $r_{in}^2 \propto D^2/(M^2 \cos i)$. Increasing D/M and increasing inclination means larger r_{in} and hence smaller spin.

The binary parameters are more easily determined in X-ray quiescence, when the compact object is faint so that the secondary star can be seen. The spectral type then gives distance, while the ellipsoidal variations give the mass and inclination. Alternatively, the mass and inclination can also be constrained from outburst data, by tracking periodic shifts in the line emission from the X-ray irradiated star (Casares 2007).

For GX 339−4, the continuum from the secondary star cannot be clearly seen even during quiescence but detection of the line emission in outburst gives a mass function of $5.8 \pm 0.5\ M_\odot$ (Hynes et al. 2003, hereafter H03). We review constraints on the mass, distance and inclination below, and then consider a representative selection of these values in order to explore their impact on the derived BH spin.

2.2.1 Distance, mass and inclination

Since the distance cannot be constrained by the companion star, it is instead estimated from the Na D absorption along the line of sight to the source. This gives $D \geq 6$ kpc, with distances as large as 15 kpc allowed, which would place GX 339−4 on the far side of the Galaxy (Hynes et al. 2004). Zdziarski et al. (2004) (hereafter Z04), show that the Na D absorption to GX 339−4 is similar to that seen towards OB stars in the galactic bulge, so suggest that it is more likely that GX 339−4 is at $D = 8$ kpc. Thus we take $6 < D < 15$ kpc as our range in distance, but this is

probably too conservative as the companion star is likely to be seen at a distance of 6 kpc (Muñoz-Darias, Casares & Martinez-Pais 2008)

The mass function gives a lower limit to the mass of 5.3 $M_{\odot}$ (H03). However, this is too conservative considering the companion star. This must fill its Roche lobe, which is only possible with a long orbital period for a somewhat evolved star. Muñoz-Darias, et al. (2008) look in detail at these constraints, and argue for a stripped giant companion star with mass $M_2 \geq 0.166\ M_{\odot}$, giving a solid lower limit to the black hole mass of 6.2 $M_{\odot}$. Conversely, the largest mass black hole in a low mass X-ray binary is GRS 1915+105 at $14 \pm 1 M_{\odot}$. Thus we consider the range $5.8 - 15\ M_{\odot}$ to be conservative, but note that $6.2 - 15\ M_{\odot}$ is more likely.

There is a strong constraint from the lack of eclipses that $i < 80^{\circ}$ (H03). However, the long orbital period and consequent large disc mean that this source almost certainly has a strong equatorial disc wind in its high luminosity states. These give strong ionised absorption lines when viewed at high inclinations ($i > 70^{\circ}$). There are ionised absorption features seen in GX 339−4, but these are much weaker than seen in the high inclination objects (Miller et al. 2004). This argues for an intermediate outer disc inclination, somewhat less than 70°, but not so much lower that the equatorial wind does not intercept the line of sight. Thus the outer disc (which should have the same inclination as the binary orbit) must have an inclination $\approx 50^{\circ} - 70^{\circ}$. The upper limit to this range is similar to the hard limit on the orbital inclination of $i > 45^{\circ}$ that comes from putting the maximum BH mass of 15 $M_{\odot}$ into the H03 mass function with the minimum companion star mass of 0.166 (Muñoz-Darias et al. 2008).

However, it is the inner disc inclination which is important for determining spin, and this can be misaligned from the binary/outer disc if the BH spin is misaligned. There is a weak observational constraint on the inner disc inclination of $i < 70^{\circ}$ from the fact that there are no high frequency QPOs detected in this source (Schnittman, Miller & Homan 2006), and a strong requirement from the iron line fits at $i \sim 20^{\circ}$

M ($M_\odot$)	d (kpc)	i (deg)	
5.8	6	20	H03
10	8	60	Z04
10	6	40	GN06
15	6	45	Max

Table 2.1: The parameter sets used in this paper. The abbreviations refer to papers referenced in the text and are explained in Section 2. The inclinations are mostly indicative, chosen to allow a wider limit range.

(Miller et al. 2008). However, this would require a large misalignment angle of more than 25° between the BH spin and orbit. Such large misalignments can only be produced from a very asymmetric supernova, and the resultant large kick is likely to unbind the orbit (Fragos et al. 2010). Thus while we consider the range $20° < i < 70°$, the more likely lower limit is 45° from the small misalignments required to form the binary (Fragos et al. 2010).

2.2.2 Parameter sets

From the ranges given above, we select some example system parameter sets in order to illustrate the impact on derived spin. Previous work on GX 339−4 by Gierliński & Newton (2006) argued for 10 $M_\odot$, $D = 6$ kpc and $i = 40°$ (hereafter termed GN06), as this gave similar transition properties to other BHBs. Zdziarski et al. (2004) used 10 $M_\odot$, $D = 8$ kpc and $i = 60°$ (hereafter termed Z04). The highest spin values will be found from the lowest D/M so $M = 15$ $M_\odot$, $D = 6$ kpc and lowest inclination, set to the more likely limit of 45° (hereafter termed Max). However, we also consider a parameter set with $i = 20°$ for the minimum BH mass and distance of 5.8 $M_\odot$, $D = 6$ kpc (hereafter termed H03).

2.3 Data analysis and selection of disc dominated spectra

GX 339−4 has been widely observed with NASA's *RXTE* satellite since its launch in 1995, and shows multiple dramatic outbursts covering all spectral states (Remillard & McClintock 2006; Done, Gierliński & Kubota 2007, hereafter DGK07). We use data from the last three outbursts of GX 339−4, namely the 2002/2003, 2004 and 2007 outbursts, where hard to soft state transitions could be observed. Data reduction was done using the standard *RXTE* data analysis methods. We add a systematic uncertainty of 1% to all the PCA spectra, and fit from 3–20 keV.

We follow the approach of Done & Gierliński (2003) in fitting the spectra with a simple multicolour disc (DISKBB) plus thermal Comptonization (THCOMP), with a Gaussian line (GAU, constrained in energy between 6–7 keV) and smeared absorption edge (SMEDGE, constrained in energy between 7–9 keV) added to approximate the effects of reflection. The hydrogen column density was fixed at $N_{\rm H} = 6 \times 10^{21}{\rm cm}^{-2}$ (Zdziarski et al. 2004). We use these results to make hardness-intensity diagrams, and select only disc dominated spectra for spectral fitting (defined as those with HR ≤ 0.2, which corresponds to spectra where the disc contains more than 80 % of the total luminosity).

2.4 Simple disc models

Within the limitations of disc spectral fitting discussed in the introduction, an indication of the black hole spin can be derived from fitting the very simplest disc model, DISKBB (Mitsuda et al. 1984), to the data. To illustrate that these disc dominated spectra not only look like a disc, but vary like one too, we first use the simple DISKBB fits above and plot bolometric, unabsorbed disc flux from the models against temperature in Fig 2.1. Plainly the data are consistent with $L_{\rm disc} \propto T_{\rm disc}^4$

relation, as expected from a constant inner size scale set by the last stable orbit. This observation gives a foundation for the more physical disc models described in Section 5.

To use these data to derive the size of this inner radius is more challenging than simply converting flux to luminosity via the system parameters discussed in Section 2. The derived luminosity is also dependent on inclination through relativistic effects, with Doppler boosting amplifying the observed flux at high inclinations. These relativistic effects also change the observed temperature with Doppler blueshift dominating at high inclination while redshifts from time dilation and strong gravity dominate at lower inclinations. The effect on both temperature and luminosity is small at $i = 60°$ for $a_* = 0$, but the much stronger relativistic effects at $a_* = 0.998$ mean that red and blueshifts approximately cancel at an inclination of $i = 75°$ (Zhang et al. 1997).

We follow Gierliński & Done (2004) and correct the *data* for these relativistic distortions, to derive an 'intrinsic' temperature and luminosity for each parameter set assuming $a_* = 0$. We use the correction factors tabulated by Zhang et al. (1997), interpolated in $\cos i$ using a cubic. Figure 2.2 shows these corrected data for $a_* = 0$.

Even though the simple disc models are widely used as approximations, the true inner disc is much more complicated. The DISKBB models assumes a temperature distribution $T(r) \propto r^{-3/4}$, so does not incorporate the relativistic stress-free inner boundary condition. Similarly, each annulus of the disc does not emit a true blackbody. The continuum (free-free) absorption drops as a function of frequency, which means that the higher energy photons in each radius are unlikely to thermalise. The emission instead can be described as a modified blackbody, characterised by a colour temperature which is a factor $f_{\rm col} = 1.6 - 2$ (Shimura & Takahara 1995) above the blackbody emission. We incorporate both these correction factors in the lines overlaid on Fig 2.2. (see Gierliński & Done 2004), for the expected size scale of $6R_g$ for $a_* = 0$. These show that the derived spin will be dependent on the assumed system

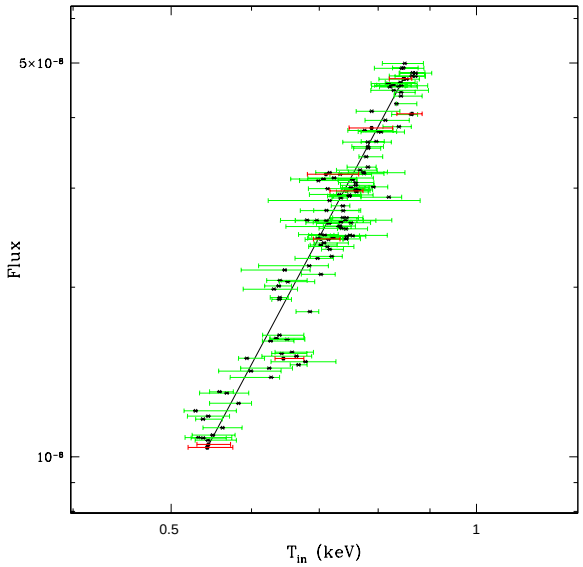

Figure 2.1: The bolometric disc flux versus the inner disc temperature from fitting DISKBB to the disc dominated spectra from GX 339−4. The solid line illustrates the $T^4_{\rm disc}$ relation and the red dots indicate the 9 spectra chosen for simultaneous fitting in Section 5.1.

parameters. The system parameters of Z04 appear consistent with zero spin, while H03, GN06 and Max are progressively further from the $a_* = 0$ prediction, indicating higher spins.

2.5 A more physical model for the disc

Even after all the corrections to the disc spectrum, the assumption that the spectrum has a modified blackbody shape is still just an approximation to the full radiative transfer scenario. Photo-electric (bound-free) absorption from partially ionised metals becomes significant especially at high energy frequencies, where the free-free absorption drops. This effect is highlighted by the radiative transfer through the

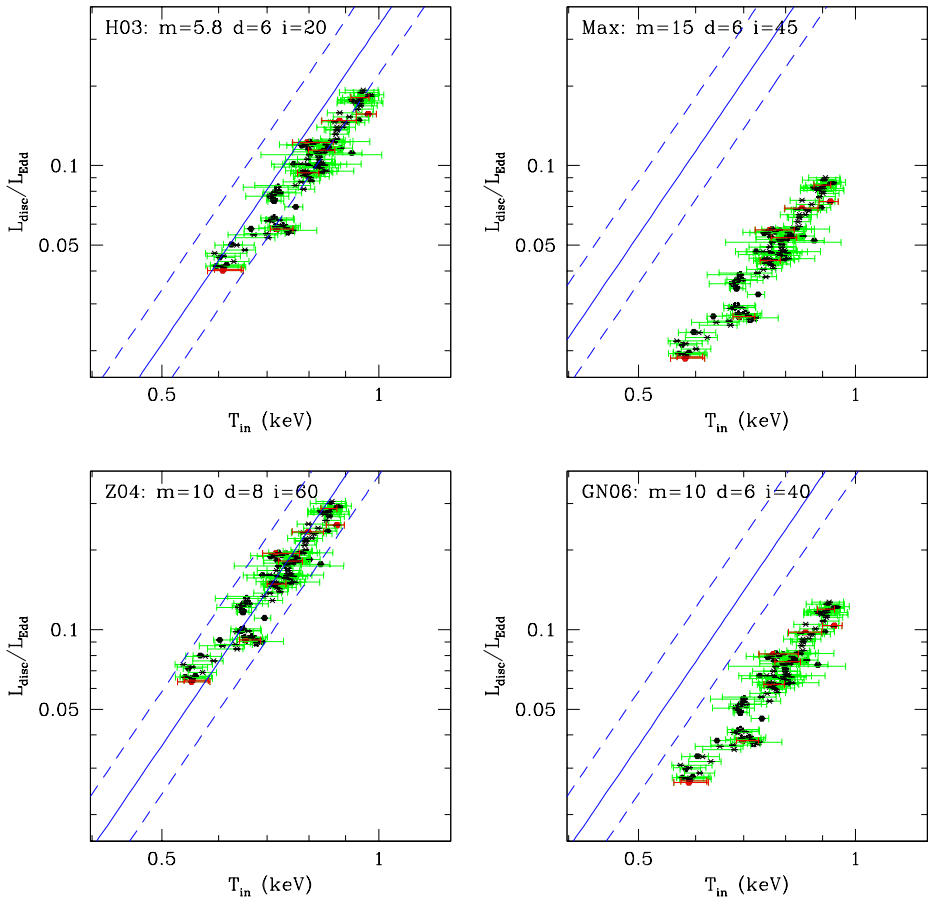

Figure 2.2: The $L - T^4$ relation in GX 339−4 with the different system parameter sets detailed in Table 1. The lines refer to $f_{\rm col}$ values of 1.6, 1.8 and 2.0 for $a_* = 0$. The solid line marks the best estimate of $f_{\rm col} = 1.8$.

vertical structure of the disc, and while these spectral features are smeared by the special and general relativistic effect, they still result in a broader spectrum than predicted by the simpler models. We use the BHSPEC model by Davis et al. (2005) which includes stellar atmosphere-like calculations to calculate the vertical structure and radiative transfer of disc annuli, and incorporates the self-consistent relativistic radial dissipation profile (stress-free inner boundary condition for any a_*: Novikov & Thorne 1976) and fully relativistic transport to produce the observed spectrum.

This model is described by the physical parameters of mass, spin, distance, inclination and mass accretion rate, parameterised as $L/L_{\rm Edd}$ (so the corresponding mass accretion rate depends on the black hole spin). Thus there is no effective temperature to use as input into the Comptonisation for the seed photon energy. Instead we fix this at the best fit inner disc temperature derived from the previous DISKBB models.

The large number of datasets means that simultaneous fitting for a_* across all the spectra is not feasible. Instead, we fit each spectrum separately with a_* fixed at 0, then average all the individual χ^2. We then repeat this for a_* fixed at 0.1, 0.2 etc up to 0.998. Fig 2.4 shows these χ^2 versus spin for the four parameter sets. The plots show a rough position for the minimum χ^2 i.e. best fit spin for each particular set of parameters. As is quite clear from Figure 2.4, the best-fit values for a_* vary significantly with the different parameter sets. Z04 gives a best fit of $a_* = 0$ as indicated by the simple DISKBB fits above, while H03, GN06 and Max have a best fit of ~ 0.7, 0.8 and 0.9, respectively. All these best fits have very similar χ^2, so these very different spin values obtained from the very different parameter sets cannot be distinguished by spectral fitting.

2.5.1 Simultaneous spectral fitting

After fitting all the spectra individually, we chose 9 spectra which together represent the full scale of the flux (marked by the red points in Figure 2.1). These 9 spectra were then fitted together simultaneously with the four different sets of system parameters. However, this time the spin parameter a_* was tied between the datasets, and fit explicitly. This allows us to explore the complex effects of inclination directly, by deriving spin for three different inclinations, 20°, 40° and 60°. The results are plotted in Figure 2.4 and the unfolded spectra are plotted with the simple diskbb+thCompml model at different luminosities in Figure 2.5.

The inclinations are illustrated with different colours for easy comparison; the smallest inclination angle (20°) is marked with green, 40° with red and the largest angle, 60°, with blue. As is clear from all the fits, increasing inclination angle decreases the spin. This simultaneous spectral fitting gives the same results as the multiple individual fits for the same inclination angle, but gives higher resolution around the spin value e.g. for H03 the minimum appears rather shallow, extending from 0.6–0.8, whereas in the simultaneous fits it is clear that for $i = 20°$ then $a_* = 0.7$ is the best fit. For Max, an inclination of 20° gives $\chi^2 > 400$ so is not included in the plot. This is because for such a low inclination, this would imply an emitting area smaller than that from maximal spin. Similarly, $i = 60°$ is not shown on H03 as this would imply such a large emission area as to require retrograde spin.

Assuming the inner disc inclination is the same as the orbital inclination, then the lower limit of $\sim 45°$ implies that $a_* < 0.9$ for any reasonable mass ($< 15 M_\odot$) and distance (> 6 kpc). Any lower mass and/or larger distance and/or higher inclination will give lower spin.

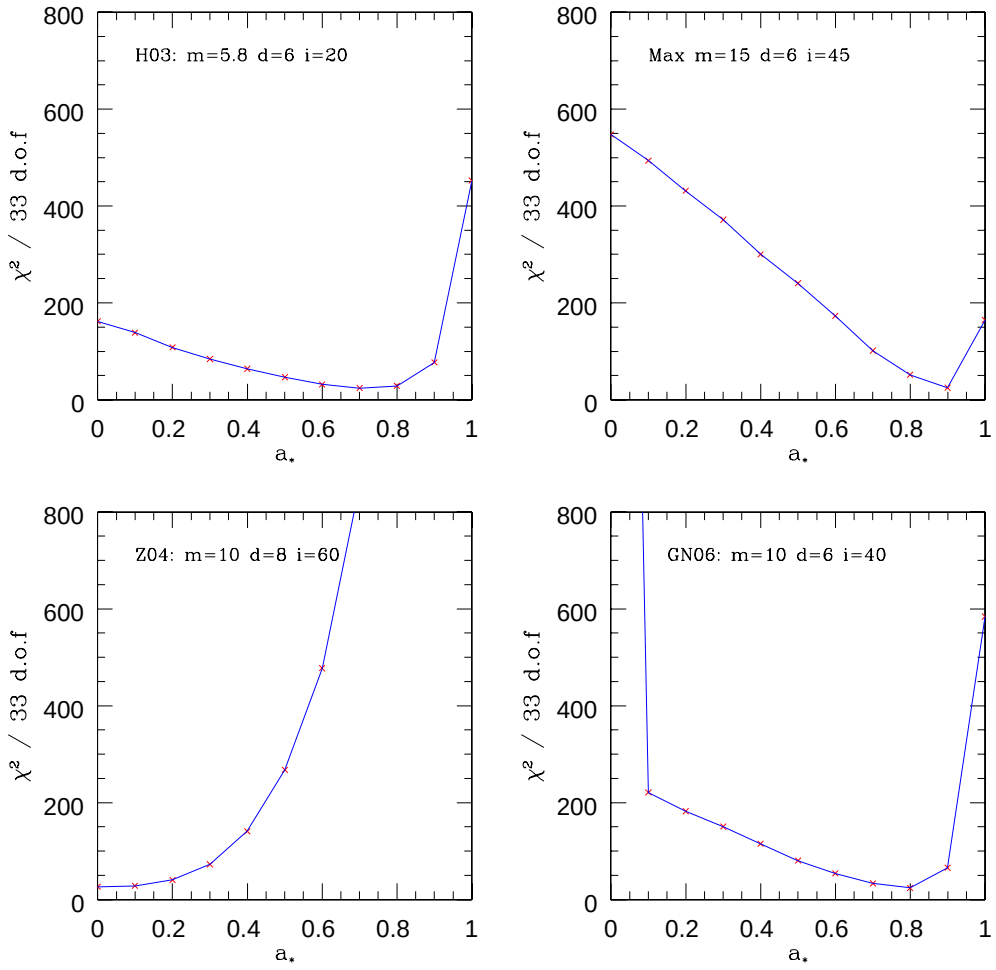

Figure 2.3: The individual spectra best-fit χ^2 values with fixed a_*.

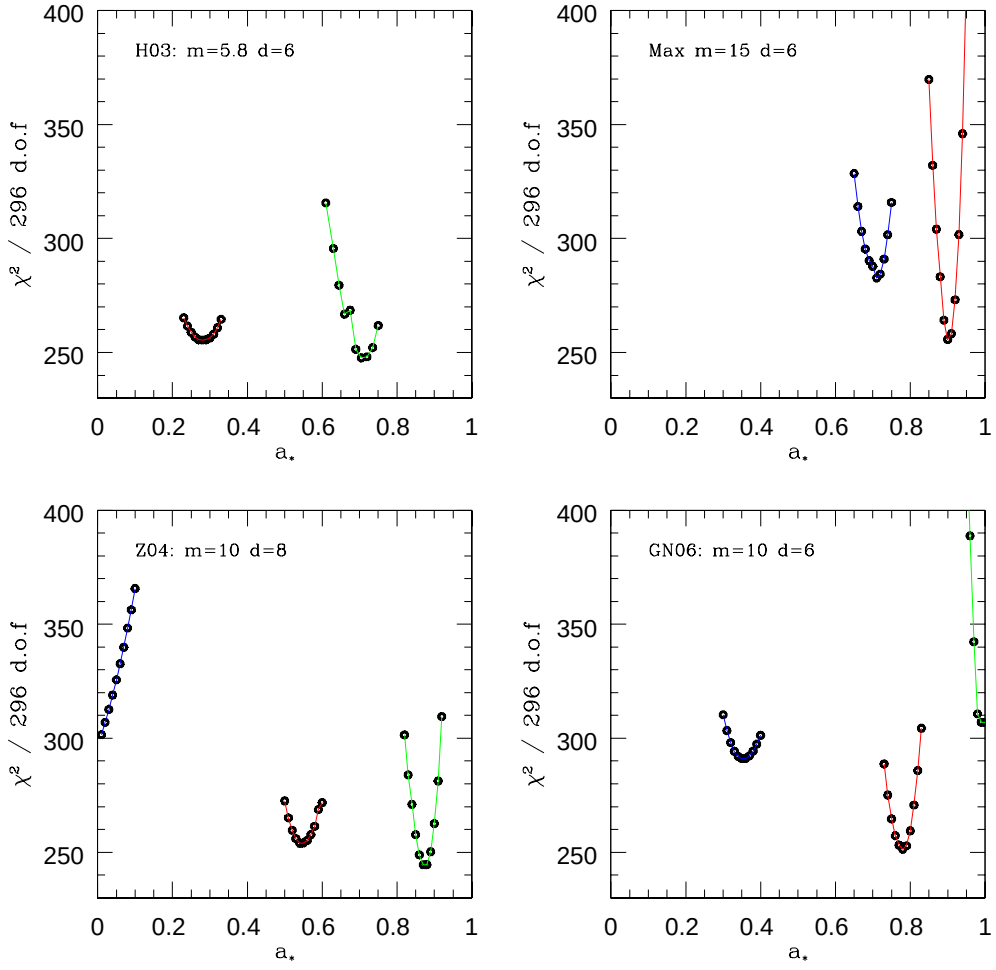

Figure 2.4: The 9 spectral fits for a_* with different inclinations. The green colour indicates $i = 20°$, red $i = 40°$ and blue $i = 60°$. a_* clearly increases with decreasing inclination.

Parameter set	i	a_*	χ^2/ 297 d.o.f
H03	20°	$0.711^{+0.017}_{-0.013}$	246.62
M= 5.8 $M_\odot$	40°	$0.282^{+0.028}_{-0.027}$	255.43
D= 6 kpc	60°	0.000 (hard limit)	1010.74
Z04	20°	$0.874^{+0.010}_{-0.010}$	243.75
M= 10 $M_\odot$	40°	$0.540^{+0.026}_{-0.012}$	253.85
D= 8 kpc	60°	$0.000^{+0.006}_{-0.000}$	297.10
GN06	20°	$0.985^{+0.014}_{-0.002}$	302.49
M= 10 $M_\odot$	40°	$0.780^{+0.015}_{-0.013}$	251.35
D= 6 kpc	60°	$0.355^{+0.024}_{-0.023}$	291.23
Max	20°	0.998 (hard limit)	37480.59
M= 15 $M_\odot$	40°	$0.946^{+0.005}_{-0.004}$	244.15
D= 6 kpc	60°	$0.710^{+0.009}_{-0.010}$	287.64

Table 2.2: The results for the simultaneous spectral fitting showing the best-fit a_* values with different inclinations.

2.6 Discussion

2.6.1 Spin from disc spectral fitting

There is a hard upper limit on spin of $a_* < 0.9$ from the disc spectral fitting, assuming that the inner disc inclination is the same as that of the orbit. Our upper limit is very conservative as it is quite unlikely that the system parameters are all at their extreme values, and in fact a distance of 6 kpc is inconsistent with a 15 $M_\odot$ black hole. At 6 kpc the companion star must be towards the 'minimum mass' solution of Muñoz-Darias et al. (2008) in order to get below the observed r-band magnitude limit of 21.4 (Zdziarski et al. 2004; corrected from Shahbaz et al. 2001). Such a star has a low mass transfer rate, yet a large black hole requires a high mass transfer rate

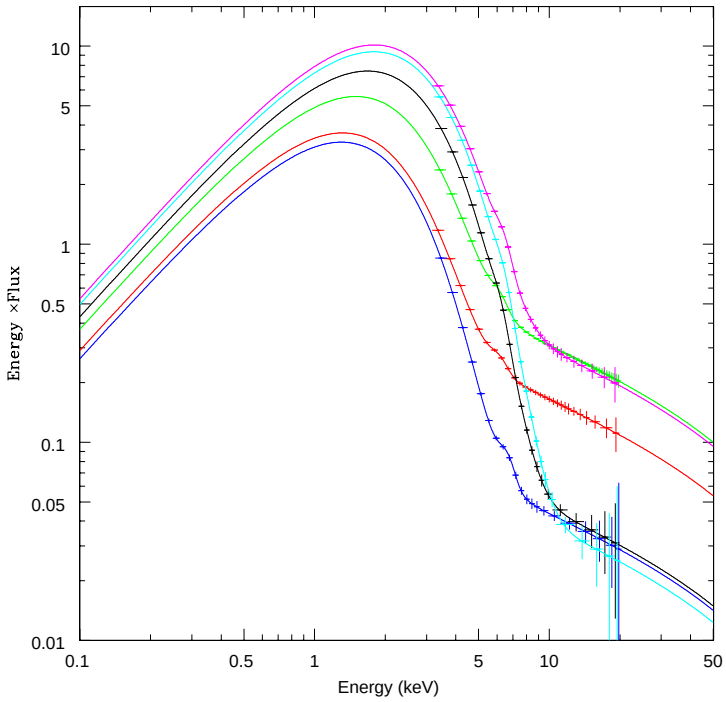

Figure 2.5: A selection of 6 unfolded spectra plotted with a simple diskbb+thCompml model covering a range of luminosities in our data.

to keep the disc close to the borderline between quiescent and transient in order to trigger the multiple outbursts (Muñoz-Darias et al. 2008).

2.6.2 Spin from the iron line fits

There are three independent data sets for GX 339−4 where the line profile has been modelled in detail (Miller et al. 2004; 2006; 2008; 2009; Reis et al. 2008; 2009). We take the most recent determinations, as these use the best current reflection models for black hole binary discs (Ross & Fabian 2007). The low/hard state XMM-Newton MOS data give an inner radius of $r_{in} = 2.04^{+0.07}_{-0.02}$, inclination $i = 20.0^{\circ}_{-1.3}$ with emissivity 3.15 ± 0.15 (Reis et al. 2008). Suzaku observations of an intermediate

state give $r_{in} = 2.39^{+0.24}_{-0.29}$ (i.e. spin of 0.89 ± 0.04), inclination $i = 18^\circ \pm 1^\circ$ (no upper limit given) with emissivity 3.0 ± 0.1 (Miller et al. 2008). Very high state XMM-Newton burst mode PN data give a consistent inner radius and inclination of $r_{in} = 2.02^{+0.02}_{-0.06}$ and $i = 20.0^\circ_{-0.3}$ (no upper limit given). However, this requires a broken power law emissivity which changes from 3 to $7.05^{+0.05}_{-0.2}$ at $r = 6$ (Reis et al. 2008).

However, two of these datasets have been challenged as being affected by instrumental pileup. This clearly affects the line determined from the XMM-Newton MOS low/hard state data, as the simultaneous PN timing mode (which can handle much higher count rates without pileup) data show a much narrower line (Done & Diaz Trigo 2009). Similarly the intermediate state *Suzaku* observation may also be affected by pileup (Yamada et al. 2009). However, the PN burst mode very high state data are not affected by this. These give an equivalent spin of $0.942^{+0.005}_{-0.004}$ for $i = 18^\circ \pm 1^\circ$ and central emissivity of ~ 7.

2.6.3 Comparison of spin from disc fitting and Fe line profile

Thus there is a clear mismatch between the parameters derived from the iron line and those derived from disc spectral fitting in GX 339−4, even after excluding piled up data. The only possible way to make the two consistent are if the inner disc is seen at low inclination, so that it is misaligned from the binary orbit. This would also make it consistent with the low inclination of $18^\circ \pm 1^\circ$ derived from the iron line fits. However, such a large misalignment could only come about from a very asymmetric supernova, but the consequent natal kick is most likely to unbind the black hole from its binary companion, disrupting the system entirely (Fragos et al. 2010). This high spin is also inconsistent with the natal spins predicted from supernova collapse models (Gammie et al. 2004), though these are poorly understood. While accretion does act to spin up the black hole, a low mass companion star of $\sim 1\ M_\odot$ has insufficient

mass to significantly increase the spin of a $\sim 10\ M_{\odot}$ black hole (King & Kolb 1999). We note that none of the spins derived from disc spectral fitting in low mass X-ray binaries are higher than 0.9 except perhaps GRS 1915+105, with $a = 0.98$ claimed by McClintock et al. (2006). However, this depends on details of model assumptions for the Comptonised spectrum, and can be as low as $a_* \sim 0.7$ (Middleton et al. 2006). It seems premature to use contested results from this pathological source to challenge the supernova collapse models.

There are three additional sources where this comparison can be made. These are 4U 1543-475 (iron line: $a_* = 0.3^{+0.2}_{-0.1}$, 22° where BHSPEC gives $a_* = 0.75 - 0.85$) XTE J1550-564 (iron line: $a_* = 0.78 \pm 0.02$, 50°, nearest comparison for BHSPEC is 43° with spin $0.72^{+0.15}_{-0.01}$) and GRO J1655-40 (iron line: $a_* = 0.94 \pm 0.03$ at 70° whereas BHSPEC gives $a_* = 0.65 - 0.75$), with ionised reflection fits in Miller et al. (2009; Table 3) and disc fits in Shafee et al. (2006) and Davis et al. (2006).

This means that 2/4 objects (GX 339−4 in this work and GRO J1655-40: Miller et al. 2009) for which this comparison can be performed give a significantly larger black hole spin from iron line fitting than from the disc spectral method. The remaining 2 objects are marginally consistent, though taking the uncertainties at face value means that formally the spins from 4U 1543-475 are also marginally inconsistent but in the opposite sense (disc fits give higher spin than the iron line).

Which method (if any!) should we trust? The disc spectrum is the dominant spectral component, and the derived disc parameters follow the predicted behaviour for a disc i.e. constant inner radius for changing mass accretion rate (Ebisawa et al. 1993; Kubota et al. 2001; Gierliński & Done 2004). By contrast, the iron line fits model a small feature on the total spectrum (which may have a much more complex form than the typical fit of disc plus power law and its reflection) and often require a highly centrally concentrated line emissivity which is not consistent with the simplest expectations of disc illumination. Thus we argue that the disc spectral fitting model results are more likely to be robust.

2.7 Conclusions

We derive a hard upper limit for the spin of GX 339−4 of $a_* < 0.9$ assuming that the inner disc inclination is the same as that of the binary orbit ($70^\circ < i < 45^\circ$). This is inconsistent with the spin of $0.942^{+0.005}_{-0.004}$ and inclination of $i = 18^\circ \pm 1^\circ$ derived from the (non-piled up) XMM-Newton burst mode very high state data (Reis et al. 2008). This high spin/low inclination derived from the iron line is already uncomfortably extreme compared to the lower spins predicted from supernova collapse models, and the small misalignment angles between black hole spin and binary orbit predicted from binary formation models. While these are both potentially poorly understood, they are independent constraints and the iron line profile in GX 339−4 conflicts with both of them.

The iron line profile itself is in subtle conflict with the X-ray continuum as the reflection smearing parameters require that the illumination pattern is highly centrally concentrated (Miller et al. 2008; Reis et al. 2008). Yet the very high state spectral shape requires that much of the inner disc is covered by optically thick Comptonizing material, making it very difficult to see strong reflection from this material (Done & Kubota 2006).

Thus we argue that the spin/inclination/emissivity derived from the iron line profile are uncomfortably extreme. It seems far more likely to us that the more moderate spin implied by the disc spectral fitting results where the inner disc is more or less aligned with the binary orbit are giving a more robust answer. The inescapable corollary to this is that there are systematic effects affecting spin as derived from the iron line profile that are not yet understood. This is a crucial issue in applying the iron line models with confidence to derive spin in AGNs.

Chapter 3

Paper 2: Modelling the high mass accretion rate spectra of GX 339−4: Black hole spin from reflection?

3.1 Introduction

Black hole spin is currently a subject of intense debate as it is very difficult to measure. Unlike mass, spin only leaves an imprint on the spacetime very close to the event horizon. Nonetheless, there are now two ways to study this. The first uses the temperature and luminosity of the accretion disc formed by material falling into the black hole. These parameters are determined by the combination of the rate at which material is swept through the disc, and how far down the disc can extend close to the black hole. A spinning black hole drags spacetime around with it, so that the accretion disc can extend closer in. This gives higher temperature and luminosity for a given accretion rate, or equivalently in terms of observables, a higher disc temperature for a given luminosity (e.g. Done, Gierliński & Kubota, 2007).

The second method uses the profile of an iron line produced by fluorescence where the X-rays illuminate the accretion disc. The closer the disc extends down

to the black hole, the faster it orbits around, and the stronger the effects of special and general relativity. The large velocity and strong gravity sculpt the line profile, broadening it from a narrow atomic transition in a way which can now be observed (e.g the review by Fabian et al. 2000).

It is obviously important to compare results from these two methods. However, the current level of agreement is not very encouraging. One of the most clearcut cases is GX 339−4, where there are claims of extremely high spin from a very broad iron line in 3 datasets, but where the disc continuum fits strongly prefer lower spin. However, two of the three broad iron line detections have been challenged as being due to instrumental pile-up (Miller et al. 2006 vs. Done & Diaz Trigo 2010 and Miller et al. 2008 vs Yamada et al. 2009). Pile-up occurs where the source is so bright that there is a high probability of two photons hitting either a single pixel within the readout time of that pixel, so that the sum of the energies is assigned to a single photon (energy pile-up) or of two photons hitting adjacent pixels, and being treated as a single photon split between two pixels (double event) with summed energy (pattern pile-up). Both processes distort the spectrum in a way which is not well understood, making detailed spectral fitting (as required for the iron line profile) difficult.

However, the remaining observation of GX 339−4 in which the very broad line is seen was taken in the burst mode of *XMM-Newton*, which is especially designed to handle the highest count rates without pile-up. It does this by reducing the readout time, but at the cost of a dramatic reduction in the detector live time. Only 3% of the available photons are collected, but the spectrum is free from the uncertainties associated with pile-up. However, while this fast timing burst data mode has been available for the *XMM-Newton* EPIC pn detector since the launch, it has only recently been calibrated well enough to give reliable spectra (see e.g. Guainazzi et al. 2010: XMM-SOC-CAL-TN-0083[1]).

[1]http://xmm.vilspa.esa.es/external/xmm_sw_cal/

Here we re-examine all the *XMM-Newton* burst mode spectra of GX 339−4 to assess the level of agreement between the spin derived from disc continuum and from the iron line profile. We find that the black hole spin derived from disc fitting with CCD data is similar to that derived from disc fitting of the higher energy *RXTE* data. However, the data also show that the best current disc contiuum models give 5–10% residuals, as they predict (smeared) atomic absorption features in the disc photosphere which are not present in the data. This is unlikely to be due to any remaining calibration issues in this mode of *XMM-Newton*, or to interstellar absorption, as similar residuals are seen in *Suzaku* data from LMC X-3, which has a very low galactic column (Kubota et al. 2010). Instead it seems more likely that illumination (either self illumination of the inner disc by its own emission or by the hard tail) drives the photosphere towards isothermality. Whatever the underlying cause, the disc dominated spectra are clearly broader than expected from an emissivity weighted sum of blackbody spectra, such as the DISKBB model (Mitsuda et al. 1984).

The shape of the disc spectrum is especially important when it comes to disentangling the iron line profile from the continuum. Fitting a narrow DISKBB shape to the accretion disc emission forces a broad residual into the data. Similarly, the high energy continuum is not a simple power law (Kubota et al. 2001; Zycki, Done & Smith 2001, Gierliński et al. 1999), so fitting such models again forces a broad residual into the spectrum. The iron line shape derived from our fits including a broader disc spectrum and a Comptonised continuum is not extremely broad. It is easily consistent with the lower spin derived from the disc spectral fitting. We caution that the continuum is complex in the soft states, especially the brighter soft states where the disc extends to 6–7 keV, and that how the continuum components are modelled makes a difference to the derived profile of the iron line.

---

calib/documentation.shtml

	Obsid	Date	Exp(s)	State
		EPIC pn		
1	0093562701	2002-08-24 10:30:16	60640	Disc dom.
2	0156760101	2002-09-29 08:56:46	75601	SIMS
3	0410581201	2007-02-19 00:03:25	15048	Disc dom.
4	0410581301	2007-03-05 11:15:56	3200	SIMS
5	0410581701	2007-03-30 15:01:07	8658	Disc dom.
		RXTE PCA		
1	70130-01-01-00	2002-08-24 10:43:07.1	3564	Disc dom.
2	70130-01-02-00	2002-09-29 12:10:17.8	9792	SIMS
3	92085-01-01-00	2007-02-19 17:41:17.7	3504	Disc dom.
4	92085-01-03-03	2007-03-05 13:16:48.6	3200	SIMS
5	92085-02-03-00	2007-03-30 00:57:49	3500	Disc dom.

Table 3.1: Details of the observations. The quoted exposure times are the exposures used in this analysis.

3.2 Observations and data reduction

GX 339−4 reaches a flux of $\sim 10^{-8}$ ergs cm^{-2} s^{-1}, i.e. ∼0.5 Crab (e.g. Dunn et al. 2008). This corresponds to count rates in *XMM-Newton* of $\sim$ 5000 c/s, well above the nominal pile-up limit of the timing mode of 800 c/s. Thus the only option for robust spectral fitting is the burst mode. Table 3.1 gives details of all burst mode observations of GX 339−4, along with details of the *RXTE* dataset closest in time to each observation. Figure 3.1 shows where these spectra fall on the long term *RXTE* PCA lightcurve of this source, with 2 datasets in the 2002/2003 and 3 in the 2007 outbursts.

The pn burst mode data were reduced using the latest version of the *XMM-*

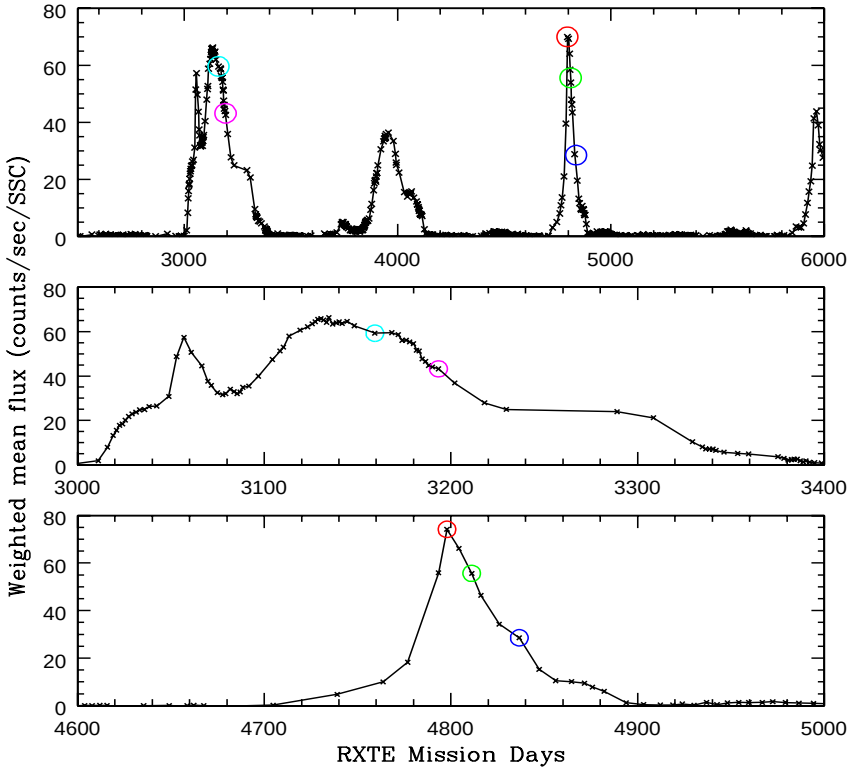

Figure 3.1: The long term *RXTE* ASM light curve of GX 339−4 (top panel) with the 2002/2003 and 2007 outbursts scaled in (middle and bottom panels, respectively). Times corresponding to the *XMM-Newton* burst mode observations are shown by the coloured circles.

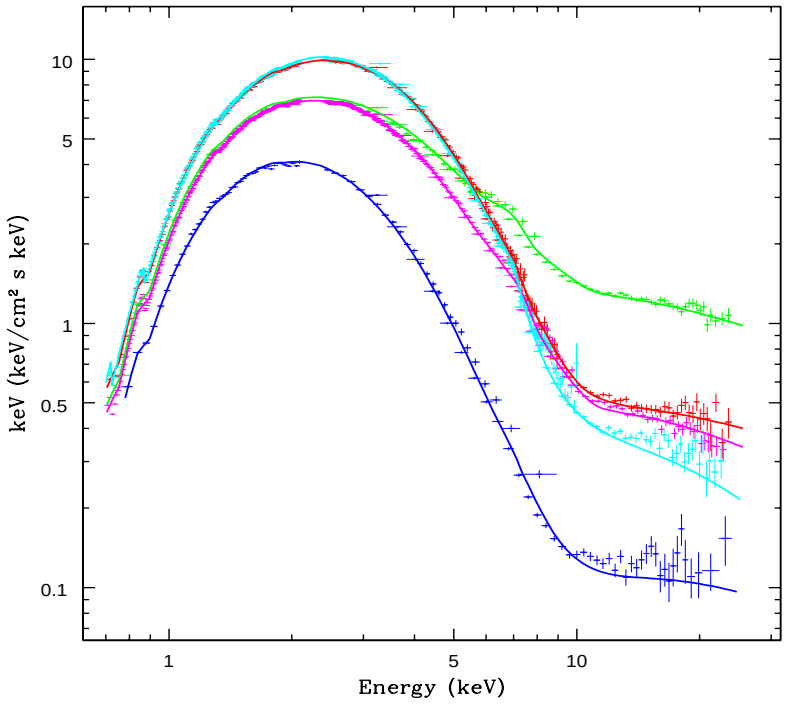

Figure 3.2: The high mass accretion rate spectra of GX 339−4. Colour convention same as in Figure 3.1: Obs 1. in cyan, Obs 2. in magenta, Obs 3. in red, Obs 4. in green and Obs 5. in blue.

Newton Science Analysis System (SAS) v10.0. While the count rates of 1000–5000 c/s ($\sim 0.1 - 0.5$ Crab) are well below the nominal pile-up limit of 60,000 c/s of this mode, an analysis of the Crab nebula showed that sources of this intensity are somewhat affected by pile-up at 140≤RAWY≤180 due to the special readout (Kirsch et al. 2006). We follow their recommendation for robust spectral determination, i.e. extract events in RAWY [1:160]. Slightly different positioning on the chip for the different observations means that we use either RAWX [31:41] or RAWX [31:42]. We only use integer column numbers as the SAS tasks for generating response and ancillary files (RMFGEN and ARFGEN) silently truncate any fractional column num-

ber. We use only single and double events (PATTERN ≤ 4) and ignore bad pixels with #XMMEA_EP and FLAG==0. We correct for rate-dependent charge transfer inefficiency (CTI), using EPFAST, which is included in the latest version of SAS. CTI occurs where electrons are caught in charge traps rather than being read out. This causes small shifts to the energy gain, so is most noticable where the effective area of the instrument changes i.e. at the Si and Au features. The level of residuals at these energies is a measure of success of the CTI correction. Our residuals around the Au edge are at the 2-5% level expected for the current calibration, but this is larger than the 1% systematic error applied to the rest of the spectrum, so we exclude this region from the fit.

Finally the spectra were rebinned using the SAS task SPECGROUP. The number of bins per instrumental energy resolution was set to 3, as recommended for the EPIC pn, to make sure that all the channels are indeed independent for the χ^2 calculations. The high signal-to-noise at low energies and the high oversampling of the *XMM-Newton* response will otherwise lead to the spectral fits being weighted more towards these low energies than the high, and hence artificially low χ^2 values. Each bin was also set to have minimum of 25 counts. Background was not extracted as all regions on the chip are contaminated by the source (Done & Diaz Trigo 2010, see Appendix A).

For each *XMM-Newton* observation we also extract the RXTE data nearest in time. These all have significantly shorter exposure than the *XMM-Newton* datasets. Observations 1, 2 and 4 are all within the corresponding *XMM-Newton* dataset, but 3 and 5 have no overlap in time. However, disc dominated states are known to have rather slow variability, so variability is probably only a potential issue for the observation with the most dominant hard tail (Obs 4). Hence we time filter this *XMM-Newton* dataset to the *RXTE* observation to get truly simultaneous data. We allow there to be a free normalisation between the PCA and *XMM-Newton* data, but tie all the spectral parameters across the two datasets.

	THE MODELS
Model 1a	tbabs×smedge×(diskbb+thcomp+gaussian)
Model 1b	tbabs×smedge×(bhspec+thcomp+gaussian)
Model 2	tbabs×(bhspec+thcomp+kdblur×refxion×(thcomp))
Model 3	tbabs×(simpl(bhspec)+kdblur×refxion×simpl(bhspec))
Model 4	tbabs×(simpl(diskbb+comptt)+kdblur×refxion×simpl(diskbb+comptt))

Table 3.2: The models used in this chapter.

3.3 Spectral analysis overview

We previously analysed all the disc dominated *RXTE* PCA data from GX 339−4 using a multicolour disc and its thermal Comptonisation, together with a Gaussian line and smeared edge to approximately model the expected reflection features ((TBABS×SMEDGE×(DISKBB+THCOMP+GAUSS)): Kolehmainen & Done 2010, Model 1a in Table 3.2). We now test this same model on our composite *RXTE/XMM-Newton* datasets which extends the low energy bandpass to 0.7 keV. We could include the simultaneous *RXTE* HEXTE data in the fit, but the much lower signal to noise at these high energies mean that these points are given very little weight in the spectral fitting. Instead, we include these data after the fit, and ratio the observed flux to the model prediction in the 25–100 keV bandpass to assess how well the model extrapolates to higher energies.

Figure 3.2 shows the derived spectra for the joint pn-PCA datasets. Clearly all of these have a large disc component, but formally only observations 1, 3 and 5 (cyan, red and blue) are disc dominated, while observations 2 and 4 (magenta and green) are soft intermediate states. Observations 1 and 3 have the most dominant disc, while observation 4 has the strongest tail.

Figure 3.3 shows the disc luminosity-temperature plot from Kolehmainen & Done

(2010) (black points) assuming a distance, mass and inclination of 8 kpc, 10 $M_{\odot}$ and 60°, respectively. The crosses show the parameters for the PCA data alone, derived from Model 1a with the absorption fixed at 6×10^{21} cm^{-2} (as in Kolehmainen & Done 2010). All these observations lie on the same $L \propto T^4$ relation as the disc dominated data from Kolehmainen & Done (2010). The solid symbols show how this changes when the pn data are included. Including the lower energy data shifts the best-fit disc parameters to lower temperature/lower luminosity, as predicted from simulations of changing bandpass with more sophisticated disc models (Done & Davis 2008), but the effect is rather small. The disc dominated spectra lie closer to the previous luminosity-temperature relation, while the soft intermediate states are increasingly shifted, so that they have lower temperature than expected for their luminosity (equivalent to a larger disc radius). However, the interpretation of this is complex due to the significant flux carried in the Comptonised tail, and correcting the disc luminosity for these scattered photons can shift these points back towards the constant radius disc luminosity-temperature relation (Kubota & Done 2004; Done & Kubota 2006; Steiner et al. 2010)

3.4 The disc dominated spectra

3.4.1 The brightest disc dominated state: Obs. 3

As the uncertainties in reconstructing the intrinsic disc properties increase when the tail gets stronger, the disc dominated spectra provide the clearest view of the underlying disc physics. We start our analysis with the bright disc dominated state at the peak of the 2007 outburst (Obs 3).

The simplified model used in the previous section (Model 1a in Table 3.2) gives acceptable results for the limited resolution of the PCA detectors over the 3–25 keV bandpass. However, it gives a very poor fit to the joint pn-PCA data ($\chi^2_{\nu} = 745/185$).

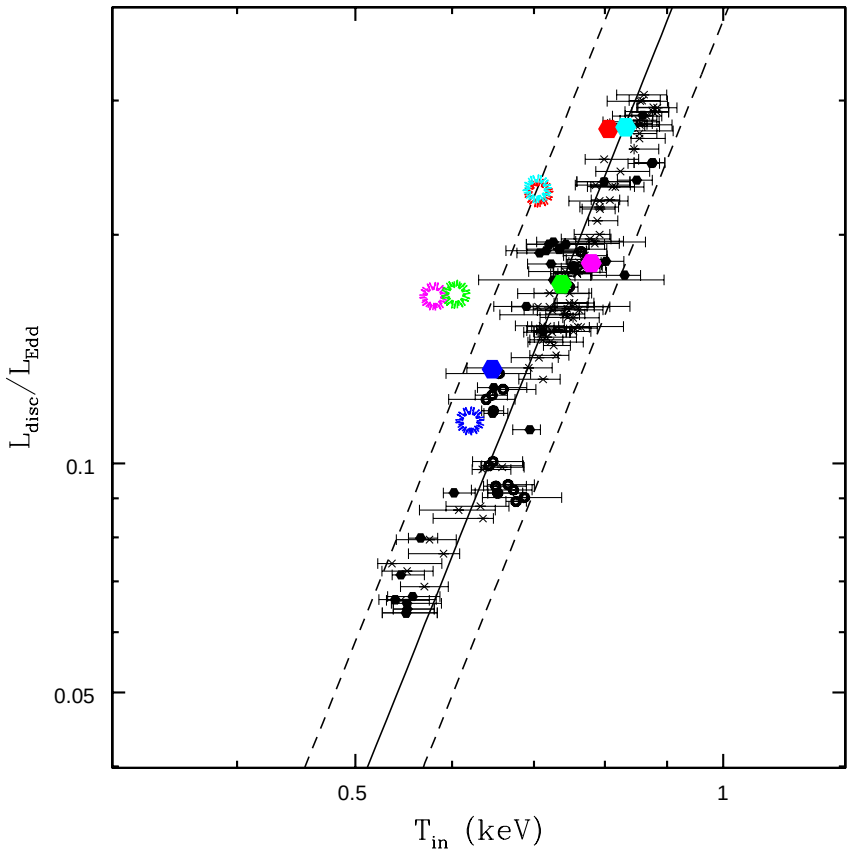

Figure 3.3: The L–T^4 diagram of all previous disc dominated data from the *RXTE* PCA sample of Kolehmainen & Done 2010 (black points) fitted with the simple Model 1a (see Table 3.2). The L–T^4 points fitted with the same model from the PCA data corresponding to each burst mode observation are shown as the coloured solid symbols (same colouring convention as in Fig 3.1), while the L–T^4 points from joint pn-PCA fits are shown as circles. These show a lower colour-temperature correction, as expected, but lie progresively further from the line as the strength of the hard tail increases.

This is to be expected as the true disc is not as simple as a multicolour blackbody. However, replacing DISKBB with a better disc model BHSPEC (Davis et al. 2005, Model 1b; assuming M=10 $M_\odot$, D=8 kpc and an inclination of 60°) makes the fit only moderately better (χ^2_ν = 530/185). Thus it seems more likely that the issue is with the very approximate description of the reflected continuum. We have combined the REFXION tabulated reflection models of Ross & Fabian (2005) with the older PEXRIV models to make a convolution model which can be used with any input continuum (rather than the hardwired power law with exponential cutoff of the REFXION models), and with normalisation given in terms of inclination and solid angle (as for PEXRIV), but with the much more accurate treatment of the ionised reflection of REFXION (see also an older version of this using the Ballantyne et al. 2001 tabulated reflection models in Done & Gierlinski 2006). We convolve this reflected emission with the relativistic smearing Greens functions of Laor (1991), so the total model is TBABS×(BHSPEC+THCOMP+KDBLUR2×REFXION×(THCOMP)) (Model 2). This results in another slight improvement, with χ^2 = 505/186, but the model clearly underpredicts the higher energy HEXTE data, with model 25–100 keV count rate of 2.5, compared to the 4.8±0.3 observed.

One issue with the model above is that the Compton scattering of seed photons from the disc by a corona should also remove disc photons from our line of sight (see the discussion of different geometries in Kubota & Done 2004). The Comptonisation model used here, THCOMP, does not couple the disc and tail together, so instead we replace it with the convolution model SIMPL (Steiner et al. 2009), which removes as many photons from the disc as are scattered up into the tail. This model has the additional advantages that it takes the seed photon shape from the model, rather than assuming blackbody or DISKBB shape as for the THCOMP model. It also assumes a power law tail, better suited to modelling the probably non-thermal emission seen in the high/soft states than thermal Compton scattering (Gierliński et al. 1999).

However, the SIMPL model, as released, does not allow the model to be used to

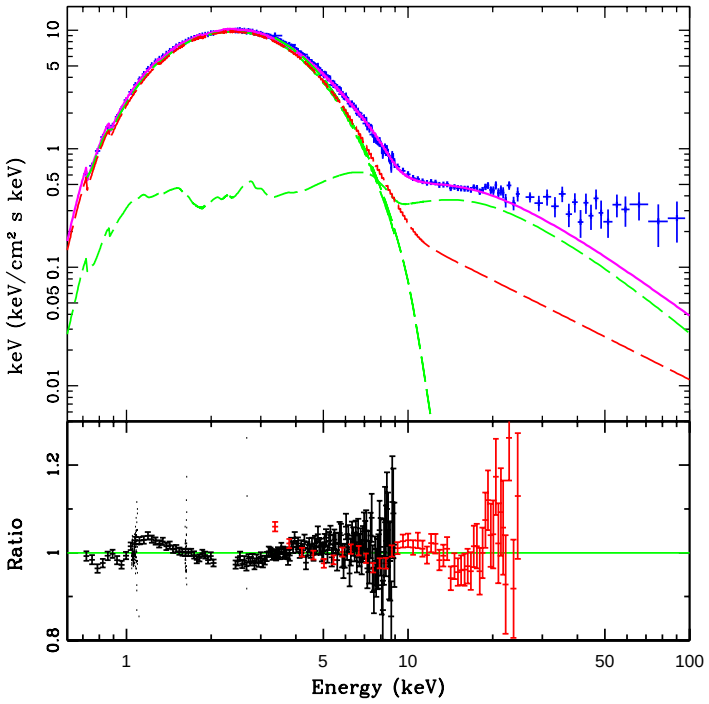

Figure 3.4: The bright disc dominated spectrum (Obs. 3) modelled with Model 3. The top panel shows the data+model, along with the model components (disc+reflection). The model residuals are plotted in the bottom panel.

calculate the tail separately. This is required for the reflection modelling, as only the coronal emission should be reflected. Hence we re-coded the SIMPL model to allow it to do this. However, this model (Model 3 in Table 3.2, with parameters tabulated in Table 3.3) gives only a slightly better $\chi^2 = 426/186$ than Model 2, with very similar parameters, including the mismatch between the extrapolated model and the observed HEXTE flux. Thus the issue is *not* with the description of the Comptonised tail (thermal vs. non-thermal) or with the disc normalisation needing correcting for Compton scattering.

Figure 3.4 shows the deconvolved νF_ν spectrum. Plainly the fit does actually

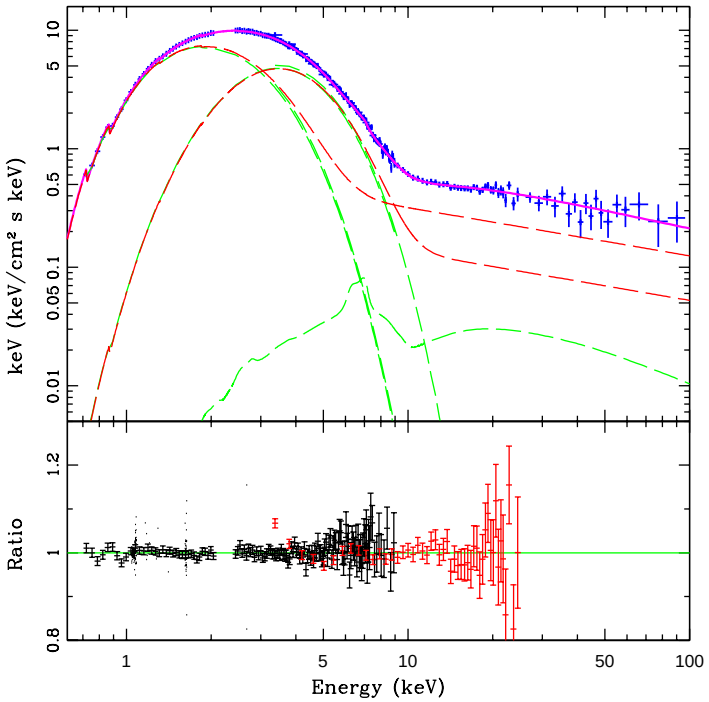

Figure 3.5: Same as Fig 3.4, this time modelled with Model 4.

describe the data quite well below 20 keV, but the Compton tail has a much steeper index than expected, at $\Gamma = 3.19^{+0.09}_{-0.05}$ compared to the typical $\Gamma \sim 2.2$ seen in the high/soft state. To get through the 10–20 keV PCA data then requires a very large reflection fraction $\Omega/2\pi = 6.9^{+0.4}_{-0.6}$ to flatten the spectrum, but reflection rolls over above 30–50 keV so the extrapolation falls well below the level of the HEXTE flux.

Thus the key issue is the derived steep Comptonisation index. One possible reason for this is that the extremely high signal-to-noise in the pn spectra are driving the fit, so that small residuals from the disc model are compensated for by a steep Comptonisation tail. This could indicate that the disc is broader than the BHSPEC model, so we replace this by a phenomenological disc spectrum made from DISKBB+COMPTT (Model 4 in Table 3.2). This gives a much better fit to the data $\chi^2_\nu = 210/186$, as

seen by the lower level of residuals below 1.5 keV (Figure 3.5). There are still two features below 1 keV, possibly Ne III and Ne II lines from the interstellar medium (Miller et al. 2004b), but no big residuals at iron.

At first sight it seems likely that the better fit with the phenomenological disc spectrum could simply be compensating for remaining calibration uncertainties in the instrument response of this mode. Figure 3.6 shows a comparison of the phenomenological DISKBB+COMPTT continuum with the BHSPEC continuum. Clearly the biggest difference is that BHSPEC predicts absorption features from ionised oxygen and iron L in the disc photosphere from 0.7–1.5 keV. These should be smeared by relativistic effects, resulting in the broad dip predicted by BHSPEC rather than sharp edges.The phenomenological model does not have these features, but is as broad as the BHSPEC continuum. This pattern of residuals is very similar to that obtained from a recent *Suzaku* spectrum of LMC X-3 in a disc dominated state (Kubota et al. 2010). These are seen even more unambiguously in LMC X-3 due to its much smaller galactic column density along the line of sight (0.038×10^{22} cm^{-2} compared to $\sim 0.52 \times 10^{22}$ cm^{-2} for GX 339−4). The different instrument (*Suzaku*) also means that the issue is not likely to be simply the *XMM-Newton* burst mode calibration.

However, the shape of the derived disc continuum is difficult to explain. It is as broad as the total continuum predicted by the BHSPEC models, but these models produce the broad continuum partly by the changing colour-temperature correction associated with the atomic features yet the atomic features are not observed. Relativistic smearing of a single colour-temperature corrected disc spectrum (as in the KERRBB disc model: Li et al. 2005) is not broad enough to explain the data (green line in Fig 3.6). For comparison, we also show the best fit DISKBB model, which is plainly far too narrow (Fig 3.6).

Thus it seems most likely that even the best current disc models do not describe the observed disc spectra at the 5-10% level, so we also use the best fit phenomenological description (Model 4) in all the following analysis.

3.4.2 The other disc dominated states: Obs. 1 & 5

We fit the two other disc dominated states with Models 3 and 4 described above, with best-fit parameters given in Tables 3.3 and 3.4, respectively. We see the same pattern as before, namely that the best current disc models are not quite the right shape to match with the high signal-to-noise EPIC pn data, so they drag the Comptonisation index to higher values to compensate, which in turn requires more reflection to flatten the spectrum in the 10–20 keV bandpass so that it can match the observed PCA data. This then fails to fit the HEXTE points. By contrast, the phenomenological DISKBB+COMPTT disc continuum fits the data much better, gives more reasonable values for the Comptonisation index and amount of reflection, and extrapolates to the HEXTE band.

Figures 3.4 – 3.8 show the deconvolved spectra for both model fits to observations 1 and 5. Unlike the more luminous spectrum discussed in the previous section, there is now a clear mismatch above 4 keV between the pn and PCA spectra. This is most likely due to the lack of background subtraction in the burst mode data, which is now beginning to become an issue at high energies for this lower luminosity spectrum. We discuss this in more detail in Appendix A.

The remaining disc dominated spectrum, Obs. 1, is very similar to the Obs. 3 so we do not show the deconvolved spectra, but give details of the fits in Tables 3.3 and 3.4. Again, the main difference between Model 3 and 5 is that the BHSPEC models predict smeared absorption features which are not seen in the best fit DISKBB+COMPTT models.

3.5 The soft intermediate state spectra (SIMS)

A significant advantage to using the SIMPL model is that it also allows us to fit spectra with strong tails in addition to the thermal dominated ones. We now use the same

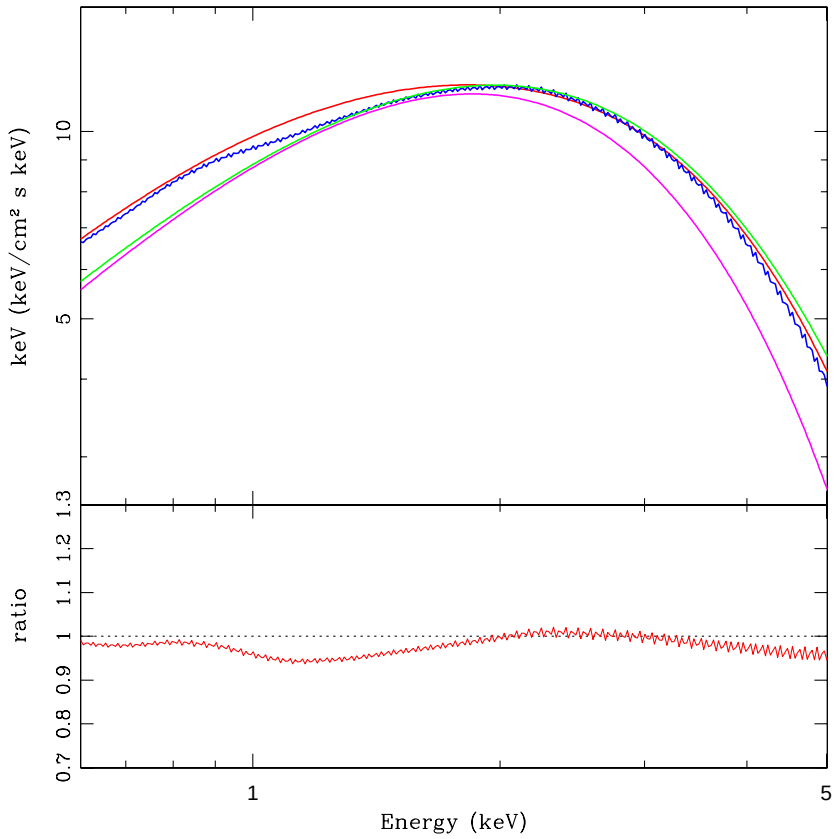

Figure 3.6: Comparison of different disc continuum models with Obs 3. DISKBB+COMPTT is plotted in red, BHSPEC in blue, KERRBB in green and DISKBB in magenta. The bottom panel shows the ratio of BHSPEC to DISKBB+COMPTT. The phenomenological DISKBB+COMPTT continuum is clearly most agreeable with the data, and hence is chosen as the disc model in the following analysis.

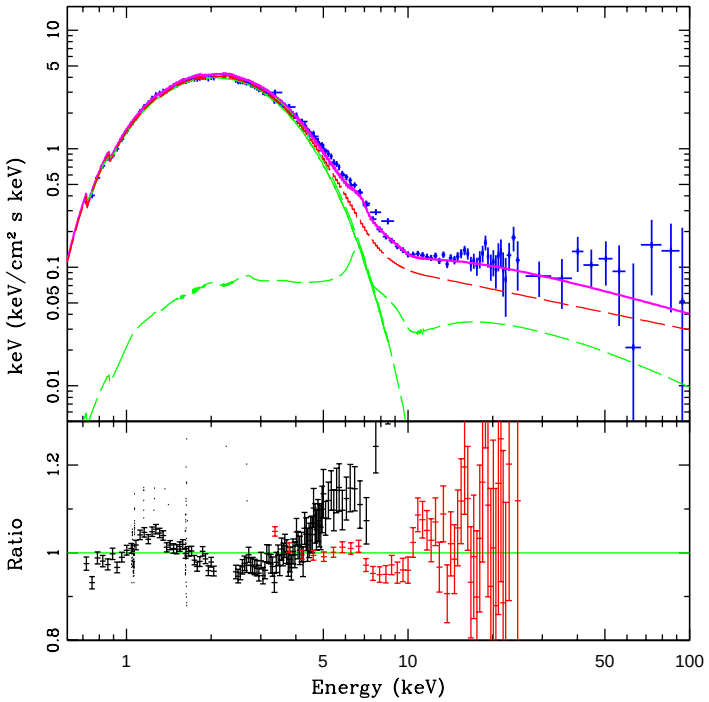

Figure 3.7: The faintest disc dominated spectrum (Obs. 5) modelled with Model 3. The top panel shows the data+model, along with the model components (disc+reflection). The model residuals are plotted in the bottom panel.

models (3 and 4) to go through the SIMS spectra in order of the strength of the tail.

3.5.1 The 2002/2003 outburst: Obs. 2

The tail carries roughly 25% of the total luminosity, and Figure 3.3 shows that it is slightly steeper than the tail seen in the disc dominated spectra. Our best-fit for Model 3 gives a very poor χ^2 of 798/199 d.o.f., while Model 4 gives a better fit with χ^2_ν=451/196. These are shown in Figures 3.10 and 3.11. Both have clear residuals above 6 keV in the pn but not the PCA. The residuals in Model 3 look like there may be an absorption line at $\sim$ 7 keV, but this feature disappears with the different

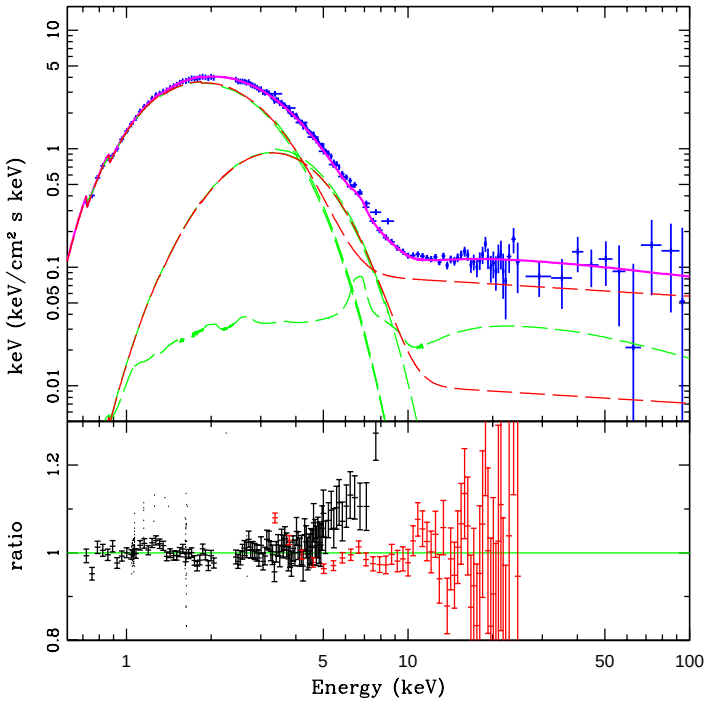

Figure 3.8: Same as Fig 3.7, now modelled with Model 4.

continuum of Model 4 and instead there is a line-like residual at ~ 8 keV. This could be due to the copper line in the pn, but no such line is seen in the residual background in Fig 3.15. However, even Model 4 struggles to fit the shape of the spectrum well, though some of this could be that the disc ionisation parameter hits its upper limit ($\log\xi = 4.00_{-0.04}$), i.e. the model does not extend to high enough ionisation to fit the data.

These data were previously analysed (though with older versions of the SAS which did not include CTI corrections) by e.g. Miller et al. (2004;2006;2008;2009) and Reis et al. (2008). These studies observed a very skewed iron line at ∼6.4 keV, indicating an almost maximally spinning black hole. This is in sharp contrast to the results from either Model 3 or 4 in our spectral fits, where the derived inner radius is quite

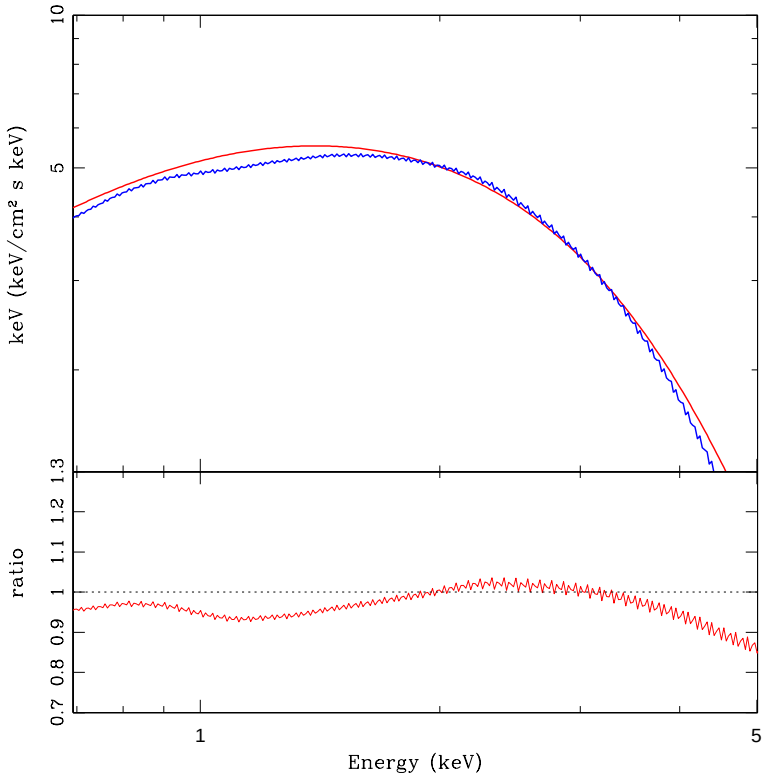

Figure 3.9: Same as Fig 3.6 for Obs. 5, now showing the phenomenological model DISKBB+COMPTT in red and the best theoretical model BHSPEC in blue. The bottom panel shows the ratio of BHSPEC to DISKBB+COMPTT.

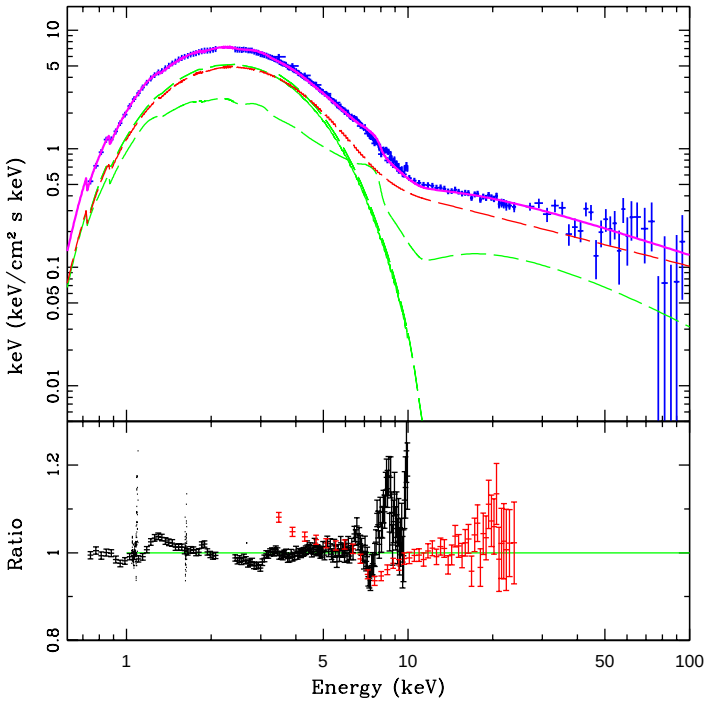

Figure 3.10: The 2002/2003 SIMS spectrum (Obs. 2) modelled with Model 3. The top panel shows the data+model, along with the model components. The model residuals are plotted in the bottom panel.

large at $R_{in} = 34^{+10}_{-17} R_g$. We return to this point in Section 3.6.

3.5.2 The 2007 outburst: Obs. 4

Figure 3.2 shows that the strongest tail is in the 2007 outburst, in observation 4 (green). Results from fits with Models 3 and 4 are again shown in Tables 3.3 and 3.4, and the spectra shown in Figures 3.12 and 3.13.

Model 3 gives an unacceptable χ^2=968/186 d.o.f. The predicted continuum falls substantially below the HEXTE points and the derived column is lower than for the other datasets, at $N_H = 5.0^{+0.04}_{-0.02} \times 10^{21}$ cm^{-2}. Model 4, on the other hand, gives a

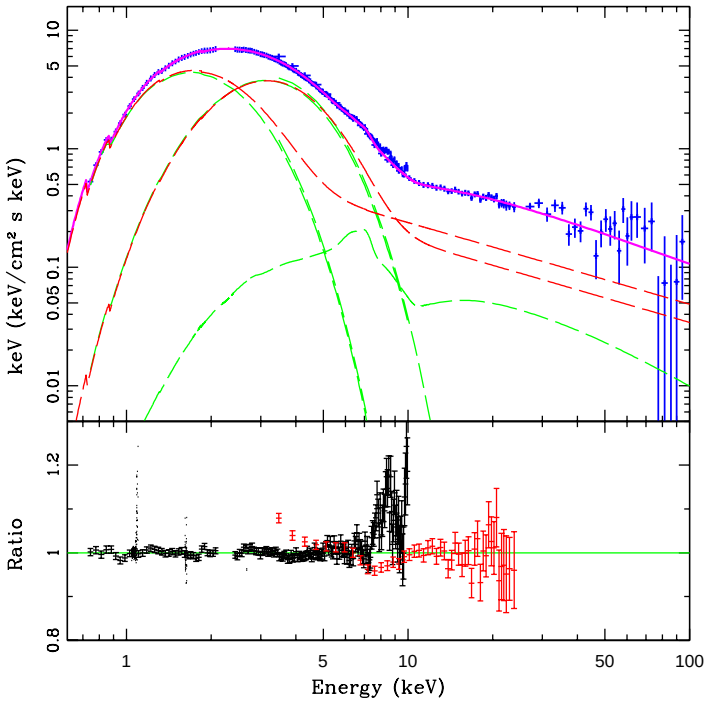

Figure 3.11: Same as Fig 3.10, modelled with Model 4.

best-fit χ^2=297/183 d.o.f (though there is still a mismatch in residuals between the pn and the PCA above 7 keV), with hydrogen column of $N_H = 5.45 \times 10^{21}$ cm^{-2}, more consistent with the other datasets. The reflected continuum has a moderate solid angle of $\Omega/2\pi = 0.63^{+0.16}_{-0.10}$ and again, the smearing is not at all extreme, with $R_{in} = 42^{+18}_{-30} R_g$. This reflection is highly ionised, but is within the range of tabulated models at $\log \xi = 3.9 \pm 0.1$. Since these data are brighter, it seems unlikely that the ionisation parameter is truly higher in the previous soft intermediate state above (Obs. 2). Instead, this probably indicates that the previous data are more complex than the model fit.

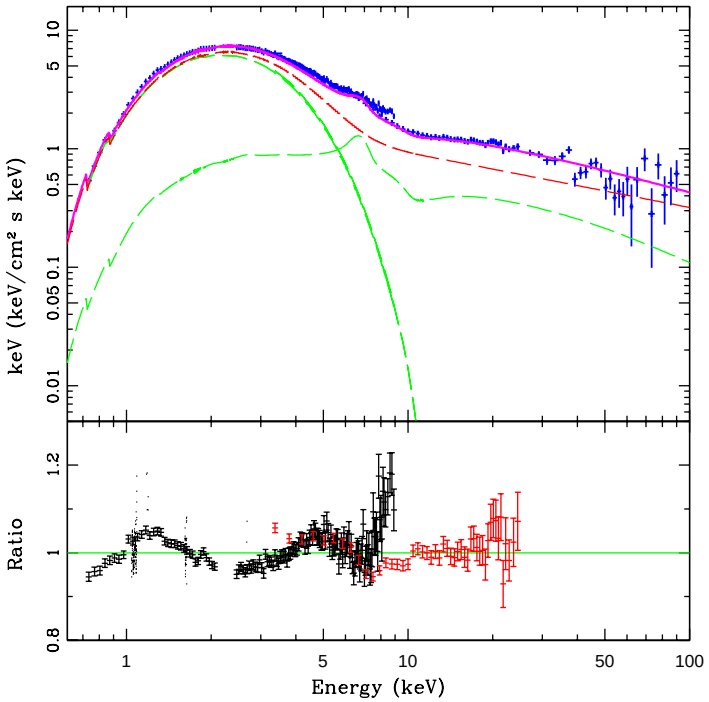

Figure 3.12: The 2007 SIMS spectrum (Obs 4.) modelled with Model 3. The top panel shows the data+model, along with the model components. The model residuals are plotted in the bottom panel.

3.6 Black hole spin

3.6.1 Disc continuum fits: BHSPEC

The BHSPEC model fits directly for black hole spin from the dominant disc component for a given mass, distance and inclination. These system parameters are quite poorly known for GX 339−4 (see e.g. Kolehmainen & Done 2010), but fixing these at reasonable values of $10M_{\odot}$, 8 kpc and 60°, respectively, gives derived spin values which are low to moderate ($a_* = 0.1 - 0.5$). This is as expected from the previous fits to the *RXTE* PCA data (Kolehmainen & Done 2010). However, the derived

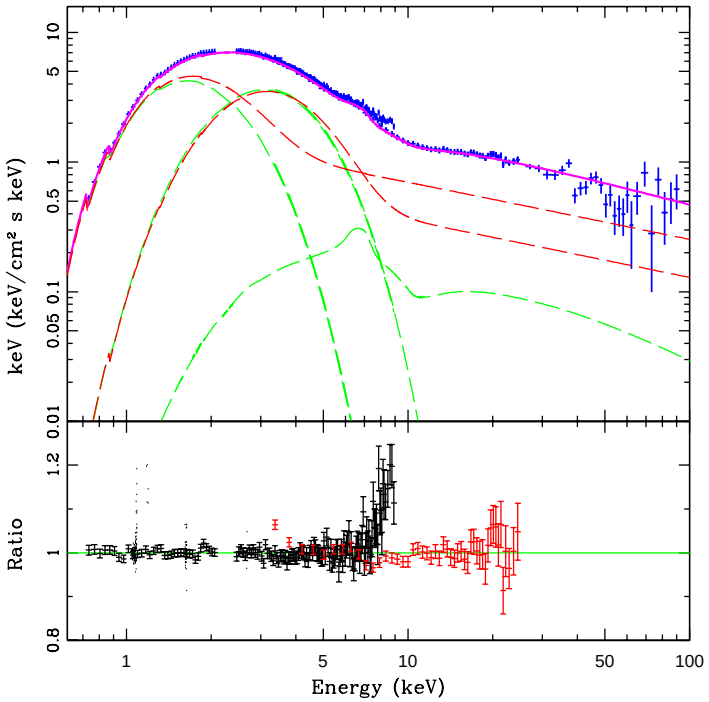

Figure 3.13: Same as Fig 3.12, modelled with Model 4.

spin is not constant, even when restricted to the disc dominated spectra (Table 3.3) due to the mismatch between the broad absorption features from oxygen and iron L predicted by BHSPEC and the data (Figs 3.6 and 3.10). The excellent statistics of the *XMM-Newton* data means that these 5–10% residuals drive the Comptonised continuum to a much steeper index to compensate for this lack of flux at low energies. This level of mismatch between the data and model is enough to distort the entire fit.

These fits (Table 3.3) also give an estimate for black hole spin from the iron line profiles. However, since the fits are so distorted, these are clearly not reliable.

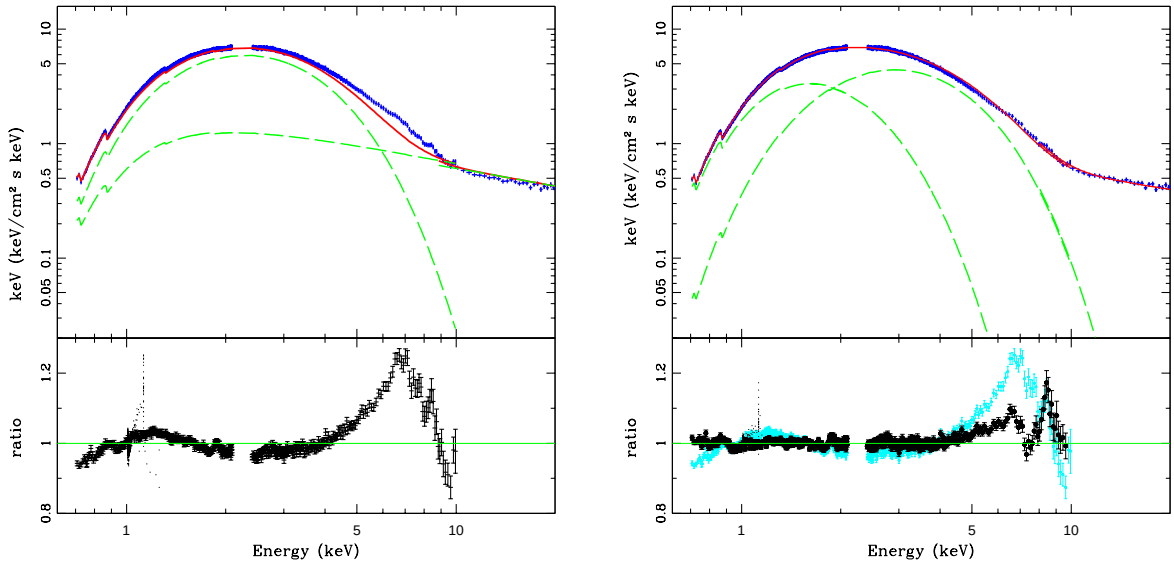

Figure 3.14: The 2002/2003 SIMS observation (Obs. 2) fitted with different set of models to illustrate the dependency of emission line residuals to the chosen continuum model. The continuum is fitted by excluding 4–7 keV. Only EPIC pn residuals are plotted for clarity. *a) Left panel*: DISKBB+POWERLAW. The residuals show a broad emission line feature at ∼6.5 keV. *b) Right panel*: The same spectrum modelled with Model 4. Residuals show narrow line features (black) and as a comparison the residuals from the *left panel* (cyan).

3.6.2 Iron line

The disc continuum is much better modelled using the phenomenological DISKBB+COMPTT description. With this, the amount of smearing of the reflected emission should be indicative of the inner radius of the disc. However, none of our spectral fits give a line which is so broad as to require that the disc extends down to the last stable orbit around even a Schwarzschild black hole. This is in sharp contrast to the claim of Miller et al. 2004 and Reis et al. 2008 for the less extreme soft intermediate state spectrum (Obs. 2), that the iron line is so broad as to require that the black hole in GX 339−4 has high spin, of a_*=0.935. This value is also in conflict with the upper limit for the spin of $a_* \leq 0.9$ in GX 339−4 (Kolehmainen & Done, 2010). We repeat their analysis on this specific dataset (Obs. 2, combined with *RXTE* PCA data), and fit the spectrum, excluding the 4–7 keV (i.e. Fe line) region, with a simple diskbb+power law. We then plot residuals including the Fe line bandpass. Our residuals indeed show a very similar line profile to their results, with an extremely broad red wing to the iron line (Figure 3.14a). Furthermore, we also add a relativistic emission line model (LAOR; Laor 1991) to describe the Fe line more physically. Again we see similar results in terms of a very small disc inner radius, low inclination and a very centrally peaked emissivity.

However, modelling complex spectral curvature such as this is a delicate task. Fig 3.2 shows that the iron line is in an area where the curvature changes from being dominated by the disc to being dominated by the tail. The 'iron line' residual will then be strongly affected by a small change in the continuum model. We show this explicitly by fitting our best continuum model (DISKBB+COMPTT for the disc, convolved with SIMPL for the tail) to the data, again excluding the Fe line region. Figure 3.14b then shows the same as Fig 3.14a but with the continuum modelled using Model 4. We overplot the previous residuals for direct comparison and the change in shape of the derived line profile is immediately apparent.

The line profile derived by this method is clearly very sensitive to a change in underlying continuum shape. The analysis of the disc dominated spectra in Section 3.4 shows that the disc continuum is substantially broader than a DISKBB due mainly to relativistic smearing of the disc continuum and radiative transfer through the disc photosphere. Fitting a DISKBB continuum then forces a broad residual into the data from the poor match to the disc continuum. However, this broad residual on the tail of the disc spectrum is in the same energy band as the expected red wing of the iron line. We caution that the derived iron line shape depends on the assumed continuum, and that this is especially important where the continuum curvature changes rapidly under the iron line. This is the case for all the bright disc dominated and soft intermediate spectra considered here.

Table **??** shows that with our best fit model the line is not extremely smeared in these data (consistent with Fig 3.14b), with $R_{in} = 34^{+10}_{-17} R_g$. This does not mean that we infer the disc to be truncated. Quite the contrary, the unfolded spectrum has a clear disc shape below ∼6 keV and the disc contributes to ∼75% of the total luminosity. Our fit also requires that the reflecting material is highly ionised, as expected from the high effective temperature of the disc. It seems more likely that the inner disc is so highly ionised that iron is completely stripped, so no longer contributes to the atomic features which are the best tracer of the reflecting material. We also caution that while this model is our best fit, our iron line parameters will also depend on our assumed continuum form. While our reflection is derived from the best currently available models (Ross & Fabian 2005), these are calculated for the lower density and temperatures of AGN discs. Newer reflection models including the effect of collisional ionisation should instead be used (Ross & Fabian 2007), but we caution that these alone will not solve the sensitivity of the iron line profile to the underlying continuum shape.

DISC:BHSPEC			COMPTONISATION + REFLECTION					
Obsid	$N_H(\times 10^{21})$	$L/L_{\rm Edd}$	a_*	Γ	R_{in} (R_g)	logξ	$f = \Omega/2\pi$	χ^2/ d.o.f
0093562701	$5.31^{+0.01}_{-0.01}$	0.26 ± 0.01	0.20 ± 0.003	$3.21^{+0.01}_{-0.03}$	26^{+7}_{-6}	$3.30^{+0.01}_{-0.04}$	$5.70^{+0.65}_{-0.15}$	721/198
0156760101	$5.58^{+0.10}_{-0.05}$	0.14 ± 0.01	0.51 ± 0.01	$2.80^{+0.02}_{-0.02}$	16^{+2}_{-2}	$3.36^{+0.02}_{-0.02}$	$0.66^{+0.04}_{-0.04}$	798/199
0410581201	$5.50^{+0.03}_{-0.05}$	0.15 ± 0.01	0.54 ± 0.01	$3.19^{+0.09}_{-0.05}$	33^{+31}_{-9}	$3.09^{+0.01}_{-0.05}$	$6.94^{+0.42}_{-0.55}$	426/186
0410581301	$5.00^{+0.04}_{-0.02}$	0.17 ± 0.01	0.18 ± 0.01	$2.51^{+0.01}_{-0.05}$	32^{+12}_{-7}	$4.00_{-0.31}$	$0.72^{+0.04}_{-0.09}$	968/186
0410581701	$5.25^{+0.03}_{-0.03}$	0.12 ± 0.01	$0.21^{+0.02}_{-0.01}$	$2.35^{+0.01}_{-0.04}$	33^{+11}_{-8}	$3.31^{+0.02}_{-0.01}$	$3.34^{+3.60}_{-2.89}$	519/178

Table 3.3: The best-fit parameter values of Model 3. The errors quoted are shown for illustrative purposes only, in summary of the freedom of fit.

	DISC:DISKBB+COMPTT			COMPTONISATION + REFLECTION					
Obsid	$N_H(\times 10^{21})$	T_{in} (keV)	kT_e	τ	Γ	R_{in} (R_g)	logξ	$f = \Omega/2\pi$	χ^2/ d.o.f
0093562701	$5.30^{+0.01}_{-0.03}$	$0.57^{+0.01}_{-0.002}$	$0.76^{+0.002}_{-0.003}$	60^{+5}_{-24}	$2.45^{+0.06}_{-0.02}$	101^{+298}_{-37}	$3.88^{+0.10}_{-0.11}$	$0.77^{+0.04}_{-0.11}$	276/195
0156760101	$5.35^{+0.01}_{-0.02}$	$0.49^{+0.01}_{-0.002}$	0.74 ± 0.01	33^{+1}_{-3}	$2.69^{+0.03}_{-0.01}$	34^{+10}_{-17}	$4.00_{-0.04}$	$0.76^{+0.04}_{-0.03}$	451/196
0410581201	$5.25^{+0.03}_{-0.04}$	0.59 ± 0.01	0.77 ± 0.01	120^{+80}_{-50}	$2.41^{+0.17}_{-0.10}$	64^{+99}_{-30}	$3.13^{+0.30}_{-0.18}$	$0.46^{+0.10}_{-0.13}$	210/183
0410581301	$5.45^{+0.02}_{-0.07}$	0.46 ± 0.01	0.71 ± 0.01	30^{+3}_{-3}	$2.44^{+0.02}_{-0.03}$	42^{+18}_{-30}	$3.90^{+0.10}_{-0.10}$	$0.63^{+0.16}_{-0.10}$	297/183
0410581701	$4.87^{+0.04}_{-0.05}$	0.58 ± 0.01	0.73 ± 0.01	65^{+117}_{-65}	$2.15^{+0.18}_{-0.05}$	235^{+164}_{-136}	$3.09^{+0.17}_{-0.12}$	$0.62^{+0.10}_{-0.17}$	323/175

Table 3.4: The best-fit parameter values of Model 4. The errors quoted are shown for illustrative purposes only, in summary of the freedom of fit.

3.7 Discussion and conclusions

The new calibration of the XMM-Newton EPIC pn burst mode allows detailed spectral fitting of bright black hole binaries. We use these data together with (mostly) simultaneous RXTE data to explore the shape of the disc dominated and soft intermediate state 0.7–200 keV spectra from GX 339−4. This is an important object to understand as there are conflicting measures of the black hole spin in this object, with disc continuum fitting of disc dominated states from RXTE showing an upper limit of $a_* < 0.9$ (Kolehmainen & Done 2010) while the iron line profile in an XMM-Newton dataset from a soft intermediate state gives $a_* = 0.935$ (Miller et al. 2004; Reis et al. 2008).

We find that while the disc dominated states are well fitted with the simple DISKBB model (together with a tail to high energies and its reflection) in the PCA, the lower energy extent of the CCD bandpass shows that this is not a good representation of the disc emission. This is as expected, as the disc continuum should also be smeared by relativistic effects, making it substantially broader. We fit the best current disc models to the data instead. These include full radiative transfer through the disc photosphere as well as relativistic smearing (BHSPEC: Davis et al. 2005). However, these are not a good match to the data either, as although they are broader, they predict smeared atomic absorption features at oxygen/iron L which are not present in the data. This mismatch is also seen in *Suzaku* data from LMC X-3 (Kubota et al. 2010), making it unlikely to be a residual calibration feature of *XMM-Newton*. Instead, it could be due to irradiation of the photosphere by the weak high energy tail.

Whatever its origin, the disc dominated spectra clearly show that the observed disc spectrum can only be currently well matched by phenomenological models. We use the same phenomenological description to fit the disc component in the soft intermediate state. This broader disc spectrum has a profound effect on the derived

iron line profile, as the line energy is close to where disc and tail components have equal flux. A small change in the disc spectrum then makes a large change in the residual flux at the iron line energy. We find that we cannot constrain black hole spin in these data with our continuum model as the line profile (which is already smeared by Compton scattering in the highly ionised reflector) is not strongly relativistically smeared, so arises predominantly from radii which are rather larger than even the last stable orbit around a Schwarszchild black hole. This probably indicates that the inner disc is so highly ionised that iron is completely stripped and hence does not produce any characteristic atomic features.

We caution that using simple continuum models for complex spectra will result in broad residuals in the data simply from deficiencies in the continuum modelling rather than giving a robust, model independent way to see the iron line profile. All bright black hole binary spectra are complex, as the disc temperature is hot enough that the iron line region is on the cross-over between the disc and tail. Only the very dimmest disc dominated spectra, where the disc peaks below ~ 1 keV, and the low/hard state have an iron line region where the continuum is mostly dominated by the tail. However, we also caution that the tail can also have complex (though more subtle) curvature which may also affect the line residuals.

3.8 Appendix A: Burst mode background

Background subtraction of bright sources in burst (and timing) modes is very challenging. The bright source contaminates the whole CCD chip, and hence background was not subtracted in the reduction phase of this analysis. To illustrate this effect, we extract a 'background' spectrum for all of our observations. The extraction region was selected as a strip of RAWX [3:10] and RAWY [1:160], near the edge of the chip, away from the source itself.

Figure 3.15 (top panel) shows the source spectrum (red), plotted with the background (blue) in detector counts. The shape of the background clearly mimics that of the source, indicating that much of the extracted 'background' is in fact contaminated by the source (see also Done & Diaz Trigo 2010 for similar issues in EPIC pn timing mode, and Guainazzi et al. 2010a). We attempt to constrain the true background by subtracting a scaled version of the source spectrum from the extracted background. We set the scale by assuming that the true background is negligible in the 1–2 keV bandpass. The remaining background is still a slight overestimate of the true background as high energy photons are preferentially scattered into the wings of the point spread function, so the spectrum at large off-axis angles will be slightly harder than the on-axis source spectrum. We plot the resulting background estimate as unfolded (νF_ν) spectra in the lower panel of Fig. 3.15.

The background above 5 keV from singles in the pn full frame mode is typically at a level of 0.1 counts/s/keV, with a strong copper line superimposed (Freyberg et al. 2006: XMM-SOC-CAL-TN-0068[1]). Adding the doubles (burst mode loses one spatial dimension, so cannot distinguish between singles and doubles in the compressed direction) would increase this by a factor ~ 2. This is roughly the level seen at 10 keV in all the spectra (upper panel) except for the one with the strongest tail (Obs. 4). The lower panel shows the source subtracted νF_ν looks similar to that expected from the background, with a strong copper line at 8 keV

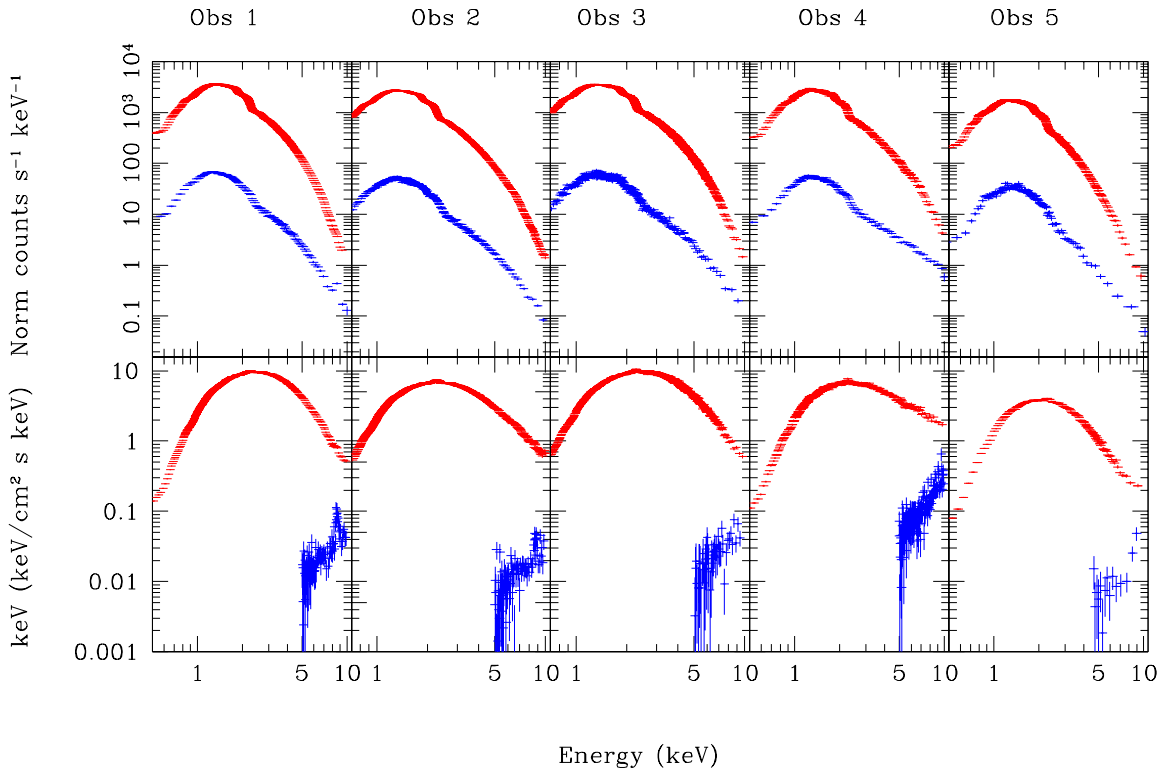

Figure 3.15: Background analysis for the EPIC pn burst mode. *Top panel*: The source spectrum (in red), plotted with the extracted background (blue) in detector counts. The shape of the background plainly follows the shape of the source, indicating that much of the 'background' is in fact contaminated by the source. *Bottom panel*: The background spectrum (in blue) corrected with the source spectrum. Observations 1 and 2 show the clearest copper lines at ∼8 keV, while the 'background' level in observation 4 is clearly strongest of the sample.

in all the disc dominated spectra. However, the 'background' level is progressively larger, swamping the line, in the spectra with stronger tails. This probably indicates that there is residual contamination from the source, and this contamination gets stronger for stronger hard spectra.

Thus the residual background in the faintest disc dominated spectrum is probably closest to the 'true' background for singles plus doubles in burst mode. This is 20% of the source flux at 8–10 keV. The bright disc dominated spectra are a factor $\sim$ 3–4 brighter at 10 keV (see Fig 3.2), so a similar background here would give a 5% excess at high energies in the pn. The residuals to the best fit model appear to be slightly larger than this (Fig 3.5) which may indicate remaining cross-calibration uncertainties between the pn and PCA (Guainazzi et al. 2010, Weisskopf et al. 2010).

The clear conclusion is that the background in burst mode is not necessarily negligible, especially for very soft spectra. There is no way to estimate this reliably from the data, so offset pointings are required.

Chapter 4

Paper 3: The Low/hard state of black hole binaries

4.1 Introduction

The current paradigm for the structure of the accretion flow in black hole binaries (hereafter BHB) at low luminosities is that the cool, optically thick, geometrically thin standard accretion disc is progressively replaced in the inner regions by a hot, optically thin, geometrically thick flow as the mass accretion rate decreases (low/hard state, Esin et al. 1997). This model has gained widespread acceptance by its ability to provide a framework in which to interpret large amounts of apparently unrelated observational data, predominantly revealed by the multiple *RXTE* observations of these systems. At the lowest luminosities, the large disc truncation radius means that the disc emission is cool and dim. Few seed photons from the disc illuminate the flow, so the Comptonised spectra are hard. Decreasing the disc truncation radius leads to a stronger disc component, and to a greater overlap of the flow with the disc. This gives more seed photons to Compton cool the flow, giving softer Compton spectra. The decreasing radius also means that any frequencies set by this radius will increase, giving a qualitative description of the increasing characteristic frequencies seen in the power spectra and their tight correlation with the energy spectra. The flow is completely replaced by the disc when the disc reaches its minimum radius of the last stable circular orbit (high/soft state), giving a physical mechanism for the

marked hard-to-soft transition seen in black hole binaries. Even the jet behaviour can be tied into this picture, as a large scale height flow is probably required for jet formation, so the collapse of the inner flow as the disc reaches its minimum radius triggers a similar collapse of the radio emission (see e.g. the reviews by Remillard & McClintock 2006; Done, Gierliński & Kubota 2007, hereafter DGK07 and Belloni et al. 2010).

Despite these evident successes, these models remain controversial due to claims that the disc extends down to the last stable orbit in the low/hard state. There are two observational signatures of this. Firstly, reflection of the Comptonised emission from the disc is smeared by a combination of special and general relativistic effects, and the extent of this broadening is determined by the inner disc radius (e.g. the review by Fabian et al. 2000). Secondly, the luminosity and temperature of the direct continuum from the disc itself can be used to evaluate the emitting area, and hence the inner disc radius. Both these require CCD data rather than the more numerous proportional counter *RXTE* datasets (lower energy bandpass for the low temperature disc emission, and higher spectral resolution for the iron line profile). A recent review of low/hard state CCD spectra from BHB by Reis et al. (2010, hereafter R10) claimed that both these signatures were routinely seen at a level which generally excluded a truncated disc.

These claims are themselves controversial, and have been challenged in the literature. The most convincing broad iron line profile in R10 is from a bright low/hard state of GX 339−4. This profile is derived from data where instrumental pileup is an issue (Miller et al. 2006; Done & Diaz Trigo 2010). Simultaneous data from another instrument which does not suffer from pileup clearly shows a much narrower line (Done & Diaz Trigo 2010). However, simulations of pileup do not produce an artificially broad line (Miller et al. 2010), but our understanding of pileup for such an extreme count rate (200× over the limit for the instrument mode used) is probably not complete (see also counterexamples in the data compilations of Ng et al. 2010;

Yamada et al. 2009).

The intrinsic disc emission has a different set of issues. Firstly it can be much weaker than the Compton continuum even in the CCD X-ray bandpass, so its luminosity and temperature depend on how the continuum is modelled (e.g. the difference in inner radius in Rykoff et al. (2007) from using Comptonised emission compared to a power law). This is unlike the situation in the high/soft state, where the disc dominates and the high energy continuum model has little effect on the results (e.g. Kubota & Done 2004). Even having modelled the disc emission, its luminosity and temperature need not be simply due to gravitational energy release as in the high/soft state. X-ray heating from illumination by the much stronger hard X-ray component can change the derived inner disc radius from being consistent with the last stable orbit (Rykoff et al. 2007) to being considerably larger, especially as the standard stress-free inner boundary condition is probably not appropriate for a truncated disc (Gierliński, Done & Page 2008).

However, it is also possible that the disc is considerably more complex. Firstly, even disc dominated high/soft spectra are not completely described by current disc models. They are broader than a simple sum of blackbodies, as expected due to relativistic smearing, and fit much better to models which incorporate this as well as full radiative transfer through the disc photosphere. While this makes a very nice physical picture, the disc spectra are even better fitted by phenomenological models, showing the limitations of the best current theoretical descriptions of disc spectra (Kolehmainen, Done & Diaz Trigo 2011). Secondly, the disc need not be a single structure. The inner edge of the truncated disc is not likely to be smooth. Clumps torn off the disc edge will spiral inwards into the hot flow, so will heat up by thermal conduction and evaporate. Before they completely merge into the hot flow they will form a small area, hotter, soft component, separate from the main body (and spectrum) of the truncated disc itself (see Figures 9 and 10 in Chiang et al. 2010).

As well as potential complexity of the disc spectrum, there is also potential complexity of the Compton continuum. At low luminosities the hot flow should be quite optically thin, in which case Compton scattering gives a bumpy rather than smooth power law spectrum. At higher luminosities the flow has higher optical depth, so can be inhomogeneous, with different parts of the flow giving different Comptonised spectra. This is required in order to produce the observed spectral lags, where the soft continuum varies before the harder continuum (Miyamoto et al. 1988; Kotov et al. 2001; Arevelo & Uttley 2006). Even more direct evidence for this is seen in the frequency resolved spectra, where the most rapidly variable parts of the flow (few 10s of milliseconds, presumably the inner regions) have harder spectra and less reflection than the more slowly variable emission (few seconds, presumably the outer parts of the flow: Revnivtsev et al. 1999). This gives rise to spectral curvature, which can be seen in broadband data (di Salvo et al. 2001; DGK07; Makishima et al. 2008; Kawabata & Mineshige 2010; Shidatsu et al. 2011). Fitting such continua with a single Comptonisation component leads to a requirement for an additional soft component, but this is connected to the Comptonisation region rather than to the disc.

Thus there is controversy both from instrumental effects for these bright sources (iron line), and over the physical interpretation of what is seen (origin of the soft X-ray component). We pick one particular instrument configuration, that of *XMM-Newton* timing mode, as this is specifically designed to observe bright sources, and systematically examine all low/hard state spectra taken in this mode to date. We assess the effects of both instrumental and modelling uncertainties, and show that both the iron line and intrinsic disc emission can be consistent with the truncated disc models in all current low/hard state spectra.

4.2 Observations and data analysis overview

Galactic black hole binaries are generally too bright to be observed in the standard imaging modes of CCD detectors, even in the low/hard state. We are therefore restricted to fast timing modes, which are currently less well calibrated than the standard imaging modes usually used for fainter sources. We select the EPIC-pn timing mode of *XMM-Newton*, as this is the mode which normally maximises the non-piled up count rate for low/hard state BHB.

There are 7 archival observations of a low/hard state from 4 sources in this mode: Cygnus X-1, Swift J1753-0127, GX 339−4 (4 datasets) and H1743-322. The latter object has an interstellar column density of $\sim 10^{22}$ cm^{-2}, substantially higher than the others. This means that the low energy continuum emission in H1743-322 is much less visible. This clearly reduces the constraint on the intrinsic disc emission, but also affects the iron line, as the latter depends on accurate modelling of the continuum emission underneath the line (see e.g. Kolehmainen et al. 2011), which in turn requires broad bandpass data. Thus we exclude H1743-322 from this analysis (see Table 4.1).

The data were reduced using the *XMM-Newton* Science Analysis System (SAS) v10.0. We applied the standard data reduction expressions, using single and double events and ignoring bad pixels. All data were extracted in full RAWY [1:200] and RAWX of 6 rows on either side of the central row. The SAS tool EPATPLOT was used to check for pile-up in all of the observations. This showed that Cyg X-1 and the brightest low/hard state observation of GX 339−4 were slightly affected. This was corrected by excluding 1 row in RAWX on both sides of the peak of the emission. Response and ancillary files were generated with SAS tasks RMFGEN and ARFGEN, respectively. The spectra were then rebinned using SPECGROUP, with an oversampling factor of 3, as recommended for all of the EPIC detectors.

The current level of EPIC instrument calibration is discussed at length in the

	Obsid	cts/s[1]	Exposure (s)
Cygnus X-1	0602610401	479 ± 0.4 (1111)	19970
GX 339−4 (GX4)	0654130401	362 ± 0.3 (944)	25290
GX 339−4 (GX3)	0204730301	257 ± 0.2	44360
GX 339−4 (GX2)	0204730201	240 ± 0.2	30480
GX 339−4 (GX1)	0605610201	125 ± 0.1	31750
Swift J1753-0127	0311590901	85 ± 0.1	40110

Table 4.1: Details of the observations analysed in this paper. The highly-absorbed BHB H1743-322 ($N_H \sim 16 \times 10^{21}$) was excluded due to the absorption's obscuring effect at low energies. The binary parameters used in this paper are Cygnus X-1: $M = 20M_\odot$, D = 24kpc, $i = 30°$, GX 339−4: $M = 10M_\odot$, D = 8kpc, $i = 60°$ and Swift J1753: $M = 9M_\odot$, D = 6kpc, $i = 60°$.

latest version of the XMM-Newton Calibration Technical Note (0083)[2]. The main issue for concern is the ubiquitous problem of X-ray loading (XRL). The 'quiet' level of the electron current in each pixel is determined from exposures at the beginning of each observation, and this offset map is automatically subtracted from the data by the onboard processor. However, for bright sources, and especially bright, hard sources, this electron current is contaminated by the source itself. The source pixels have too much electron current subtracted, leading to a constant offset in the gain. This problem affects all *XMM-Newton* fast modes. It is currently under investigation, but is not yet resolved.

The charge transfer inefficiency (CTI) is a separate issue, and does not include the effects of XRL. Damage to the CCD means that there are electron traps, so not all charge is transfered on readout. This charge transfer inefficiency is reduced for bright sources, as the multiple electrons produced by high X-ray illumination fill the

[2]http://xmm.vilspa.esa.es/external/xmm_sw_cal/calib/documentation.shtml

holes, so that the remaining charge can be efficiently transfered. This makes the CTI rate dependent, resulting in a linear gain shift with energy which depends on source count rate. This is currently corrected by the SAS task EPFAST, but the parameters for the gain shift were derived assuming that the data were affected only by a linear gain shift, while in reality they are affected by a combination of a linear gain shift from CTI and a constant offset from XRL. We follow current recommendations and use EPFAST on all our data, but at these relatively low count rates (compared to the ones seen in burst mode) the correction did not cause any noticeable changes in the data.

The wings of the point-spread function of the EPIC-pn extend further than the data collection region in timing mode, which means that selecting a source-free region for background subtraction is not possible (e.g. Done & Diaz Trigo 2011). However, the 10–15 keV lightcurve from the outer regions of the EPIC-pn can still be used to identify and exclude regions of background flaring, and these can be checked from outer chip lightcurves from the MOS imaging data, when available. We also use blank sky backgrounds in timing mode to check that the background is indeed negligible for these bright, hard sources. Table 4.1 shows the resulting effective exposure time after excluding background flaring.

We also extract quasi-simultaneous *RXTE* data on all of our objects and reduce these using the standard data reduction methods. These are further discussed in Section 4.3.1.

4.3 Low/hard state spectral overview

We start by fitting the data with a single power law model to illustrate any possible deviations from a pure power law shape. Figure 4.1 shows the 3–10 keV data unfolded with this model, where for plotting purposes we have multiplied Cyg X-1 and Swift J1753-0127 (hereafter S1753) by $(M/10)(8/D)^2$ so that the spectra are

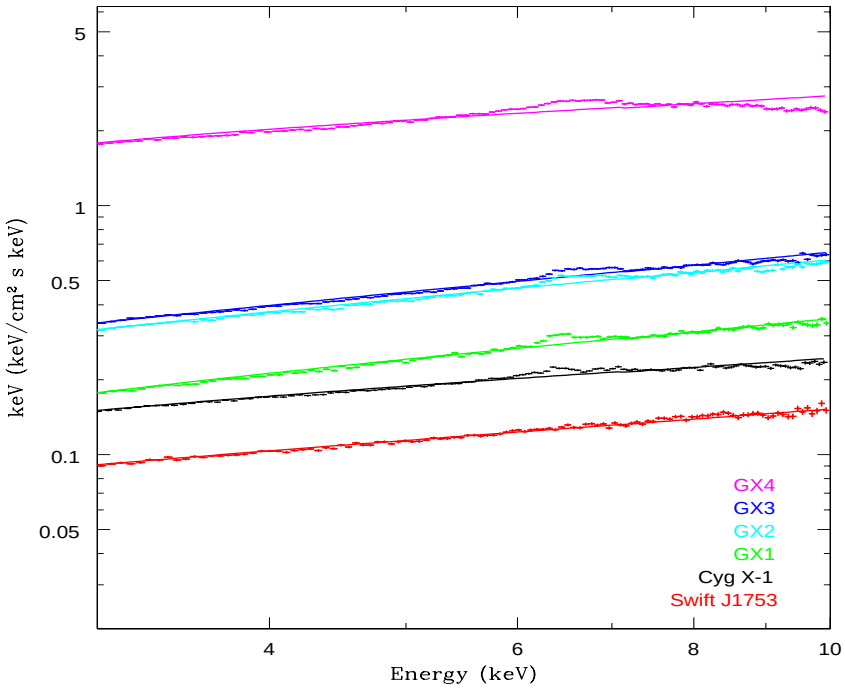

Figure 4.1: All the observations analysed in this paper, unfolded by a simple power law model to illustrate the spectral deviations from the continuum. The spectra are plotted in order of increasing luminosity in the 3–10 keV range.

normalised in relative L/L_{Edd}. Plainly the excess emission around the line increases in both strength and width with increasing L/L_{Edd}, qualitatively consistent with the predictions of the truncated disc model. It is also clear that there is a narrow line core in GX 339−4 and Cyg X-1, probably from illumination of the outer disc.

4.3.1 Cross-Calibration with RXTE

Figure 4.1 shows that S1753 has the simplest spectrum, with very little spectral features or curvature. Fig 4.2 shows the simultaneous EPIC-pn/PCA data. This shows a clear discrepancy in the cross-calibration of the two instruments in the region

of overlap (3-10 keV), also noted in Hiemstra et al. (2011) for the bright BHB XTE J1652. However, for S1753 there is almost no spectral complexity to mask the issues. The two instruments clearly have different spectral indices, with $\Delta\Gamma = 0.11^{+0.01}_{-0.02}$, even restricting the fit to the 3–10 keV region where the data overlap. We find similar discrepancies in spectral indices in all our data in the overlapping 3–10 keV bandpass, though here the evident complexity around the iron line could affect the modelling.

One way to assess the status of the cross-calibration between the EPIC-pn fast timing mode and PCA is to use the Crab data, though this is necessarily in EPIC-pn burst mode rather than timing mode due to the very high count rate of the Crab. Appendix B gives details of these data, and shows that the Crab also shows a similarly discrepant spectral index with the PCA (see Appendix B). We might expect that the discrepancies in cross-calibration are worse for the much higher count rate Crab data if this effect is due to XRL. However, we find that the offset in spectral index is similar, with $\Delta\alpha = 0.15\pm$ for the 3-10 keV region where the XMM-Newton and RXTE PCA data directly overlap. Thus this may instead be connected to the effective area at high energies. Irrespective of the origin, the offset in spectral index plainly means that we cannot fit the data together. Hence we focus the rest of this analysis solely on the EPIC-pn data as we are interested in the iron line profile and the soft continuum.

4.4 Lowest L/L_{Edd}: Swift J1753-0127

We start the more detailed analysis with the simplest spectrum, S1753. Previous work on this spectrum has shown that there is curvature in the continuum, which can be described either by a disc component or by reflection (R10, Hiemstra et al. 2010). However, both of these would imply that the inner disc is present at some level, in conflict with the simplest truncated disc model.

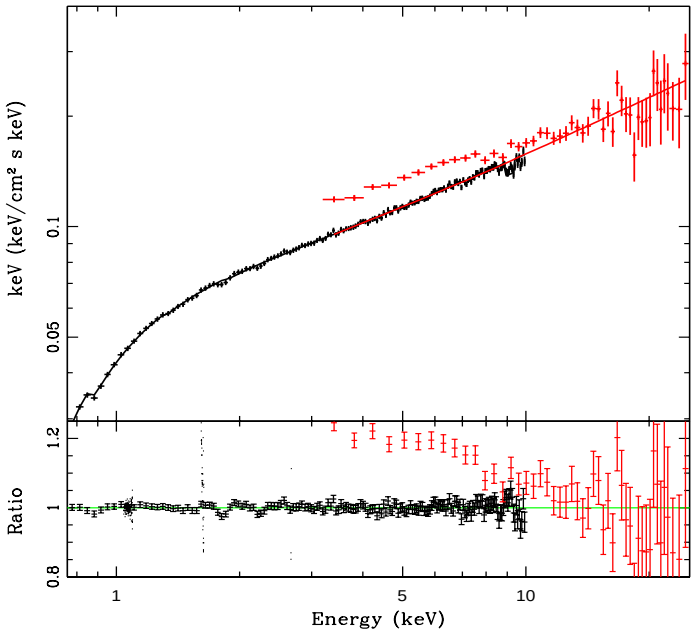

Figure 4.2: Joint EPIC-pn-PCA fit of the S1753 observation fitted in the joint energy range of 0.7–25 keV. The data are consistent only above 7 keV, with the difference in photon indices of $\Delta\Gamma \sim 0.11$. Due to this obvious disagreement in cross-correlation, the rest of this analysis focuses solely on the EPIC-pn data.

We confirm that there is indeed spectral curvature by fitting a series of models of increasing complexity. We start with a single absorbed Comptonisation component, described by the NTHCOMP model. We assume that the seed photons have blackbody shape which gives $\chi^2 = 196/163$ for a seed photon temperature of ~ 0.2 keV. We add a disc spectrum with inner disc temperature tied to the seed photon temperature for Comptonisation. This gives a significantly better fit with $\chi^2 = 169/162$. The disc normalisation of 400^{+180}_{-100} implies an apparent radius of 17 km for the fiducial values of distance and inclination. This gives a corrected radius of 20 km for a colour correction factor of 1.7 and stress free inner boundary condition of 0.41 (Kubota et al. 2001), which is $1.3R_g$ for the fiducial mass of $10M_\odot$. Even without the stress

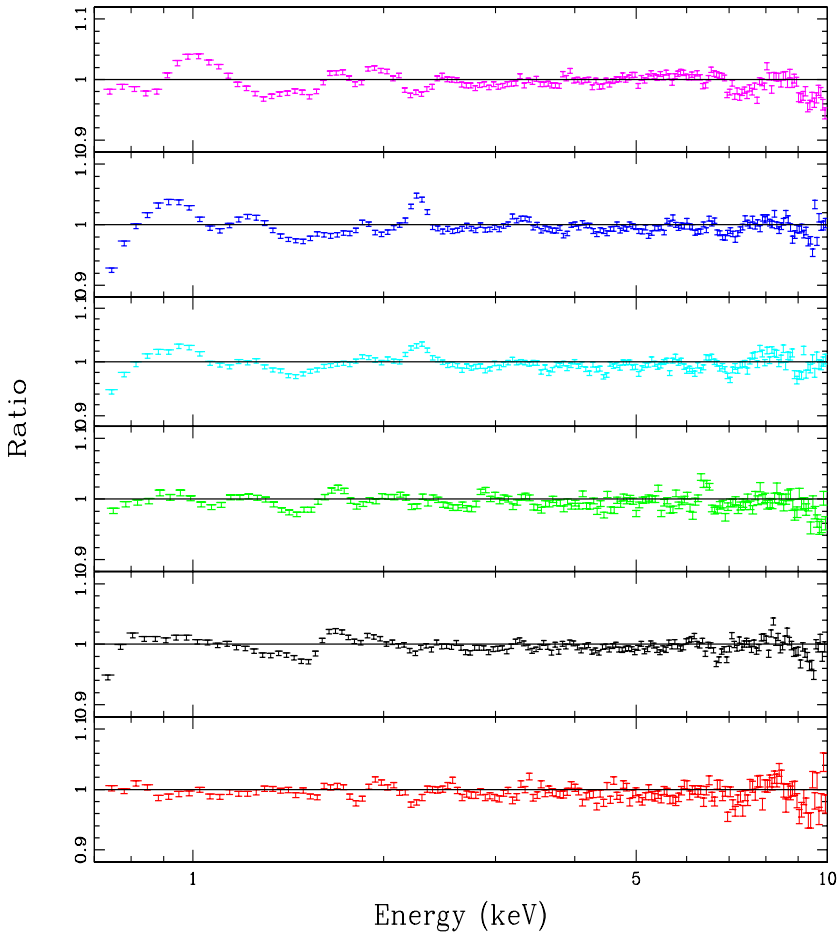

Figure 4.3: Data/model ratio for all spectra, when fitted with DISKBB+NTHCOMP+REFLECTION model.

free inner boundary the radius is only $3R_g$, so this is completely inconsistent with a truncated disc. Instead, this small emitting area could be indicative of small clumps at large radii torn from the truncated disc edge, heated by conduction as they spiral into the hot flow (Chiang et al. 2010).

Alternatively, this soft component could be Comptonised emission from a smoothly truncated disc where the emission from the inner edge does not completely thermalise. We add an optically thick Compton component COMPTT, again with seed photons tied to the disc temperature. This is not a significantly better fit ($\chi^2 = 161/159$), but the disc temperature decreases so its normalisation increases. However, the upper limit on the disc norm of 2.6×10^4 ($< 10R_g$ or $< 25R_g$ with and without the boundary condition, respectively) is still a little small for the truncated disc models.

Instead, we get an even better fit using the EQPAIR Comptonisation model with no additional soft component ($\chi^2_\nu = 160/163$). This model calculates the full Comptonised emission from each individual Compton scattering order, so at low optical depths and high temperatures (best fit is $\tau \sim 0.3$, $kT_e = 300$ keV) the excess soft X-ray flux is fitted by the first order scattering from seed photons from the disc at 11 ± 1 eV. The disc normalisation is completely unconstrained at these low temperatures, so is consistent with a truncated disc.

Thus the *spectrum* of S1753 is consistent within current instrumental uncertainties as being simply described by a single Comptonisation continuum from low optical depth material, with no disc required in either direct or reflected emission, as predicted by the truncated disc models at low L/L_{Edd}. However, this is not consistent with the *timing* behaviour. Fast time variability shows clearly that there *is* an additional component at soft energies (Fig 3, Uttley et al. 2011). This soft component leads the harder X-rays by ~ 0.1 s, far too long to be the light crossing time lags between individual Compton scattering orders (see also Miyamoto & Kitamoto 1989). Instead, these almost certainly are viscous lags from propagating fluctuations, with

fluctuations in a spectrally softer component at larger radii propagating down to modulate a harder component produced at smaller radii (Kotov et al 2001; Arevalo & Uttley 2006).

Hence we do want to include a separate soft component in the XMM-Newton bandpass in these data. If this is roughly blackbody in shape then it could either represent the inner edge of an untruncated disc around an extreme spin black hole, or small clumps torn from the edge of a disc which is truncated at much larger radii. Clumps have the advantage of also giving a clear origin for variability, whereas a disc down to the last stable orbit in the disc dominated states has remarkably little variability (e.g. Churazov et al. 2001).

Observationally, these two possibilities predict different reflection signatures. Clumps at large radii subtend very little solid angle, so give a small reflected spectrum which is not strongly smeared. Conversely, an inner disc round a high spin black hole should be physically close to the X-ray source, so should give a larger reflected fraction and strong relativistic smearing. We include reflection of the Comptonisation continuum from relativistically smeared, ionised material with (TBABS×(DISKBB+NTHCOMP+KDBLUR×RFXCONV×NTHCOMP)), which gives $\chi^2_\nu = 141/159$, $\Delta\chi^2 = 25$ for three additional parameters better than the original DISKBB+NTHCOMP continuum model. This reflected emission requires strong relativistic smearing, with $r_{in} = 1.9^{+6}_{-0.7} R_g$ even though the amount of reflection is small ($\Omega/2\pi = 0.05^{+0.03}_{-0.02}$). The reason that the data require such extreme spin is that the drop from the blue wing of the iron line is at ~ 8.5 keV (Fig. 4.4), so requiring large Doppler blueshifting from the rest line energy for He-like iron (as implied by the ionisation state) of 6.7 keV.

At first sight this strongly supports the untruncated disc. However, the parameters are puzzling in this geometry. The amount of reflection is very small, which, together with the hard continuum, supports models where the X-rays are beamed away from the disc (e.g. Malzac, Beloborodov & Poutanen 2001). However, this also

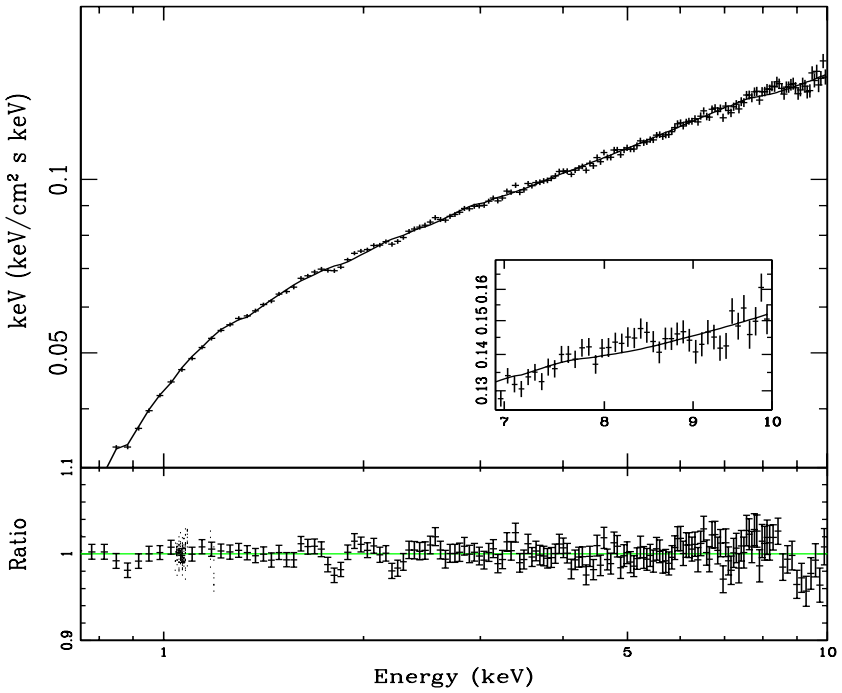

Figure 4.4: The S1753 observation modelled with a simple DISKBB+NTHCOMP continuum plus reflection, and zoomed in to the 7–10 keV region. A ~ 6 per cent dip is visible in the residuals at $\sim$9 keV.

changes the illuminating radiation pattern, defocusing it away from the disc central regions. Yet the reflection spectrum requires that the inner disc is illuminated in order to produce the observed smearing. This, together with the fact that the features being fitted by reflection are very small (less than a few percent in a ratio plot) means that they are critically dependent on the current calibration of the XMM-Newton EPIC-pn timing mode. We explore this in more detail below by using a combination of all the low/hard state spectra, and the Crab data.

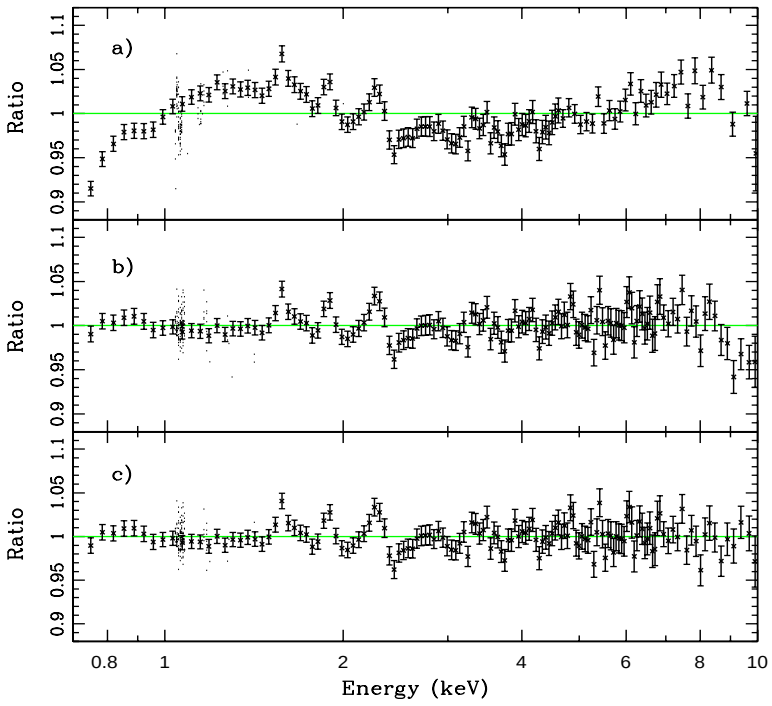

Figure 4.5: *Upper panel a):* Residuals from a double power law model of the Crab with EPFAST correction. The features between ∼1.6–2.4 keV are due to the CTI correction, which seems to have over-compensated the characteristically negative residuals. *Middle panel b):* A double power law model to account for both nebular and pulsar contributions to the observed spectrum removes the dip at low energies. *Lower panel c):* Residuals from the same double power law model as the middle panel, with the additional NOTCH absorption line fitted at 9.39 keV.

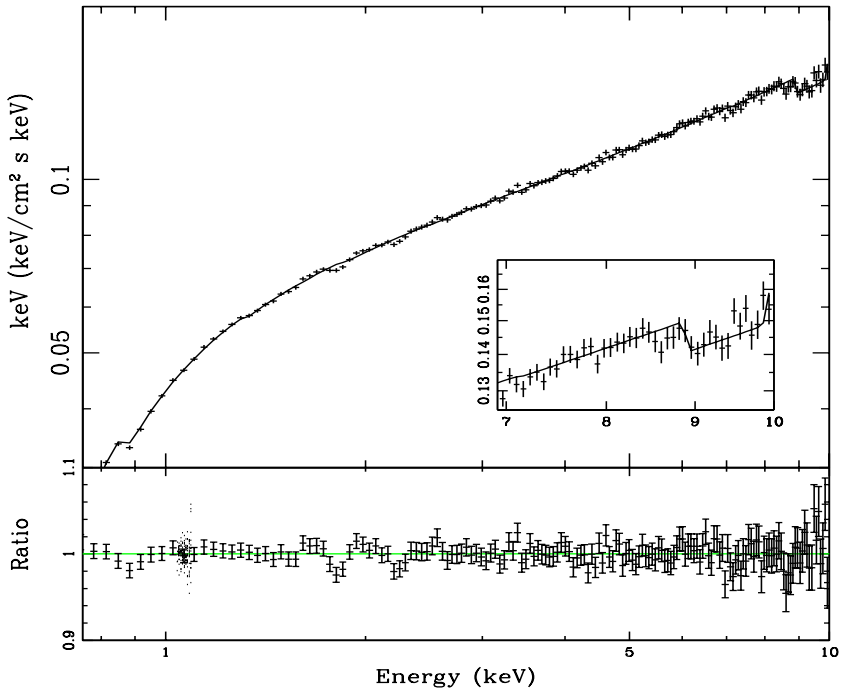

Figure 4.6: The S1753 observation modelled as in Figure 4.4, but with a broad absorption line fixed at 9.39 keV as described in Section 4.5.

4.5 All low/hard state spectra and limitations of the current EPIC-pn timing mode response

We fit all the spectra with the disc plus single Comptonisation model i.e. assume that there is a real additional soft component. This is supported by the fact that Cyg X-1 and GX1,2,3 all have similar lag spectra to S1753 (GX4 is too recent an observation to be included in Uttley et al. 2011). Figure 4.1 shows that all the spectra other than S1753 have obvious residuals from reflection, so we fit the model TBABS×(DISKBB+NTHCOMP+KDBLUR×RFXCONV×NTHCOMP). Both GX 339−4 and Cyg X-1 also require a small, narrow, neutral core to the iron line, which is

probably due to reflection from the raised rim of the outer disc. We include this as a narrow (σ fixed to 0.01 keV) neutral line (energy fixed at 6.4 keV) in the model. All our fit parameters are shown in Table 4.2 and residuals are plotted in Figure 4.3. This fit for GX4 is very poorly constrained, as the fit is dominated by highly ionised reflection which is degenerate with the underlying Compton continuum.

The residuals to the best fit models clearly show increasing problems around the edges in the response matrix ($\sim$1.8 and $\sim$2.2 keV) as the source count rate increases, presumably due to the uncorrected effect of XRL. However, spectrum GX3, taken 1 day after spectrum GX2 (consecutive XMM-Newton orbits) and with very similar count rate and spectral shape, has stronger residuals at 2.2 keV, indicating a different gain shift. This cannot be due to different XRL as the count rate is very similar. Instead it shows the limiting stability ($\sim$ 5 eV) of the EPIC-pn gain. The stronger residuals around the instrument edges affect some of the fit parameters, so that the disc normalisation changes significantly. This is almost certainly an artifact, as real changes in geometry are not likely to occur on such short timescales without a corresponding change in flux. Hence it seems most likely that the difference between GX2 and GX3 is driven mainly by unknown, time-dependent stability issues in the EPIC-pn response. In the remaining discussion in this section we ignore GX3.

There is also an excess at 1 keV, which appears systematically stronger at higher L/L_{Edd}. Such an excess is often seen in heavily absorbed systems (e.g. Heimstra et al. 2011), where it may be a symptom of the uncertainties in the low energy tail of the response to higher energy photons ((CAL-TN-0083[3])). However, this should not be an issue for the low-to-moderate absorption columns required here. Thus it is likely to be real. Nonetheless, it is not easy to interpret physically, despite the energy pointing to iron L emission, as the reflector required to make the iron K line is too highly ionised to produce much iron L. A reflection origin would also impact

[3]http://xmm.vilspa.esa.es/external/xmm_sw_cal/calib/documentation.shtml

on the lag spectrum, turning the generic hard lag into a lead at these energies as the reflected emission will follow the hard X-ray illumination (e.g. Madej et al. 2012). The lag spectra show no such feature (Uttley et al. 2011). Hence this most probably shows that the soft component is not well modelled by DISKBB, but instead has a more complex spectrum.

There is also a drop above 9 keV which is always present. This feature could be real if there are substantial amounts of ionised H-like iron as this has a K-edge energy of 9.23 keV (e.g. Hiemstra et al. 2011). However, it would then be expected to vary with the amount of ionised reflection, yet this drop has the same 5% level irrespective of L/L_{Edd}. Thus it appears more likely to be a calibration issue at these highest energies rather than an intrinsic feature in the spectra.

We investigate the calibration issues using the Crab data. Fig 4.5 shows a series of residuals from spectral fits to one of the on-axis observations of the Crab (see Appendix B). The top panel shows residuals to a single power law, with $\Gamma = 2.1$. This is a similar fit to those in Weisskoft et al. (2010), but here the more appropriate binning does not suppress the visibility of the high energy residuals. There are clear residuals at 1.5 keV and 9 keV which appear fairly similar to the ones in our data. However, a single power law is not a good approximation to the spectrum from the Crab, as there are both nebular and pulsar contributions. Instead, a double power law fit removes the soft residuals, but not the high energy feature at 9 keV (middle panel). We model this with a NOTCH, with width fixed at 1 keV and find a significant reduction in χ^2 (from 260/162 to 231/160) for an energy 9.39±0.01 keV, with a covering fraction of 0.06±0.02 (i.e. equivalent width 60 eV). The residuals in Fig 4.5c are now flat. This feature is not significantly present in the other on-axis Crab spectrum (see Appendix B) so we regard this instead as showing the limitations of our current knowledge of the response.

We revisit all our spectral fits with this caveat. For S1753 the drop at high energies in the data was the key feature which meant that highly smeared reflection was

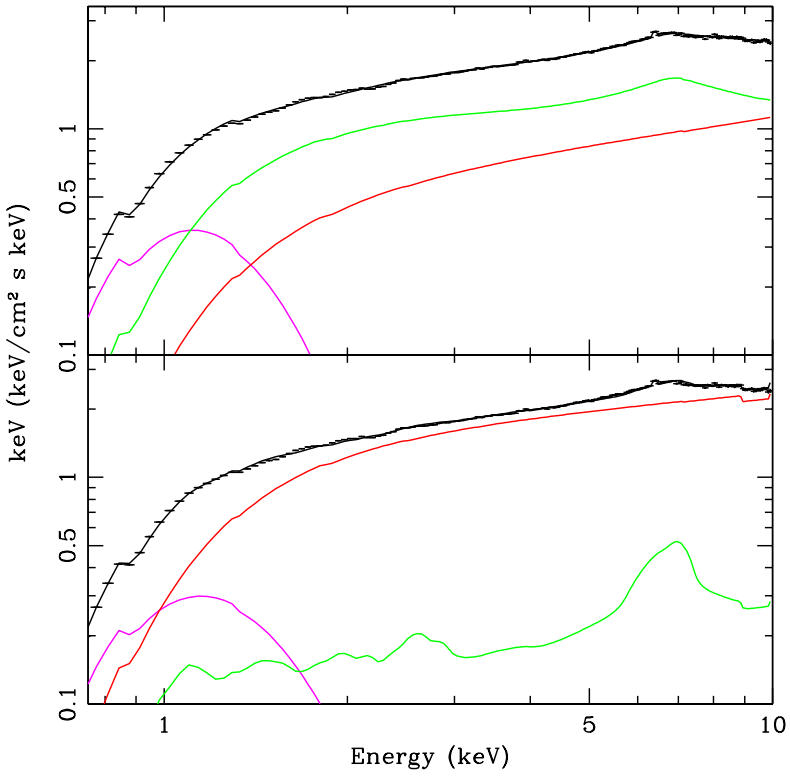

Figure 4.7: GX4 fits without the notch (top panel) and with the notch (bottom panel), illustrating the different spectral decompositions of two different solutions to the same model.

significantly detected. The reflection component is now only marginally significant ($\Delta\chi^2 = 12$ for 3 additional degrees of freedom) with the NOTCH, but all the model parameters are similar within the uncertainties. This includes the inner radius, which is still small, showing that the best fit model has reflection which is strongly smeared, but the driver for this now is the soft excess at low energies produced by ionisation reflection rather than the iron line region. This suggests that a more complex continuum can completely remove the requirement for reflection. We explore this in more detail in the next section.

None of the fits to GX1,2,3 and Cyg X-1 are significantly changed by inclusion of the NOTCH, as reflection is much more significantly detected in these datasets, and is less strongly smeared ($r_{in,ref} > 100R_g$) than in S1753. This makes it much less dependent on the high energy region, so the reflection parameters are robust to small changes in effective area at 9-10 keV. However, for GX4, the much broader reflection features mean that the high energy calibration again makes a difference. Without the notch, the amount of reflection is larger than expected for isotropic illumination, with $\Omega/2\pi = 1.3$. The spectral broadening of the iron features which is so evident in Fig 1 is driven mainly by its higher ionisation state, so the derived inner radius is surprisingly large, with $r_{in,ref} > 100R_g$. With the notch the amount of reflection drops to $\Omega/2\pi = 0.35$, its ionisation is similar to that in GX1,2,3 and the obvious broadening is now due to a smaller inner radius, with $r_{in,ref} = 50R_g$. These very different spectral decompositions are shown in Figure 4.7.

	TBabs(diskbb+nthComp+Gaussian+kdblur×rfxconv×nthComp)									
	$N_H(\times 10^{21})$	$T_{in}(keV)$	$N_{Disc}(\times 10^3)$	Γ	N_{comp}	R_{in} (R_g)	$f = \Omega/2\pi$	logξ	eW (eV)	χ^2/ d.o.f
Cyg X-1	4.8 ± 0.02	0.21 ± 0.01	170^{+40}_{-30}	1.69 ± 0.01	1.48	16 ± 4	0.07 ± 0.01	$2.80^{+0.11}_{-0.05}$	8 ± 2	294/158
GX4	0.66 ± 0.02	0.18 ± 0.01	660^{+100}_{-80}	1.58 ± 0.02	0.27	$2.2^{*}_{-0.5}$	3.54 ± 0.02	270^{*}_{-150}	8 ± 3	381/158
GX3	3.7 ± 0.01	0.31 ± 0.01	$1.6^{+0.4}_{-0.2}$	1.55 ± 0.01	0.14	92^{+35}_{-20}	$0.15^{+0.01}_{-0.02}$	$2.69^{+0.01}_{-0.11}$	5 ± 3	552/158
GX2	3.9 ± 0.2	0.27 ± 0.02	$2.6^{+0.9}_{-0.7}$	1.56 ± 0.01	0.14	85^{+40}_{-25}	$0.17^{+0.04}_{-0.03}$	$2.53^{+0.17}_{-0.08}$	5 ± 3	358/158
GX1	4.4 ± 0.2	$0.24^{+0.01}_{-0.02}$	$2.6^{+1.2}_{-0.8}$	1.53 ± 0.01	9.0	110^{+80}_{-40}	$0.17^{+0.04}_{-0.03}$	$2.37^{+0.05}_{-0.02}$	13 ± 3	154/158
S1753	$0.12^{+0.04}_{-0.02}$	$0.20^{+0.10}_{-0.05}$	$0^{+2.4}_{*}$	1.60 ± 0.01	0.05	$1.9^{+6.9}_{-0.6}$	$0.06^{+0.04}_{-0.02}$	$2.76^{+0.21}_{-0.05}$		140/159

Table 4.2: The best fit parameters for the single Comptonisation model.

TBabs(diskbb+comptt+nthComp+Gaussian+kdblur×rfxconv×nthComp)										
	T_{in}(kev)	$N_{Disc}(\times 10^3)$	τ	N_{comp}	Γ	$N_{nthcomp}$	$R_{in}(R_g)$	$f = \Omega/2\pi$	logξ	χ^2/ d.o.f
Cyg X-1	0.17 ± 0.01	490 ± 6	$2.3^{+0.1}_{-0.2}$	0.32	$1.40^{+0.03}_{*}$	0.56	$4.5^{+0.6}_{-0.5}$	$0.15^{+0.04}_{-0.02}$	2.72 ± 0.02	222/157
GX4	0.21 ± 0.01	140 ± 20	*	*	1.73 ± 0.01	1.1	47^{+10}_{-7}	$0.35^{\pm}0.05$	2.44 ± 0.04	381/158
GX3	0.16 ± 0.01	71^{+12}_{-9}	1.5 ± 0.1	0.044	$1.4^{+0.01}_{*}$	0.13	140^{+60}_{-50}	0.18 ± 0.03	$2.49^{+0.18}_{-0.04}$	360/150
GX2	0.16 ± 0.01	65 ± 9	1.6 ± 0.1	0.036	$1.4^{+0.01}_{*}$	0.12	115^{+85}_{-35}	0.19 ± 0.03	$2.45^{+0.07}_{-0.04}$	212/157
GX1	0.17 ± 0.01	26^{+5}_{-3}	1.8 ± 0.2	0.014	$1.4^{+0.03}_{*}$	0.07	150^{*}_{-50}	$0.17^{+0.04}_{-0.03}$	2.35 ± 0.03	150/157
S1753	$0.15^{+0.01}_{-0.04}$	$6.7^{+3.4}_{-1.0}$	2.2 ± 0.8	0.011	$1.4^{+0.1}_{*}$	0.03	*	*	*	141/161

Table 4.3: The best fit parameters for the double Comptonisation model.

4.6 Discussion and conclusions

4.6.1 Disc, double Comptonisation and reflection

The spectral lags clearly show that there is a separate soft component in Swift J1753, GX1,2,3 and Cyg X-1 (Uttley et al. 2011). While GX4 is not included in that study, it is plain from the spectrum alone that there is a separate soft component in these data also, as L_{soft}/L_{tot} is much larger in this dataset than in the others. However, the spectral lags are not confined to the soft component alone. It has long been clear that there is a complex pattern of hard lags in Compton continuum, which requires an inhomogeneous emission region. The most successful model to date can match these observed lags by fluctuations propagating down through the accretion flow, where the outer parts of the flow have a softer spectrum than the inner. Two Comptonisation components (together with the disc and reflected emission) are also required to adequately model the low/hard state spectra of BHB (di Salvo et al. 2000; Makishima et al. 2008). We describe this additional Comptonisation with the COMPTT model. However, the more limited bandpass of our data means that we cannot constrain all the parameters, so we fix the electron temperature of this additional component at 10 keV. We assume that both soft and hard Compton components have the same seed photon energy, and that this represents the temperature of the disc itself.

An additional soft component generically means that the disc component goes down to lower temperatures, and its normalisation increases, as does the interstellar column density. This is a nice feature of this additional component, as all the columns derived from the previous fits are somewhat lower than expected, except for GX4. However, again our data cannot constrain all of the parameters, so we fix N_H at the expected value for all of our data (0.21, 0.55 and 0.55×10^{22} in S1753, GX 339−4 and Cyg X-1, respectively). We include the notch with parameters fixed to those of

the Crab, and tabulate results in Table 4.3.

This model gives significantly better fits than the single Compton continuum model (compare with Table 4.2) for all spectra except for GX4. In GX4 the observed, dominant, soft component has a shape which is very similar to a disc. By contrast, in all the other spectra where the soft component makes only a small contribution to the spectrum below 1 keV, the shape of this soft component is much better described by themal emission plus a broader spectrum. Conversely, in S1753, the combination of this broader soft emission plus the notch means that reflection is not significantly detected.

4.6.2 The disc inner radius

Figure 4.8 shows the relation between the disc inner radius derived from reflection and from the soft component assuming that it is indeed the disc. The inner radius from reflection in all these fits is very different to that determined from the soft X-ray component. There is no requirement for any reflection in S1753 (with notch), yet the soft component emitting area is extremely small. GX 1,2, and Cyg X-1 all require a small amount of reflection, $\Omega/2\pi \sim 0.1 - 0.2$, but this is not strongly smeared, with typical values of $r_{in,ref} > 100R_g$. This is in sharp contrast to the soft excess normalisation in these data if this is interpreted as the inner edge of the disc. GX1 has a disc normalisation of 2600, equivalent to an apparent radius of 58 km, or 68 km corrected for colour temperature and stress free inner boundary i.e. $r_{in} = 4.6R_g$ ($5.4R_g$ for GX2). GX4 is the only one where the disc normalisation is consistent with the amount of relativistic smearing (with notch), at $r_{in} = 50R_g$ (Figure 4.8).

Thus the data are consistent with the truncated disc picture if the soft component in the low luminosity low/hard state is from small clumps torn from the inner edge of the truncated disc. The main disc structure has too low a temperature to contribute

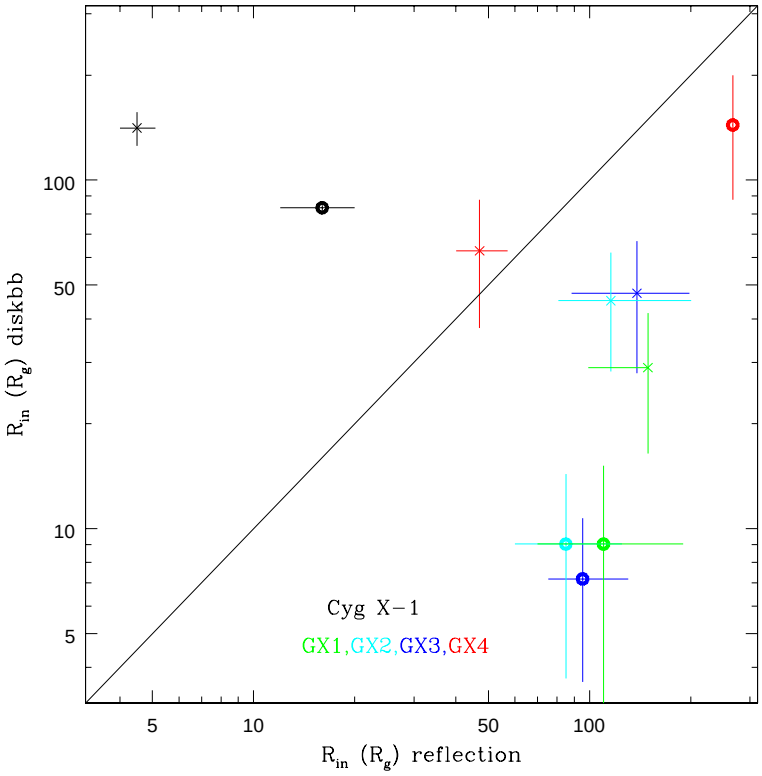

Figure 4.8: The relation between the disc inner radii derived from the disc normalisation and reflection. The line illustrates where the points would lie if these two methods gave consistent results. The circles refer to the inner radius derived from the DISKBB+NTHCOMP model (Table 4.2), and the crossed to the inner radius derived from the double Compton component model (Table 4.3). GX4 disc inner radius, as derived from the double Compton component model, is the only one showing consistency within the errors.

to the soft X-ray bandpass. The small solid angle and lack of strong broadening of the reflected emission are consistent with this structure. In the brighter low/hard state spectra (GX4), the disc extends down further, so contributes directly to the soft X-ray flux (Chiang et al. 2010).

Iron line profiles with very broad red wings have been widely reported in the low/hard state of X-ray binaries (e.g. Miller et al. 2006, R10). This is not the case for any of the spectra reported here. The data show a clear trend in behaviour as a function of L/L_{Edd}. At the lowest luminosities the iron line is not required, then reflection becomes a significant feature in the data, though with small solid angle $\Omega/2\pi \sim 0.2$. This reflecting material is significantly ionised. For bright low/hard states (GX4) reflection is much stronger, and much more obviously broadened, though most of this is modelled by higher ionisation state of the disc rather than higher reflection fraction.

Thus none of our sample spectra seem to require the accretion disc to extend down to the last stable orbit. In fact, the only observation that shows a disc inner radius below a Schwarzschild black hole is S1653, but even then the observed feature can be explained through an instrumental effect. We find that the black hole spin cannot be constrained in these data using a self-consistent reflection model, as the derived line profile appears too narrow and the amount of relativistic smearing suggests that the observed line originates from radii far from the black hole. The only case where the line does look intrinsically broad is GX4, but the spectrum has a complex continuum, where issues with modelling are apparent and affect the derived line profile.

4.7 Appendix B: Comparison to Crab spectra

To test the level of instrumental effects mentioned in Sections 4.3 and 4.2, we decided to take a closer look at the calibration source itself. Essentially, features seen in the spectra of black hole binaries are not expected to be found in the Crab. Thus we tried to shed more light into the very concerning cross-calibrational disagreement seen in Figure 4.2 by comparing EPIC-pn and PCA observations of the Crab.

The fact that the Crab is a pulsar surrounded by a nebula adds complications to the comparison. First of all, since the PCA has a wider field-of-view than the EPIC-pn, it covers a bigger portion of the nebula. Secondly, due to the brightness of the Crab, most of the *XMM-Newton* observations are taken in a slightly offset position. There are only two archived EPIC-pn burst mode observations (01610960401 and 0160960601) that were taken in a bore-sight position, thus allowing the whole nebula to be fully encompassed by the aperture (Weisskopf et al. 2010).

We coupled the EPIC-pn observation 01610960401 with a PCA observation (90802-02-05-00), taken 5 days prior to the *XMM-Newton* one. Since it seems that the rate-dependent CTI correction task EPFAST does not properly correct for these EPIC-pn Crab spectra (see Figure 4.9 and features around 2 keV in Figure 4.5), we considered both EPFAST-corrected and non-corrected EPIC-pn spectra for the comparison. Figure 4.10 shows the data fitted with an absorbed two-component power law, with the EPFAST-corrected EPIC-pn data in black, non-corrected in green and the PCA in red. The difference in photon index is blatantly evident even by eye, and fitting the spectra in the combined energy range of 0.7–25 keV gives a difference in photon index of $\Delta\Gamma$=0.16 $\pm$ 0.01 between the CTI-corrected EPIC-pn and the PCA spectra. We tested this further by fitting only above 3 keV to omit any absorption effects that might affect the EPIC-pn spectra at low energies. This yielded individual indices of $1.97^{+0.03}_{-0.06}$ for the EPFAST-corrected EPIC-pn, 2.14 for the non-corrected EPIC-pn and 2.12 for the PCA. Thus the EPFAST-corrected spectrum shows stronger disagreement

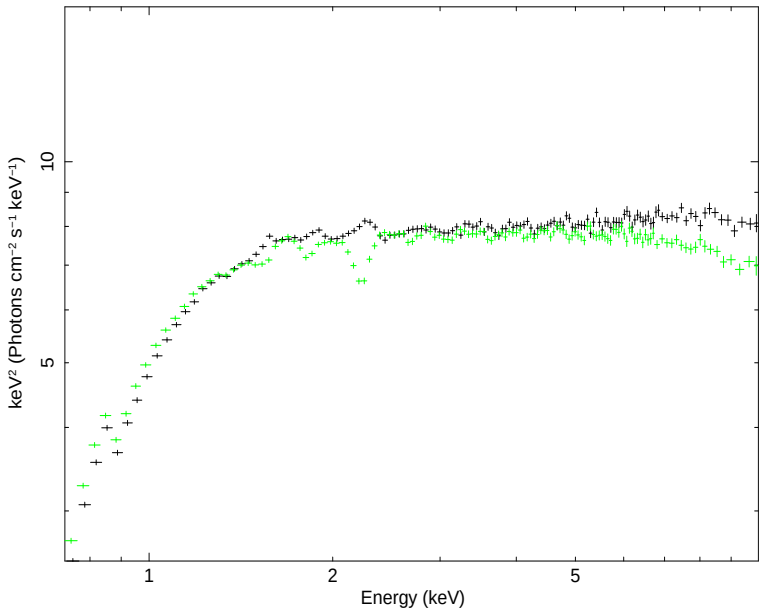

Figure 4.9: Crab observation 01610960401 with EPFAST correction (in black) and without (in green). The rate-dependent CTI effects are visible in the non-corrected data, whereas the corrected one shows over-compensation around the instrumental Si and Au-edges.

with the PCA, whereas the non-corrected spectrum rolls over above ∼8 keV in a way that wrongly resembles the PCA spectral index. In addition, the absorption feature seen in Figure 4.5 is even greater in a non-corrected spectrum, with a >15% residual at 9 keV.

A discrepancy this noticeable is obviously very concerning. One possibility is that it could be due to an incorrect energy-dependency of the rate-dependent CTI and the calibration effort is currently on-going. However, dealing with a burst mode observation of the Crab nebula is complex in itself. None of the data reduction and/or analysis choices are trivial. Issues such as centralising the extraction region at the peak of the emission in RAWX, the size of the extraction region and subtracting a background from the source all affect the resulting spectrum. It is also currently

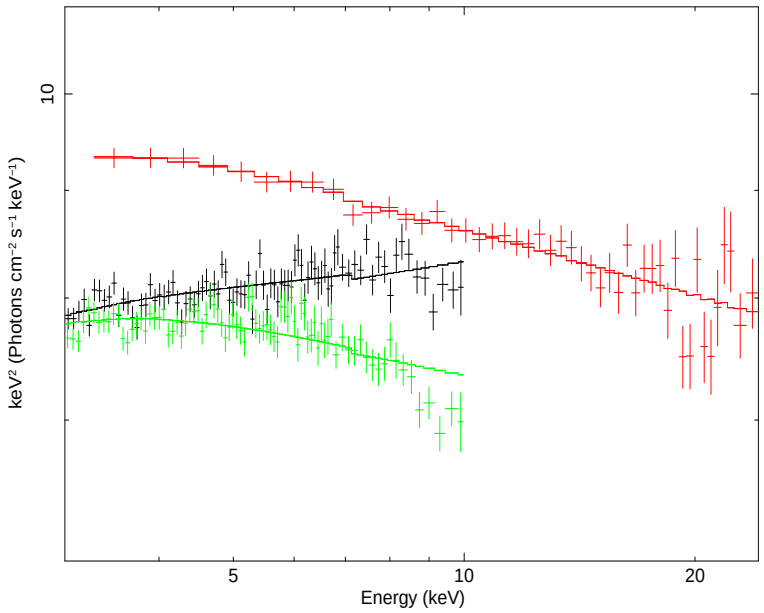

Figure 4.10: Same as Figure 4.9, combined with the corresponding PCA observation in red. EPFAST has corrected for the turnover above ∼8 keV in the non-corrected data, but rather over-estimated the instrumental edges at ∼1.85 keV and ∼2.2 keV.

impossible to correct for the unknown universal effect of XRL in the data. All these factors in mind, we conclude that the discrepancy in cross-calibration limits joint EPIC-pn/PCA spectral fitting below ∼7 keV.

Chapter 5

LMC X-3: The best test for accretion disc models

5.1 Introduction

The emission from the accretion disc tells us how the gravitational energy is converted to radiation by the black hole. The simplest models of the accretion flow assume that the material forms a disc in which the gravitational potential energy released by the in-falling material can thermalise. This gives rise to a characteristic spectrum made up of a sum over all radii of these different temperature blackbody components, $T \propto R^{-3/4}$ at $R >> R_{in}$. This relation is implemented in the simple DISKBB model, and correcting this for a stress-free inner boundary condition produces the classical Shakura & Sunyaev accretion disc, which was expanded to include general relativistic effects by Novikov & Thorne (1973). More corrections come from the fact that emission from each radius is only a true blackbody if the disc is effectively optically thick to absorption at all frequencies. Continuum (free-free) absorption drops as a function of frequency, so the highest energy photons from each radius are unlikely to thermalise. Thus this modified blackbody has an effective temperature of a factor f_{col} higher than for complete thermalisation (Shimura and Takahara, 1995). Smearing this modified blackbody spectrum by a combination of special and general relativistic effects for a spinning black hole is incorporated in the KERRBB model (Li et al. 2005).

However, assuming that the intrinsic spectrum has a modified blackbody shape

is only an approximation to the full radiative problem. Photo-electric absorption from partially ionised metals becomes important at higher energies where the continuum absorption drops (Davis et al. 2005). This imprints atomic features on the continuum spectra from each radius, and the strength of these is set by radiative transfer through the vertical structure of the photosphere. These features are included in the BHSPEC model by Davis et al. (2005), currently the best physical model for sub-Eddington thin accretion discs, as introduced in previous chapters of this thesis. Rather than assuming a multi-temperature blackbody spectrum, it uses radiative transfer to calculate the full spectrum through the vertical structure of the disc at each annuli. This is then convolved with special and general relativistic transfer functions to form the best physical disc model currently available (Davis et al. 2005). The disc minimum radius is set by the last stable orbit, thus these disc spectra contain both a key prediction of general relativity and a diagnostic of black hole spin.

While single snapshot spectra can be used to measure the innermost radius, a set of monitoring data gives a more reliable estimate, as these show that this size scale remains constant despite significant (more than a factor of 10) changes in luminosity over decades of observations (Kubota et al. 2001; Steiner et al. 2010). The best known source for this is the black hole binary LMC X–3, a high mass X-ray binary in the Large Magellanic Cloud (LMC). Decades of X-ray observations have established it as a persistent but variable source. It spends most of its time in the high/soft state, but also goes through state transitions into the low/hard state (Wilms et al. 2001). Optical observations have unveiled an orbital period of 1.7 days and a mass function of $2.3\pm0.3M_{\odot}$ (Cowley et al. 1983). Although dynamically a canonical black hole, what makes LMC X–3 so unique for detailed spectroscopy is its absorption column density, which is an order of magnitude lower than any known Galactic black hole binary, with $N_H = 3.8\times10^{20}$ cm^{-2} (Page et al. 2003). This, along with its persistence and strong variability, makes it a perfect source in

an effort to constrain the disc models down to the lowest X-ray energies. Its location in the LMC also means the distance is known to better accuracy than to any other black hole binary (D=52 kpc; di Benedetto, 1997), so giving the smallest systematic uncertainties in conversion of flux to luminosity. The black hole mass and orbital inclination are constrained from dynamical measurements to 7–9$M_{\odot}$ (Cowley et al. 1983; Soria et al. 2001) and $50^{\circ} - 67^{\circ}$ (Cowley et al. 1983) respectively. Converting the disc inner radius into gravitational radii within these parameter ranges gives $\sim$4.5–6R_g (Kubota et al. 2010), which means less than a factor of 2 uncertainty in the black hole inner radius, and a spin of a_*=0–0.7 (Kubota et al. 2010).

In Chapter 3 we discussed some uncertainties in the BHSPEC model when using extremely high count rate data. The problems that arise from using the non-standard burst mode, however, combined with the very poorly determined binary parameters of GX 339−4, made it very difficult to constrain the disc at low energies for detailed accretion disc analysis, let alone measure the black hole spin. By taking advantage of the very low absorption column of LMC X–3, and using the less-extreme timing mode of *XMM-Newton* EPIC-pn, we now aim to carefully test these models against arguably the best X-ray data available.

5.1.1 LMC X–3 Observations

Despite all the advantages mentioned above, there is very little archival CCD data of LMC X–3 available. *XMM-Newton* had previously observed LMC X–3 on 12 occasions, listed in Wu et al. (2001), but as 11 of these were taken in standard photon counting modes, they suffer from major pileup and thus cannot be used for detailed spectral fitting (e.g. Done & Diaz Trigo 2010). The single timing mode observation was fortuitously taken near the peak luminosity ($\sim 0.4L/L_{Edd}$), showing the brightest disc spectrum to date for LMC X–3 (Obs 1. in Table 5.1; Figure 5.1, in black).

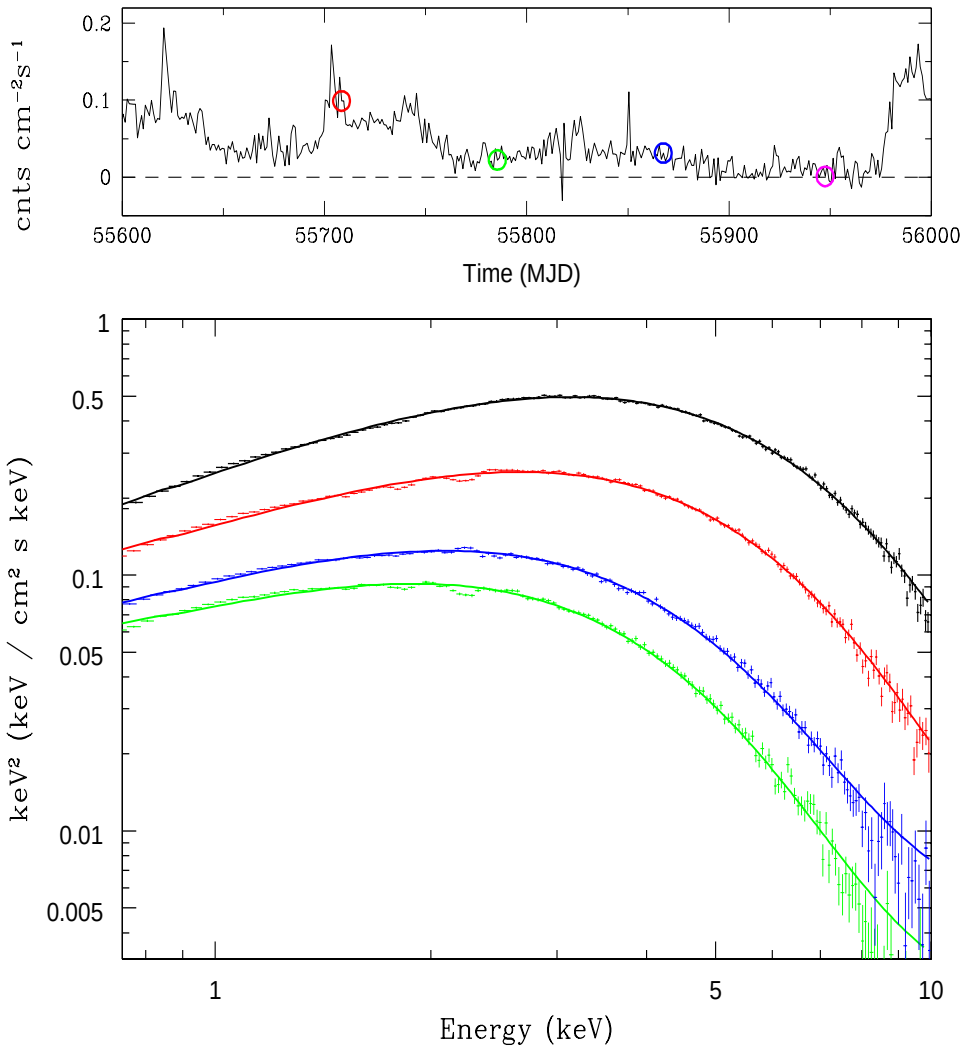

Figure 5.1: *Top panel*: A long term MAXI lightcurve of LMC X–3, with the AO-10 observations marked with colours corresponding to the unfolded spectra in the bottom panel. Observation 5 is marked in magenta, but is not included in the analysis due to extremely low count rate. *Bottom panel*: The unfolded spectra of the observations discussed in this chapter, modelled with an absorbed SIMPL⊗BHSPEC model. The 2000 archival observation (Obs 1) is plotted in black, with Obs 2 plotted in red, Obs 3 in green and Obs 4 in blue. The dips between 1.7–2.4 keV in Obs 2 & 3 are due to instrumental edges present in the data *after* the EPFAST correction, whereas Obs 4 seems to be less affected and Obs 1 almost free of instrumental residuals.

	Obsid	Date	cts/s	Exposure (s)
Obs 1	0109090101	2000-11-24 22:26:27	525.8 ± 0.5	9184
Obs 2	0671420301	2011-05-27 02:30:51	279.2 ± 0.3	11480
Obs 3	0671420401	2011-08-12 14:06:30	133.1 ± 0.2	10510
Obs 4	0671420501	2011-11-02 06:49:08	167.4 ± 0.2	10510
Obs 5	0671420601	2012-01-21 06:36:13	0.33 ± 0.01	10390
Obs 6	96113-01-88-00	2011-11-02 07:26:16	14.4 ± 0.2	1888

Table 5.1: Details of the observations analysed in this paper. Obs. 1 is currently the only archival XMM-Newton timing mode observation, and also the brightest. The source virtually switched off shortly before Observation 5 was taken, making it too faint for detailed spectral analysis. Obs. 5 was thus excluded from this analysis. Obs. 6 is the only PCA observation included in this analysis, simultaneous with Obs. 4.

The XMM-Newton AO-10 monitoring campaign

We successfully proposed to monitor LMC X–3 during the XMM-Newton AO-10 cycle, to obtain excellent quality data, covering as much as possible of the disc emission at different luminosities. We intend to use these observations to sensitively search for the expected smeared atomic features predicted from the intrinsic photospheric emission in the best theoretical disc models, and use them to test our understanding of the disc vertical structure. Our monitoring campaign consisted of 4 timing mode EPIC pn observations of LMC X–3, plus a single 5 ksec offset exposure in order to constrain the timing mode background towards the source. The on-source pointings were all $\sim$10 ksec long, taken between May 2011 and January 2012, and spaced roughly 80$\pm$10 days apart. In addition to these we include the single archival *XMM-Newton* timing mode observation available in our analysis. The details of all the observations are listed in Table 5.1.

Observations 2–4 successfully cover a range of luminosities in the disc dominated state (0.07–0.2L/L_{Edd}), all clearly fainter than the brightest Obs 1. Shortly before Obs 5, however, the source went through a state transition and entered into an extremely faint low/hard state. The source 2–10 keV flux upper limit of $1.7 \times 10^{-15} ergs\ cm^2 s^{-1}$ corresponds to a bolometric luminosity of $< 5.4 \times 10^{32} erg\ s^{-1}$. This is the lowest upper limit luminosity for LMC X-3 ever detected, showing that the source does have episodes of disc instability quiescence.

At the time Swift monitoring was already instigated for a separate AO-11 observing campaign, and we were able to follow the flux evolution as the source started getting brighter (Figure 5.2). Interestingly, the source seemed to undergo a very strong outburst during this time, going from the lowest ever detected luminosity to the highest in ∼30 days. We are currently exploring the implications of disc instability models in regards to this event, led by Graham Wynn at University of Leicester (Wynn, Kolehmainen et al., in prep). However, as Obs. 5 is only an upper limit, it had to be excluded from this analysis.

5.2 Data reduction and calibration status

The data were reduced using *XMM-Newton* Science Analysis System (SAS) v10.0. All the observations were taken in EPIC-pn timing mode and have count rates comfortably below the nominal pileup limit of 800 cts/s (see Table 5.1). We extracted the source spectra in 5 columns on both sides of the central column in RAWX and the full RAWY. Response and ancillary files were generated using RMFGEN and ARFGEN, respectively. Finally, the spectra were rebinned using the SAS task SPECGROUP, with a minimum of 25 counts/bin and an oversampling factor of 3 as recommended for all EPIC detectors.

The latest calibration status of the EPIC detectors has been discussed in great detail in the previous chapters of this thesis, with two main issues remaining at the

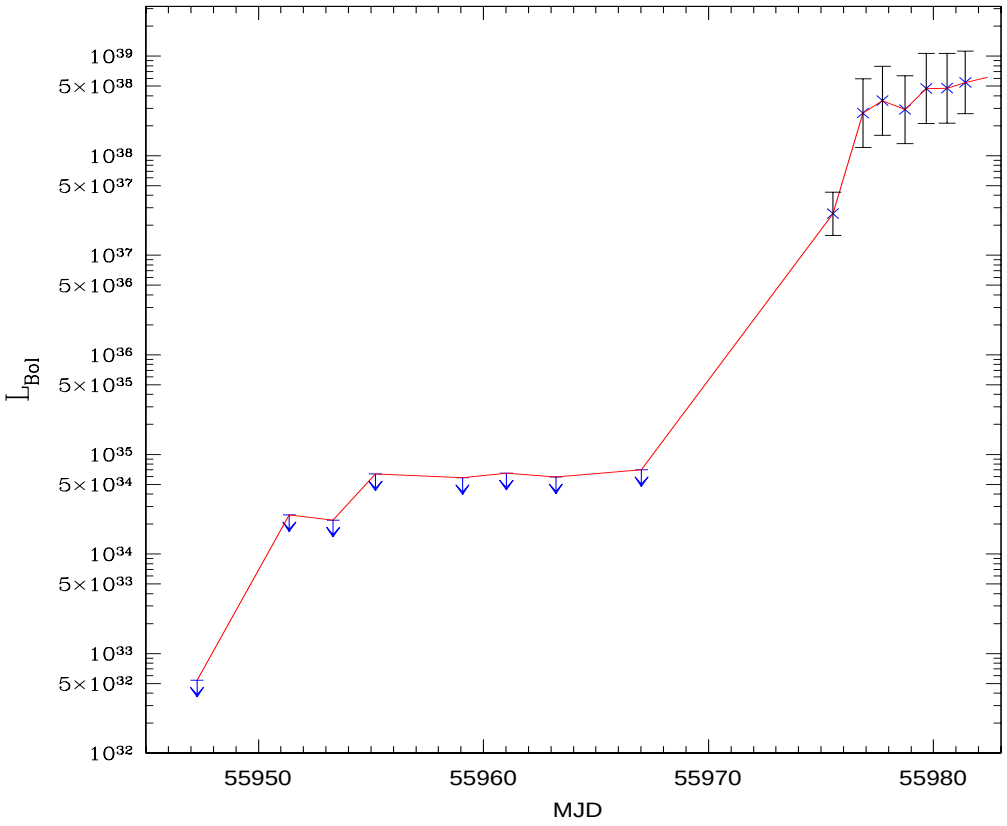

Figure 5.2: The luminosity evolution of LMC X–3 during the extremely faint low/hard state in January 2012. The lowest upper limit for the luminosity was observed with *XMM-Newton*'s EPIC-pn, after which we initiated a *Swift* monitoring campaign to obtain ∼1 ksec snapshot exposures every 2–3 days in order to determine the flux. LMC X–3 seemed to go through a violent outburst during this campaign, going from the lowest ever detected flux to the highest in ∼30 days. The 8-day gap in the observations is due to the source being in the satellite orbital pole and hence unobservable during the fast rising phase.

time of writing. The major problem with the current calibration is the universal effect of X-ray loading (XRL), that arises from the way the underlying electron current in each pixel is determined from offset-map exposures at the beginning of each observation. For bright sources, such as black hole binaries, this current is effectively contaminated by the source itself, resulting in a constant offset in the gain. This issue is further complicated by the automatic subtraction of the exposure map from the data on-board the satellite, making it virtually impossible to reconstruct the original photon energies on ground. XRL has now been understood to affect all *XMM-Newton* fast modes, and thus solving it is the first step in the calibration process. It is currently under vigorous investigation, and a completely new calibration for the XMM-Newton fast timing modes is expected towards the end of 2012, including a solution to the XRL problem.

The second question of whether or not to use the SAS task EPFAST to correct for the rate-dependent charge transfer inefficiency (CTI) is currently dividing opinions within the community. In all simplicity, EPFAST adds a multiplicative correction factor to counteract the small shifts to the energy scale caused by trapped electrons. This factor is applied to the full energy scale such that $E_{corrected} = E_{original}/G_{corr}$, where $E_{original}$ and $E_{corrected}$ are the original and corrected energies and G_{corr} is the correction factor (CAL-TN-0083[1]). This does not, however, change the fact that the data have already been affected by the energy-independent XRL, which adds an energy-independent additive shift to the full energy scale. Furthermore, G_{corr} was originally calibrated for the instrumental edges in the 1.5–3 keV energy range, and outside of this range the calibration is most likely incorrect (CAL-TN-0083). In fact, Walton et al. (2012) showed that not applying the EPFAST correction led to a more accurate energy reconstruction around the Fe line region in a burst mode observation. However, this can at least partly be explained by their relatively low

[1]http://xmm.vilspa.esa.es/external/xmm_sw_cal/calib/documentation.shtml

count rate, hard intermediate state observation, as the task was originally designed for high count rates and yields more scatter at rates below ∼250 cts/s. That said, EPFAST is currently the best way available to correct for the rate-dependent effects in the *XMM-Newton* data, and recommended by the satellite calibration team, which is why we chose to run EPFAST on all of the timing mode event files analysed here.

As the EPIC-pn is calibrated only up to 10 keV, constraining the hard tail is impossible without higher energy data. Sadly, the late *RXTE* satellite was taking its last breath at the time of our monitoring campaign, and in the end we only managed to obtain simultaneous PCA data for one of our observations, Obs 4. This PCA spectrum was extracted using the *RXTE* standard products pipeline.

5.3 Modelling the disc dominated spectra

In Chapter 3 we showed that real accretion disc spectra seem to be broader than the BHSPEC model allows. Furthermore, the model includes atomic absorption edges from oxygen and iron L between 0.7–1.2 keV. Even though these edges are relativistically broadened and smeared, they still appear stronger in the model than in the actual data (Kubota et al. 2010; Kolehmainen, Done & Diaz Trigo 2011). These residuals are only at the 5–10 % level, but are made significant by the quality of data available.

Following the analysis of the LMC X–3 system parameters in Kubota et al. (2010), we fix the black hole mass at $9M_{\odot}$, the inclination at 50° and distance to the source at 52 kpc. This combination of parameters will give us an upper limit for a_*, and thus we let the spin parameter vary freely. However, while LMC X–3 offers an unprecedented view of the accretion disc at low energies, the lack of high energy data makes modelling the continuum very difficult. We first focus on Obs.1 as it seems to have the fewest instrumental features in Figure 5.1.

	Models
Model 1	BHSPEC
Model 2	SIMPL $\otimes$ BHSPEC
Model 3	SIMPL $\otimes$ BHSPEC ($\Gamma = 2.2$)
Model 4	SIMPL $\otimes$(DISKBB+COMPTT)
Model 5	SIMPL $\otimes$(DISKBB+COMPTT)+reflection
Model 6	(SIMPL $\otimes$ BHSPEC)+reflection

Table 5.2: The spectral models used in this analysis. All models are absorbed with TBABS, with N_H fixed at $3.8{\times}10^{20}$ cm^{-2}. Reflection is modelled with KDBLUR$\times$RFXCONV$\times$(SIMPL$\otimes$BHSPEC).

5.3.1 The brightest observation: Obs. 1

We go through a selection of theoretically and observationally motivated spectral models in an effort to find a model that describes the spectra best, all listed in Table 5.2. We start our analysis by fitting the disc with an absorbed BHSPEC, Model 1 in Table 5.2. As the spectrum looks like a clear disc, modelling it with a physical disc model should result in an acceptable fit. However, this yields a very poor best-fit of $\chi^2_\nu = 556/165$, with a high spin of $a_* = 0.84 \pm 0.001$ at $0.42L/L_{Edd}$. The model residuals also show major fluctuations below 3 keV(Figure 5.3).

Adding a power law component by convolving the disc with the modified SIMPL model, as outlined in Kolehmainen et al. (2011), gives statistically a slightly better fit with $\chi^2_\nu = 364/163$, but with *plainly* unphysical model parameters. The spin is slightly lower this time ($a_* = 0.75{\pm}0.01$), but the photon index turns extremely steep, as $\Gamma = 9.80^{+0.31}_{-0.86}$ and the fraction of upscattered photons hits unity ($f_{scat} = 1_{-0.02}$ (Figure 5.3). This is most likely caused by the real disc being broader than BHSPEC, and since the data cannot constrain the hard tail, SIMPL has the freedom to use the

'hard tail' as a soft component for the disc. Since most of the signal-to-noise is at low energies, the discrepancies between the data and the model below 2 keV seem to drive the fit, which leads to these residuals at low energies being compensated by a steep tail.

Seeing as the model is not able to constrain the tail without higher energy data, we fix the spectral index at a typical value of Γ=2.2, as is usually seen in the high/soft state. Thus Model 3 allows us to find a fit that describes the hard tail well above 7 keV, giving $\chi^2_\nu = 555/164$ (Figure 5.3). The fraction of upscattered photons is now much more reasonable, constrained between 0–3%, meaning that the tail is not actually significant in these data. Since the model does not have the freedom here to make the disc broader, it is forced to follow the BHSPEC model. Therefore the derived spin is determined from the system parameters and thus gives the same spin as BHSPEC alone.

In Chapter 3 we circumvented these issues by replacing the more physical BHSPEC model with a phenomenological DISKBB+COMPTT combination, which resulted in a better fit to the data at low energies while still maintaining the broad disc shape. Model 4 gives $\chi^2_\nu = 286/160$, with a very cool disc ($T_{in} = 0.39 \pm 0.04$) and a steep power law ($\Gamma = 5.54^{+0.18}_{-0.17}$). The fraction of upscattered photons is again close to unity ($f_{scat} = 0.99^{+0.01}_{-0.18}$) due to the strong coupling of these two parameters. Adding smeared reflection of the Comptonised continuum (Model 5), as was used in Kolehmainen et al. (2011), gives a statistically better fit with $\chi^2_\nu = 211/157$, but the tail is unphysically steep again at $\Gamma = 3.8^{+0.8}_{-0.6}$ (Figure 5.4).

The features below 2 keV in both of these models look similar to the ones seen previously for EPIC-pn data of GX 339−4 in Kolehmainen et al. 2011, and seem to confirm our results in Chapter 3. A comparison of Models 2 and 4 is plotted in Figure 5.5, showing clearly the discrepancies between the data and the physical model.

The fact that Obs. 1, the brightest of our observations, shows the clearest disc

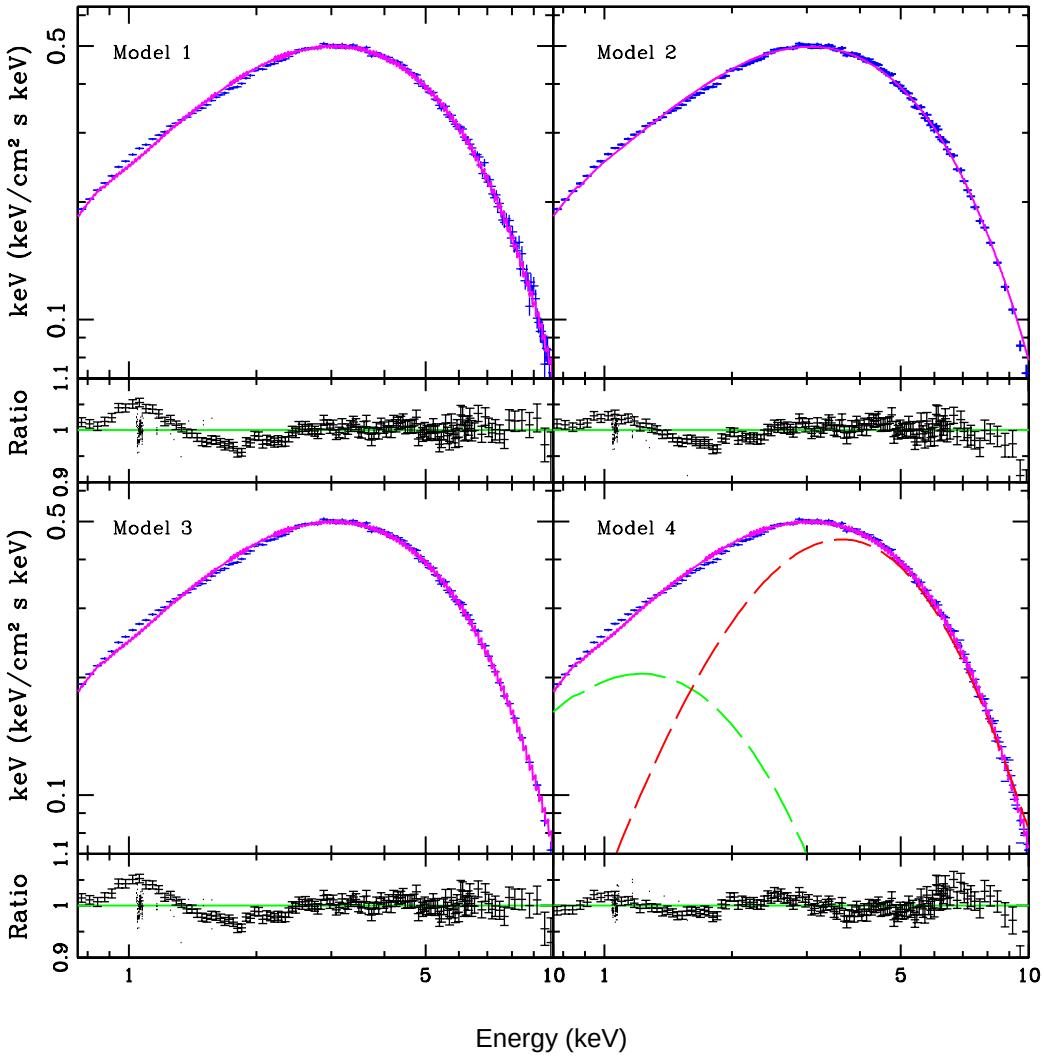

Figure 5.3: Obs. 1 modelled with Models 1–4. The data are better fitted by the phenomenological Model 4 at low energies than the more physical models 1–3, which is also seen in the case of Galactic black hole binary GX 339−4 (Kolehmainen et al. 2011).

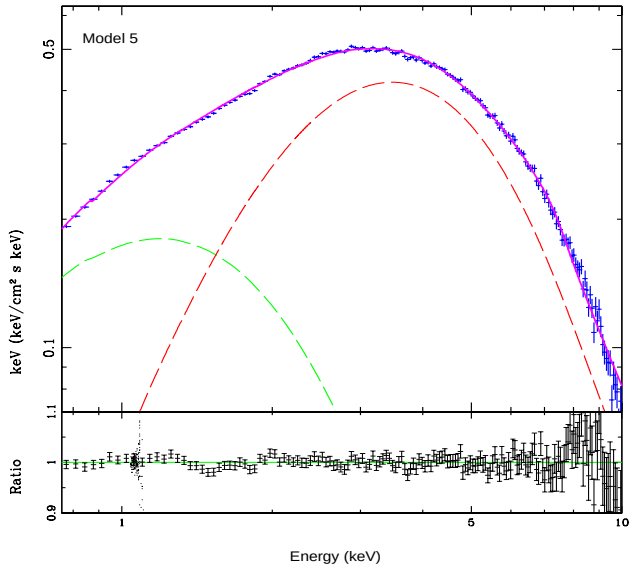

Figure 5.4: Obs. 1 modelled with a phenomenological DISKBB+COMPTT+ REFLECTION model, following Kolehmainen et al. (2011). The DISKBB component is plotted in green and COMPTT in red. The data are best fit by this phenomenological Model 5 out all of the models considered here.

shape and seems to follow the BHSPEC model the closest above ∼2 keV and around the peak of the spectrum (Figure 5.5), but then fails to produce a physical fit, suggests that real disc spectra are actually more complex than BHSPEC. This might be at least partly due to the model struggling to constrain the hard tail with only the EPIC-pn data, and hence we employ the only available simultaneous *RXTE* PCA dataset.

5.3.2 Joint EPIC-pn/PCA fits: Obs. 4

We combine the only available PCA observation together with Obs. 4 in an effort to constrain the hard tail. Surprisingly, fitting the simultaneous EPIC-pn and PCA data together does not help the fit at all. The cross-calibration issues between the EPIC-

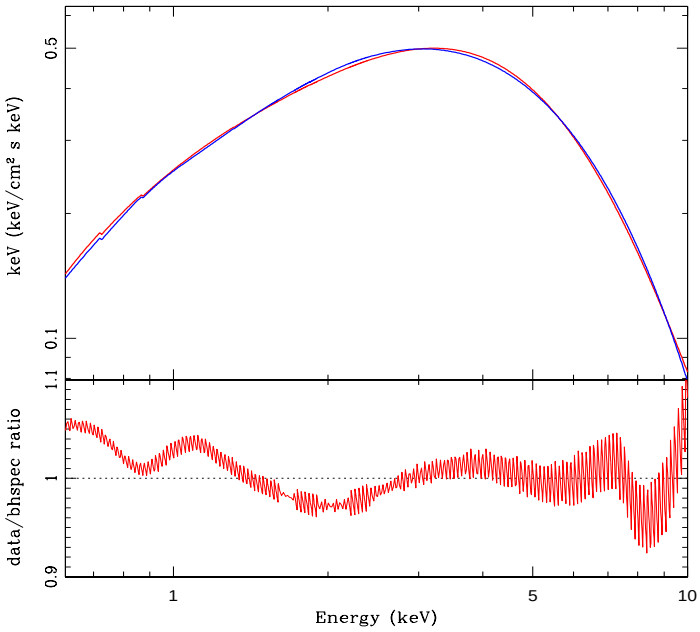

Figure 5.5: Comparison between the more physical SIMPL⊗BHSPEC model (Model 2, in blue) and the phenomenological SIMPL⊗(DISKBB+COMPTT) model (Model 4, in red) for Obs. 1, showing clearly the discrepancies between the data and the physical model.

pn and the PCA, previously noted in Chapters 3 & 4, are also present here. There is a clear mismatch above 4 keV between the two datasets, with the PCA requiring a steeper spectral index than the pn. In addition, the short, less than 2 ksec, snapshot PCA observation has too poor signal-to-noise to provide extra constraints on the high energy tail (Figure 5.6).

Model 2 yields poorer fit than for Obs 1, $\chi^2_\nu = 323/191$ with similarly steep tail and a scattering fraction of unity (Figure 5.6). Adding smeared reflection to Model 2 gives a better fit with $\chi^2_\nu = 266/199$, statistically slightly more acceptable than with EPIC-pn only, but once again with the same unphysical continuum parameters (Model 6). Reflection is more reasonable with $\Omega/2\pi$=$0.17^{+0.03}_{-0.10}$ and ionisation state

of $\xi = 3.38^{+0.27}_{-0.25}$. The spin is measured at $a_* = 0.70^{+0.04}_{-0.03}$, which is also the upper limit expected from our chosen system parameters, and the same as in Kubota et al. (2010).

The phenomenological model (Model 5) yields a much better fit this time, however, with $\chi^2_\nu = 190/178$ and with much more believable parameters (Figure 5.6, lower left panel). The continuum is still relatively steep ($\Gamma = 3.26^{+0.03}_{-0.02}$), but the scattered fraction is reasonable at $f_{scat} = 0.06 \pm +0.001$, and a disc inner radius, as measured from reflection, is at $R_{in} = 14^{+11}_{-6}$. The reflection component is quite high at ($\Omega/2\pi$=$0.70^{+0.05}_{-0.10}$) and the disc is extremely ionised at $\xi = 4.00_{-0.12}$. This is similar to what we saw in the high mass accretion rate spectra of GX 339−4 in Chapter 3, but surprisingly different to the Suzaku residuals of LMC X–3 in Kubota et al. (2010, Figure 5.8), despite having similar luminosities. A comparison of Models 5 and 6 is shown in Figure 5.7, with noticeable deviations between the data and the physical model.

This analysis has shown explicitly, how, on one hand, the lack of higher energy data means that EPIC-pn alone cannot constrain the continuum above ∼7 keV. On the other hand, the quality of these data is high enough to confirm the 5–10% discrepancy between the data and the best physical model seen in Chapter 3. All that said, however, the fact that the BHSPEC model fits the data better in the higher luminosity observation than the lower luminosity one is intriguing. It raises the question of whether the effect of advection could explain this difference above luminosities $\sim 0.3L/L_{Edd}$, where the limitations to the standard thin disc model mean it cannot radiate all the energy that is dissipated by the viscous stresses, and as a result puffs up. However, Straub et al. (2012) showed by using a slim disc model that advection makes very little change to the spectrum at luminosities $L < L_{Edd}$. Thus advection alone is unlikely to be the cause for the discrepancy at moderate luminosities. These issues are discussed more in Section 5.5.2 below.

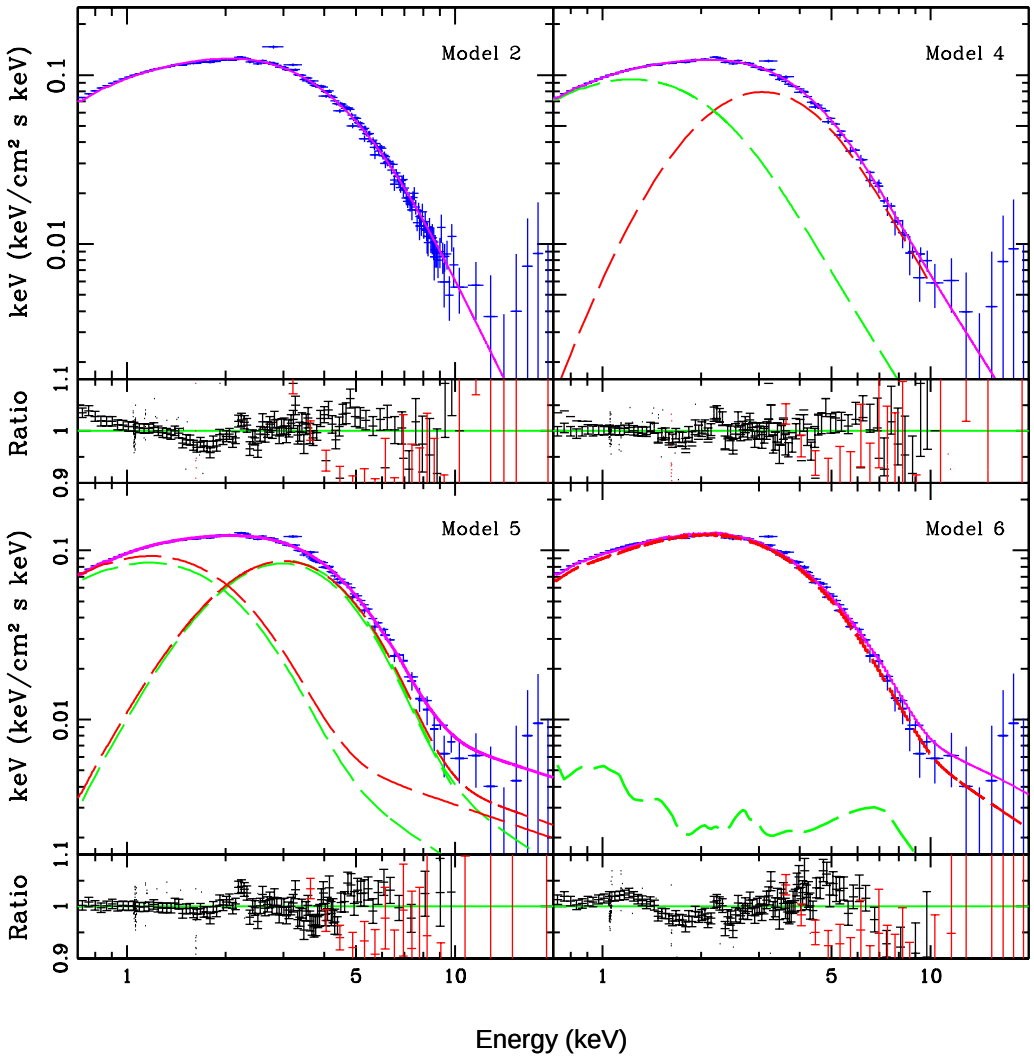

Figure 5.6: Obs. 4, combined with the PCA data, modelled with Models 2, 4, 5, 6. The PCA data points cannot constrain the continuum above 10 keV, and the issues with cross-calibration are clear from the data-to-model ratios in the lower panels.

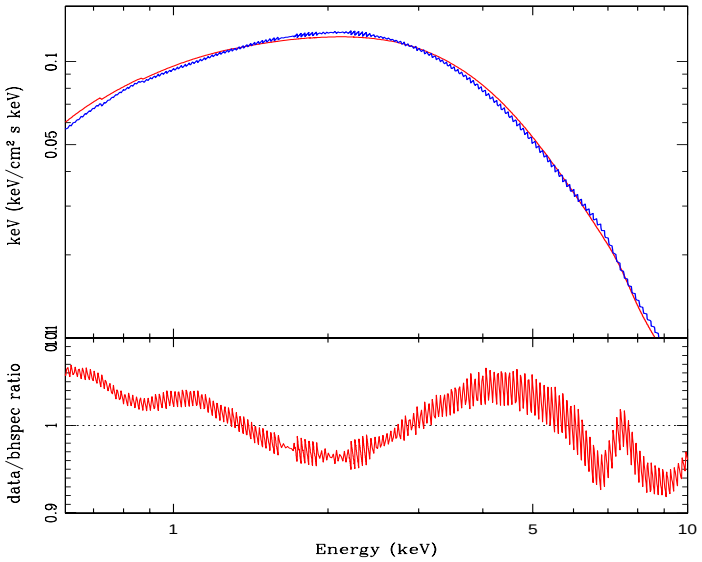

Figure 5.7: Comparison between the phenomenological Model 5 (in red) and Model 6 (in blue) for Obs. 4, showing clearly the discrepancies between the data and the more physical model.

5.3.3 Observations 2 & 3

Observations 2 and 3 are strongly affected by the instrumental Si and Au edges between 1.7–2.4 keV (see Figure 5.1). As the model tries to predominantly fit for the lower energies at the expense of the tail, this yields an over-estimation of the model at high energies above ∼7 keV in the EPIC-pn. Therefore, instead of detailed spectral analysis of these data, we focus on analysis of the data–model discrepancies in Section 5.4.

5.4 Quantifying deviations from the model

Since it is difficult to reliably constrain the continuum with the EPIC-pn data alone, we instead focus on quantifying the deviations from the BHSPEC model in these

data. The low energies possess most of the signal-to-noise in the EPIC-pn, and hence the small features below 2 keV cause the model to over-estimate the tail at higher energies (Figures 5.5 and 5.7). To compare these differences between the observations, we use an absorbed BHSPEC, with smeared reflection, and search for a fit that describes the data above 7 keV. Starting with the observation that is best fit by the model, Obs. 1, we fix the tail at a typical value of Γ=2.2, usually seen in the high/soft state, and freeze the reflection fraction at unity. We then manipulate the normalisation of the SIMPLE model, characterised by the fraction of up-scattered photons from the disc, by forcing the model to follow the data above the desired 7 keV. This scattering fraction is then fixed before fitting the model. The data-to-model ratios are plotted in Figure 5.8. The bottom two panels in Figure 5.8 show the GX 339−4 observation (0410581201) analysed in Chapter 3 (magenta), and the Suzaku observation of LMC X–3 analysed in Kubota et al. (2010) for comparison.

Figure 5.8 shows the observations 1–4 in order of decreasing luminosity, with the same colour convention as in Figure 5.1. All *XMM-Newton* LMC X–3 observations show an excess around ∼1 keV, similar to what was previously seen in the high mass accretion rate spectra in Chapter 3, plotted in Figure 5.8 for comparison. This bump around 1 keV has the same shape as seen in the low/hard state GX 339−4 spectra in Figure 5.3 in Chapter 4. We took this feature as an indication of a clumpy inner disc in the low/hard state, and a possible origin for the disc variability seen in Uttley et al. 2011. This is not the case here, however, as these data are clearly dominated by the disc emission. Thus the most likely explanation is again the model having stronger absorption features than the data actually show. However, the fainter observations 2–4 show much broader deviations below ∼1.5 keV, caused by the disc being too narrow to reach the data at low energies. Noticeably, the *Suzaku* observation at the bottom panel in Figure 5.8 shows a ∼2% dip at these energies instead of an excess. This could be an indication that the low energy feature in all of the EPIC-pn data is at least partly instrumental, and also probably indicates a cross-calibrational issue

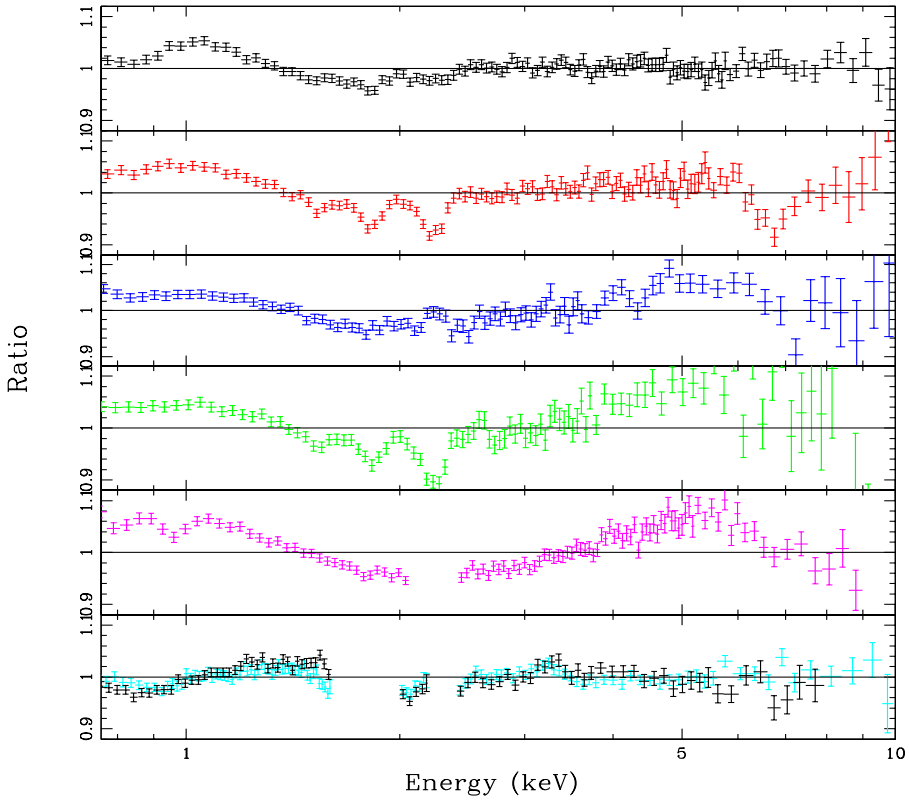

Figure 5.8: The data/model ratios of all of our observations, modelled with BHSPEC plus reflected continuum as described in the text. The photon index was fixed to 2.2 as expected for disc dominated high/soft state spectra and the reflection fraction was set to unity. The fraction of up-scattered photons was used to constrain the data above 7 keV before fitting the data. This gives a way to quantify the deviations from the model at low energies. The colour convention is the same as in Figure 5.1, with the addition of the GX 339−4 observation 0410581201 analysed in Chapter 3 (in magenta), and the *Suzaku* observation of LMC X–3 analysed in Kubota et al. (2010).

between *XMM-Newton* and *Suzaku* at these small 5–10% levels.

Obs. 1 in the top panel (in black) follows the model well above ∼2.4 keV, with only slight features remaining between 1.7–2.4 keV after the CTI correction. This could be due to the expected time dependence of the CTI, as the number of electron 'traps' is likely to increase with time. Time dependence does not explain the similarly low level of residuals in the newest observation (Obs. 4), however. This is more likely due to the CTI correction task EPFAST being subject to more scatter at count rates below ∼250 cts/s. These strong edges have been ignored in the GX 339−4 and the *Suzaku* observations as described in Chapter 3 and in Kubota et al. (2010), respectively.

Another notable feature is the 'hump' around 5 keV, that seems to strengthen with decreasing luminosity. This feature is nearly at the 10 % level in Obs. 3, at 5 % in Obs. 4, and at the 2% level in Obs. 2. It is also a ∼10 % feature in the GX 339−4 spectrum. Observation 1, on the other hand, follows the model closely at these energies, showing no deviations above ∼2 keV, similar to both of the *Suzaku* XIS spectra. A more interesting feature, however, is the dip at ∼6.9 keV in observations 2–4. This dip is at the right energies to be an absorption edge from hydrogen-like iron, and as such an indication of a disc wind. Winds are generally seen in sources with a high inclination angle (Ponti et al. 2012), which, if this is indeed a signature of a disc wind, would suggest that the inclination is higher than the 50° used here. In fact, recent studies suggest that the inclination is most likely between 65° and 67° (J. Steiner, private communication).

5.5 Discussion and conclusions

Our analysis of the best quality data available, modelled with the best physical models available, only confirms our results from Chapter 3. The lower luminosity data are best described by a phenomenological two-component disc, that allows it

to be broader than the more physical BHSPEC model. Using a phenomenological model in conjunction with higher energy data also gets rid of the absorption features present in BHSPEC and stops the fits being driven by these strong features at low energies. This implies that some physics are still missing from our best current disc models.

5.5.1 Black hole spin

Even though the spin is a free parameter in the model, it is tightly bound to the system parameters. The values quoted in this paper are by no means meant to be taken as exact spin estimates, but rather show the dependence on the continuum shape. Kubota et al. (2010) have previously constrained the spin between 0–0.7 within the system parameters. This seemingly large range actually corresponds to a change in inner radius of less than a factor of two. They suggested that the BHSPEC model is not sensitive to low to moderate spins, but we note that this depends on how well the disc is constrained. Fitting our brightest observation (Obs. 1) with an absorbed BHSPEC gave $a_* = 0.84 \pm 0.01$, which is significantly higher than the upper limit from Kubota et al. (2010). The high spin derived here is most likely due to the physical model being too narrow to fit the broad disc, as seen in Figure 5.5. If the inclination is in fact higher, as suggested by the presence of wind features, then the spin will be lower. Thus it seems most likely that the spin in LMC X–3 is moderate, rather than extreme, which is also in keeping with previous studies of Galactic black hole binaries (Yamada et al. 2009; Kolehmainen & Done, 2010; Steiner et al. 2010).

Considering that LMC X–3 is one of the best-constrained black hole binaries, this demonstrates the need for better limits on system parameters, along with further improvements in the physical disc models for direct fitting for the spin parameter.

5.5.2 Improvements to the current disc models

We have confirmed our results in Chapter 3, showing that real accretion disc spectra seem to be broader than the BHSPEC model allows. A further deviation is caused by atomic absorption edges from oxygen and iron L between 0.7–1.2 keV that seem to be present in the model but not in the data. One solution to reduce these atomic features could be to apply sub-solar abundances, which would be consistent with the LMC previously being suggested to have sub-solar abundances by e.g. Russell & Bessell (1989) and Korn et al. (2002). Kubota et al. (2010), however, showed that the discrepancies in the model cannot be explained by this alone. Instead they proposed including more atomic physics into the model, since self-irradiation of the disc, driving the photosphere towards isothermality, could provide a way to reduce the absorption features in the model while still maintaining the broad disc shape.

The brightest observation (Obs. 1) at $\sim 0.4L/L_{Edd}$ is best fit by the BHSPEC model out of our sample data. The fact that deviations seem to increase as the luminosity decreases could suggest a significant change in the accretion flow, namely advection becoming significant above $\sim 0.3L/L_{Edd}$. But the trend in luminosity seen here goes the wrong way. More deviations are expected at higher luminosities as advection becomes more important, but instead the data show smaller deviations from the model. This was previously investigated by Straub et al. (2012), who explored the effects of advection by using a slim disc model on both low and high luminosity disc spectra of the ultra-luminous X-ray source in M31. Based on their study, however, they concluded that advection makes very little difference to spectra well below the Eddington luminosity. Instead they speculate that the observed spectral broadening could be a characteristic of magnetic pressure support in the disc. This would increase the scale hight of the disc, decreasing its density and absorption opacity and making the spectrum broader as electron scattering becomes more important (Davis et al. 2009). However, there are issues with how this pressure scales with

gas pressure and radiation pressure, and thus more numerical simulations are needed (Straub et al. 2012).

Chapter 6 | *Concluding remarks*

The previous chapters have striven to understand and carefully model the time-averaged energy spectra from several Galactic black hole binaries, in order to ultimately measure the black hole spin. Achieving this has required in-depth understanding of the instruments as well as the data analysis methods. The spin leaves only minor traces in the data, and these can be affected by calibration uncertainties, uncertainties in the models and systematic uncertainties. This knowledge is absolutely essential for a detailed analysis of all relativistically smeared atomic features seen in the time-averaged energy spectra of compact objects.

Resolving the spin controversy in X-ray binaries is crucial in expanding the knowledge to supermassive black holes. Since Galactic black hole binaries are too bright to be observed with the standard, well calibrated imaging modes, we are instead forced to use special, fast timing modes. During the course of this thesis, it has become increasingly apparent that the current calibration of these timing and burst modes is not at the level where this can be reliably achieved. I have been collaborating with the *XMM-Newton* calibration team at the European Space Agency's (ESA) European Space Astronomy Centre (ESAC), and have acquired an extensive knowledge of the calibration and instrumental effects in the *XMM-Newton* satellite that affect the resulting spectra. The work in this thesis has had a major impact in the active calibration effort by the *XMM-Newton* calibration team, and has led to issues with the EPIC-pn response being addressed. A new release of the timing and burst mode responses has now been released for the Science Analysis System (SAS) version 12.0, but was announced too late to be included in this thesis. However, this does not fix the underlying issue of X-ray loading, and seeing as correcting for it is the *first* step

in the calibration process, any additional data augmentation efforts may seem irrelevant at this time. A completely new calibration for the *XMM-Newton* fast timing modes is expected to be announced towards the end of 2012, including a solution for the XRL.

Despite of these issues with the fast mode calibration, the quality of the current X-ray data is actually high enough to show the weaknesses in the current spectral models. This thesis has demonstrated how the currently best physical accretion disc models do not describe the data to better than 5–10% level, with absorption features in the model that do not seem to be present in the data (Kolehmainen et al. 2011). Illustrating this in detail is of course an important result, and hopefully a step forward in motivating the development of new theoretical models. This is essential in the effort to increase the confidence in spin measurements, for both the continuum fitting and the iron Kα line method.

As for the black hole spin, some of the controversy still exists. We have managed to resolve some of the disagreement in spin measurements in the specific case of the Galactic black hole binary GX 339−4 by careful modelling of the continuum. We showed that most low/hard state spectra do not require relativistically broadened line profiles, unlike widely claimed in literature, and thus the iron line method can produce spin values that are consistent with upper limits derived from the continuum fitting method. The few strong candidates (e.g. GX4 in Chapter 4) for a broad line profile observation have complex continuum spectra, and the reflection is strongly ionised, with modelling issues becoming apparent. Hence the effort to derive actual, consistent spin estimates from the two current methods is challenging. The iron line profile is strongly dependent on the continuum model used, and as a $\sim$5% feature it is vulnerable to calibration uncertainties of the same level. However, even though the continuum fitting method is widely accepted as the more robust method to determine the black hole spin, the biggest challenge for *reliable* spin measurements comes from the strong parameter dependence of this method. Seeing as this relatively robust

method already exists, the solution lies in dynamical studies. Better dynamical constraints on the system parameters are needed for all of the known black hole binaries. Currently one of the best sources for this, the black hole binary LMC X-3, with a distance measured at 52 kpc (di Benedetto 1997), black hole mass between $7 - 9M_{\odot}$ and an inclination of 50°–67°, can at best constrain the spin between $a_* = 0 - 0.7$ within the limits of the system parameters (Kubota et al. 2010). The development of new techniques and instruments will hopefully also shed new light into the black hole spin in the near future.

6.1 The way forward

Time-averaged energy spectra alone are not enough to resolve the controversy over the accretion geometry and causality. A change in the accretion geometry gives rise to the observed spectral variability on time scales >100 seconds. In general, time-averaged energy spectra give us information of the accretion properties in the form of different emission components, but say nothing about the way these different spectral components, such as the accretion disc blackbody and the high energy continuum power law, vary with respect to each other in time. By looking at the absolute amplitude of variations in count rate as a function of energy, we can construct a variability spectrum, which identifies only the time-varying components. This method is uniquely appealing as it allows us to distinguish complex patterns of spectral variability where components have different time-scales of variation, and determine not only the way the components vary, but also when they vary in relation to each other. This way we can pick out the different emission components and construct a picture of the accretion geometry in a completely new way when joined with long-term energy spectral information. The possible correlation of variance in different energy bands against time will also help us separate intrinsic emission from reprocessed emission, which again is crucial in reconstructing the structure of the

accretion flow.

This line of research has only recently been developed and is still at an early stage. With the wide energy band of X-ray satellites, such as *XMM-Newton*, *NuSTAR* and *Astro-H*, we can model the frequency resolved energy spectrum in the 0.7–200 keV energy range in a way that has not been possible before. This will enable us to map the structure of the emission region around the black hole and reveal the nature of the black hole accretion mechanism.

Bibliography

[1] Arévalo, P., & Uttley, P. 2006, MNRAS, 367, 801

[2] Ballantyne, D. R., Ross, R. R., & Fabian, A. C. 2001, MNRAS, 327, 10

[3] di Benedetto, G. P. 1997, ApJ, 486, 60

[4] Casares, J. 2007, astro-ph/0612312

[5] Chiang, C. Y., Done, C., Still, M., & Godet, O. 2010, MNRAS, 403, 1102

[6] Churazov, E., Gilfanov, M., & Revnivtsev, M. 2001, MNRAS, 321, 759

[7] Cunningham, C. T. 1975, ApJ, 202, 788

[8] Davis, S. W., Blaes, O. M., Hubeny, I., & Turner, N. J. 2005, ApJ, 621, 372

[9] Davis, S. W., Done, C., & Blaes, O. M. 2006, ApJ, 647, 525

[10] Davis, S. W., Blaes, O. M., Hirose, S., & Krolik, J. H. 2009, ApJL, 703, 569

[11] Done, C. 2010, arXiv:1008.2287

[12] Done, C., & Davis, S. W. 2008, ApJ, 683, 389

[13] Done, C., Diaz Trigo, M. 2010, MNRAS, 407, 2287

[14] Done, C., & Gierliński, M. 2003, MNRAS, 342, 1041

[15] Done, C., & Gierliński, M. 2006, MNRAS, 367, 659

[16] Done, C., Gierliński, M., & Kubota, A. 2007, A&ARv, 15, 1

[17] Done, C., & Kubota, A. 2006, MNRAS, 371, 1216

[18] Done, C., & Nayakshin, S. 2007, MNRAS, 377, L59

[19] Dunn, R. J. H., Fender, R. P., Körding, E. G., Cabanac, C., & Belloni, T. 2008, MNRAS, 387, 545

[20] Esin, A. A., McClintock, J. E., & Narayan, R. 1997, ApJ, 489, 865

[21] Fabian, A. C., Rees, M. J., Stella, L., & White, N. E. 1989, MNRAS, 238, 729

[22] Fabian, A. C., Iwasawa, K., Reynolds, C. S., & Young, A. J. 2000, PASP, 112, 1145

[23] Fanidakis, N., Baugh, C. M., Benson, A. J., et al. 2011, MNRAS, 410, 53

[24] Fender, R. P., Gallo, E., & Russell, D. 2010, MNRAS, 406, 1425

[25] Fragos, T., Tremmel, M., Rantsiou, E., & Belczynski, K. 2010, ApJL, 719, L79

[26] Gammie, C. F. and Shapiro, S. L. and McKinney, J. C., 2004, ApJ, 602, 312G

[27] Gierlinski, M., Zdziarski, A. A., Done, C., et al. 1997, MNRAS, 288, 958

[28] Gierliński, M., Zdziarski, A. A., Poutanen, J., Coppi, P. S., Ebisawa, K., & Johnson, W. N. 1999, MNRAS, 309, 496

[29] Gierliński, M., & Done, C. 2004, MNRAS, 347, 885

[30] Gierliński, M., Done, C., & Page, K. 2008, MNRAS, 388, 753

[31] Gierliński, M., Maciołek-Niedźwiecki, A., & Ebisawa, K. 2001, MNRAS, 325, 1253

[32] Gierliński, M., & Newton, J. 2006, MNRAS, 370, 837

[33] Guainazzi, M., Bianchi, S., Matt, G., Dadina, M., Kaastra, J., Malzac, J., & Risaliti, G. 2010, MNRAS, 406, 2013

[34] Hiemstra, B., Soleri, P., Méndez, M., et al. 2009, MNRAS, 394, 2080

[35] Hiemstra, B., Méndez, M., Done, C., et al. 2011, MNRAS, 411, 137

[36] Hynes, R. I., Steeghs, D., Casares, J., Charles, P. A., & O'Brien, K. 2003, ApJ, 583, L95

[37] Hynes, R. I., Steeghs, D., Casares, J., Charles, P. A., & O'Brien, K. 2004, ApJ, 609, 317

[38] Ingram, A., Done, C., & Fragile, P. C. 2009, MNRAS, 397, L101

[39] Ingram, A., & Done, C. 2011, MNRAS, 415, 2323

[40] Ingram, A., & Done, C. 2012, MNRAS, 419, 2369

[41] Kato, S., Fukue, J., & Mineshige, S. 1998, Black-hole accretion disks. Edited by Shoji Kato, Jun Fukue, and Sin Mineshige. Publisher: Kyoto, Japan: Kyoto University Press, 1998. ISBN: 4876980535,

[42] Kawabata, R., & Mineshige, S. 2010, PASJ, 62, 621

[43] King, A. R., Pringle, J. E., & Hofmann, J. A. 2008, MNRAS, 385, 1621

[44] King, A. R., & Kolb, U. 1999, MNRAS, 305, 654

[45] Kirsch, M. G. F., et al. 2006, A&A, 453, 173

[46] Kolehmainen, M., & Done, C. 2010, MNRAS, 406, 2206

[47] Kolehmainen, M., Done, C., & Díaz Trigo, M. 2011, MNRAS, 416, 311

[48] Korn, A. J., Keller, S. C., Kaufer, A., et al. 2002, A&A, 385, 143

[49] Kotov, O., Churazov, E., & Gilfanov, M. 2001, MNRAS, 327, 799

[50] Kubota, A., & Done, C. 2004, MNRAS, 353, 980

[51] Kubota, A., Done, C., Davis, S. W., Dotani, T., Mizuno, T., & Ueda, Y. 2010, ApJ, 714, 860

[52] Kubota, A., Makishima, K., & Ebisawa, K. 2001, ApJ, 560, L147

[53] Laor, A. 1991, ApJ, 376, 90

[54] Li, L.-X., Zimmerman, E. R., Narayan, R., & McClintock, J. E. 2005, ApJS, 157, 335

[55] Madej, O. K., & Jonker, P. G. 2011, MNRAS, 412, L11

[56] Makishima, K., Takahashi, H., Yamada, S., et al. 2008, PASJ, 60, 585

[57] Malzac, J., Beloborodov, A. M., & Poutanen, J. 2001, 326, 417

[58] McClintock, J. E., & Remillard, R. A. 2006, Compact stellar X-ray sources, 157

[59] McClintock, J. E., Shafee, R., Narayan, R., Remillard, R. A., Davis, S. W., & Li, L.-X. 2006, ApJ, 652, 518

[60] Middleton, M., Done, C., Gierliński, M., & Davis, S. W. 2006, MNRAS, 373, 1004

[61] Miller, J. M., et al. 2004a, ApJL, 606, L131

[62] Miller, J. M., et al. 2004b, ApJ, 601, 450

[63] Miller, J. M., Homan, J., Steeghs, D., Rupen, M., Hunstead, R. W., Wijnands, R., Charles, P. A., & Fabian, A. C. 2006, ApJ, 653, 525

[64] Miller, J. M., et al. 2008, ApJ, 679, L113

[65] Miller, J. M., Reynolds, C. S., Fabian, A. C., Miniutti, G., & Gallo, L. C. 2009, ApJ, 697, 900

[66] Miller, L., Turner, T. J., Reeves, J. N., George, I. M., Kraemer, S. B., & Wingert, B. 2007, A&A, 463, 131

[67] Miller, L., Turner, T. J., & Reeves, J. N. 2008, A&A, 483, 437

[68] Mitsuda, K., et al. 1984, PASJ, 36, 741

[69] Miyamoto, S., Kitamoto, S., Mitsuda, K., & Dotani, T. 1988, Natur, 336, 450

[70] Muñoz-Darias, T., Casares, J., & Martínez-Pais, I. G. 2008, MNRAS, 385, 2205

[71] Narayan, R., & McClintock, J. E. 2012, MNRAS, 419, L69

[72] Nayakshin, S., Kazanas, D., & Kallman, T. R. 2001, X-ray Emission from Accretion onto Black Holes,

[73] Ng, C., Díaz Trigo, M., Cadolle Bel, M., & Migliari, S. 2010, A&A, 522, A96

[74] Novikov, I. D., & Thorne, K. S. 1973, Black Holes (Les Astres Occlus), 343

[75] Page, M. J., Soria, R., Wu, K., Mason, K. O., Cordova, F. A., & Priedhorsky, W. C. 2003, MNRAS, 345, 639

[76] Ponti, G., Fender, R. P., Begelman, M. C., et al. 2012, MNRAS, 422, L11

[77] Pringle, J. E. 1981, ARA&A, 19, 137

[78] Reis, R. C., Fabian, A. C., Ross, R. R., Miniutti, G., Miller, J. M., & Reynolds, C. 2008, MNRAS, 387, 1489

[79] Reis, R. C., Fabian, A. C., & Miller, J. M. 2010, MNRAS, 402, 836

[80] Reynolds, C. S., & Fabian, A. C. 2008, ApJ, 675, 1048

[81] Ross, R. R., & Fabian, A. C. 2005, MNRAS, 358, 211

[82] Russell, S. C., & Bessell, M. S. 1989, ApJS, 70, 865

[83] Ross, R. R., Fabian, A. C., & Young, A. J. 1999, MNRAS, 306, 461

[84] Rykoff, E. S., Miller, J. M., Steeghs, D., & Torres, M. A. P. 2007, ApJ, 666, 1129

[85] Di Salvo, T., Done, C., Życki, P. T., Burderi, L., & Robba, N. R. 2001, ApJ, 547, 1024

[86] Schnittman, J. D., Homan, J., & Miller, J. M. 2006, ApJ, 642, 420

[87] Shidatsu, M., Ueda, Y., Tazaki, F., et al. 2011, PASJ, 63, 785

[88] Shafee, R., McClintock, J. E., Narayan, R., Davis, S. W., Li, L.-X., & Remillard, R. A. 2006, ApJ, 636, L113

[89] Shafee, R., McKinney, J. C., Narayan, R., Tchekhovskoy, A., Gammie, C. F., & McClintock, J. E. 2008, ApJ, 687, L25

[90] Shahbaz, T., Fender, R., & Charles, P. A. 2001, A&A, 376, L17

[91] Shimura, T., & Takahara, F. 1995, ApJ, 445, 780

[92] Soria, R., Wu, K., Page, M. J., & Sakelliou, I. 2001, A&A, 365, L273

[93] Steiner, J. F., McClintock, J. E., Remillard, R. A., Narayan, R., & Gou, L. 2009, ApJ, 701, L83

[94] Steiner, J. F., McClintock, J. E., Remillard, R. A., Gou, L., Yamada, S., & Narayan, R. 2010, ApJL, 718, L117

[95] Straub, O., Done, C., & Middleton, M. J. 2012, arXiv:1208.0160

[96] Thorne, K. S. 1974, ApJ, 191, 507

[97] Uttley, P., Wilkinson, T., Cassatella, P., et al. 2011, MNRAS, 414, L60

[98] Walton, D. J., Reis, R. C., Cackett, E. M., Fabian, A. C., & Miller, J. M. 2012, MNRAS, 422, 2510

[99] Weisskopf, M. C., Guainazzi, M., Jahoda, K., Shaposhnikov, N., O'Dell, S. L., Zavlin, V. E., Wilson-Hodge, C., & Elsner, R. F. 2010, ApJ, 713, 912

[100] Wilms, J., Nowak, M. A., Pottschmidt, K., et al. 2001, MNRAS, 320, 327

[101] Wu, K., Soria, R., Page, M. J., et al. 2001, A&A, 365, L267

[102] Yamada, S., et al. 2009, ApJL, 707, L109

[103] Young, A. J., Lee, J. C., Fabian, A. C., Reynolds, C. S., Gibson, R. R., & Canizares, C. R. 2005, ApJ, 631, 733

[104] Zdziarski, A. A., Gierliński, M., Mikołajewska, J., Wardziński, G., Smith, D. M., Harmon, B. A., & Kitamoto, S. 2004, MNRAS, 351, 791

[105] Zhang, S. N., Cui, W., & Chen, W. 1997, ApJ, 482, L155

[106] Życki, P. T., Done, C., & Smith, D. A. 2001, MNRAS, 326, 1367